Mode Analyses of Gyrokinetic Simulations of Plasma Microturbulence

by

David R. Hatch

A dissertation submitted in partial fulfillment

of the requirements for the degree of

Doctor of Philosophy

(Physics)

at The University of Wisconsin - Madison

2010

For Jen and Owen

ACKNOWLEDGEMENTS

I would like to thank my advisor, Paul Terry, who provided me with a research topic which I have found engaging and challenging, and has also offered an ideal balance of guidance, direction, freedom to roam, and friendship. I owe thanks to the many people with whom I have collaborated on certain aspects of this thesis - Bill Nevins, who introduced me to gyrokinetics and data analysis; Frank Jenko, Florian Merz, and M. J. Pueschel who have been helpful in my GENE-related studies; and Diego Del-Castillo-Negrete, with whom I have developed applications of HOSVD. I would also like to thank those who have facilitated my development as a plasma physicist, particularly Farrell Edwards and Eric Held at Utah State University, and the many fantastic plasma faculty members at the University of Wisconsin. I am grateful to the many fellow-students and post-docs with whom I have shared ideas, expertise, and friendship - Huck for many entertaining lunch breaks, Juhyung, Kirit, Kurt, Varun, and many others. I thank my parents, brother, and sisters for years of support. Also, my son, Owen, who has provided many pleasant (but not always convenient) distractions over the past year and a half. And finally, I thank my beloved wife, Jen, who has been a great source of support and companionship, and will, unfortunately, still have to survive without a dishwasher for the foreseeable future.

TABLE OF CONTENTS

LIST OF FIGURES

Figure

ABSTRACT

Mode Analyses of Gyrokinetic Simulations of Plasma Microturbulence

by

David R. Hatch

Steady progress has been made over the last several decades in the quest to produce fusion energy through magnetic confinement. One of the remaining obstacles to realizing this goal is the small scale plasma turbulence that allows heat and particles to escape confinement by moving across the magnetic field to the plasma boundary. Thus a major effort in fusion research is in developing a better understanding of this turbulence and the capability of predicting its effects in fusion devices - the overarching motivation of this thesis.

Many models have been used to describe plasma microturbulence. These range in complexity from simple local fluid models which are amenable to analytic calculations to comprehensive gyrokinetic models which must be solved by massive parallel simulations. Recently work has used fluid models to identified a novel fundamental phenomenon in plasma microturbulence - the nonlinear excitation of damped eigenmodes and the resulting modification to saturation and transport processes. A major theme of this thesis is bridging the gap between this insight gained from fluid models and the complexity of gyrokinetic simulations.

In order to address this question of damped mode excitation in gyrokinetic models, mode decompositions are used to analyze gyrokinetic simulation data. A mode decomposition can be constructed by projecting a nonlinearly evolved gyrokinetic distribution function onto a set of linear eigenmodes, or alternatively by constructing a proper orthogonal decomposition (POD) of the distribution function. Both of these techniques are described and corresponding results are presented.

POD decompositions are used to examine the role of damped modes in saturating ion temperature gradient (ITG) driven turbulence. In order to identify the contribution of different modes to the energy sources and sinks, numerical diagnostics for a gyrokinetic energy quantity were developed for the GENE code. The use of these energy diagnostics in conjunction with POD mode decompositions demonstrates that ITG turbulence saturates largely through dissipation by damped modes at the same perpendicular spatial scales as those of the driving instabilities. This defines a picture of turbulent saturation that is very different from both traditional hydrodynamic scenarios and also many common theories for the saturation of plasma turbulence.

POD mode decompositions are also used to examine the role of subdominant modes in causing magnetic stochasticity in electromagnetic gyrokinetic simulations. It is shown that the magnetic stochasticity, which appears to be ubiquitous in electromagnetic microturbulence, is caused largely by subdominant modes with tearing parity.

The application of higher-order singular value decomposition (HOSVD) (a high-dimensional variant of the matrix decomposition, singular value decomposition (SVD)) to the full distribution function from gyrokinetic simulations is presented. This is an effort to demonstrate the ability to characterize and extract insight from a very large, complex, and high-dimensional data-set - the 5-D (plus time) gyrokinetic distribution function. It is also shown that the HOSVD is very effective at compressing gyrokinetic

data - a capability that can find many practical uses in the field of gyrokinetics.

Finally, methods for inferring the excitation of damped eigenmodes without the use of mode decompositions are discussed. Such methods are presented in the course of describing preliminary work performed before many of the useful techniques described in this thesis were developed. These have possible applications in identifying damped mode effects in experimental data.

CHAPTER I

Introduction

1.1 Turbulence and Transport in Fusion Devices

Magnetically confined fusion holds the promise of solving many of the world's energy problems. The fuel (deuterium) is virtually inexhaustible and available everywhere on earth, it produces no greenhouse emissions, and the resulting radiation levels are minimal compared with the byproducts of fission (1). Although the quest to produce a viable fusion energy source has been fraught with challenges and setbacks, striking and steady progress has been made since fusion research began in earnest in the mid-twentieth century. An illustration of this progress is shown in Fig. 1.1 where advancements in the fusion triple product (2), $n_0 T_0 \tau$ (where n_0 is the plasma density, T_0 is the temperature, and τ is the confinement time), are plotted along with analogous measures of performance in other fields. By this measure, progress in fusion research has outpaced progress in computer speed as described by the well-known Moore's law. Currently, ITER, an experimental fusion device funded by a multi-billion dollar international collaboration, is being built in the EU with the expectation of experimental startup within ten years (3). ITER is expected to demonstrate that large amounts of energy can be produced by a laboratory fusion

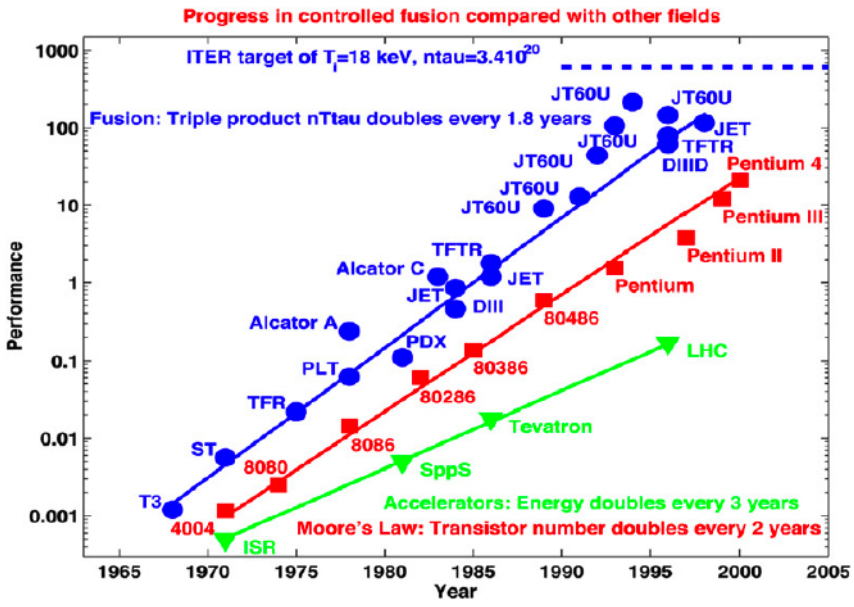

Figure 1.1: Plot of the advancement in measures of performance in three different fields - fusion triple product (blue), computer performance (red), and particle accelerator energy (green). Source: Ref. (3)

device; projections indicate the capability of producing $\sim$ 500 MW of energy (a rate of energy production sufficient to power a half-million homes) for pulses of several hundred seconds (4). Yet even in the event that ITER matches its expectations, several obstacles (e.g., the capability of continuous operation, material surfaces that can withstand high neutron fluxes for long periods of time, etc.) will need to be overcome in order for fusion to contribute on a large scale to the world's energy supply. Nonetheless, in light of the striking history of human scientific innovation, and the recent decades of steady progress in fusion research, one may be optimistic that the goal of a valid fusion energy source will eventually be realized.

The progress represented in Fig. 1.1 can be attributed to improvements in plasma confinement. In order to achieve a fusion power source, further improvements are necessary. Since the early days of fusion research, various mechanisms have been responsible for the erosion of plasma confinement in fusion devices. The earliest cul-

prits were catastrophic large-scale (machine size) disruptions that resulted in near-instantaneous escape of the plasma from the confining magnetic fields. With the development of magneto-hydrodynamic (MHD) theory (5),(6), the most violent of these disruptions were eventually largely understood and eliminated (7). It was soon discovered, however, that even in the absence of disruptive large scale MHD activity there remains a residual level of heat and particle transport that erodes confinement. The earliest attempts to explain this problem appealed to classical and neo-classical collisional transport theories, but predictions based on these models under-predict actual transport levels by orders of magnitude (8). Thus the high level of residual transport was dubbed 'anomalous,' and identification of some additional physical phenomenon was necessary. It was soon speculated, and has been increasingly validated, that small scale (on the order of the gyro-radius) plasma turbulence is responsible for most of the heat and particle transport in modern fusion devices (9), (10).

This small scale turbulence is caused by microinstabilities which are driven by gradients in the background density and temperature profiles. The earliest efforts to understand these micro-instabilities and the resulting turbulence relied on fluid models, (9) which describe the evolution of a small number of fluctuating physical quantities such as, e.g., density, temperature, electrostatic potential, and vorticity (see, e.g., Refs. (11), (12), and (13)). These studies produced a foundational understanding of many of the most critical aspects of the phenomenon; many candidate instabilities were derived, expectations were compared with experimental evidence, and the dependence of these instabilities on such things as gradient scale lengths, magnetic shear, safety factor, q, and flow shear were examined (14),(15),(9). However, these reduced fluid models are not comprehensive enough to provide quantitatively accurate predictions of experimental fluctuations. Successively greater degrees of complexity and comprehensiveness have been incorporated into studies of plasma

microturbulence, first with gyrofluid models (16),(17), and finally with simulations of the gyrokinetic model (18). Progress in computational power has facilitated many of these advances. Highly scalable computer codes can now solve the gyrokinetic equations while resolving nearly all of the physical effects (e.g., electron dynamics, realistic geometry, impurity ions, electromagnetic effects, etc.) thought to be important to the core microturbulence (19). There are examples of excellent agreement between simulated predictions and experimental results, but also (possibly more) examples of unexplained discrepancies (the following references provide example of both, usually in the same study: (19)-(25)). Thus there is much to be done before the capability is developed to reliably predict the effects of microturbulence. Such an understanding would plausibly reveal novel methods for suppressing it as well. This goal of a more complete and comprehensive understanding of plasma microturbulence in fusion devices is the over-arching motivation for the research presented in this thesis.

1.2 Damped Eigenmode Paradigm

In spite of the current trends toward comprehensive models (gyrokinetics) and massive simulations of them, there is still much that can be learned from reduced fluid models. One example of this is the body of work upon which this thesis builds - the discovery and developing understanding over the last decade of the role of damped eigenmodes in saturating microturbulence and modifying transport levels. This understanding has stemmed from extensive studies of eigenmode decompositions of local fluid models (26) - (30).

In the context of fluid models, the instabilities that drive plasma microturbulence are mathematically defined as eigenmodes of a linear system of coupled ODEs. This eigenmode problem produces the same number of solutions as the number of equa-

tions in the system. One of these solutions defines an unstable eigenmode and the others define stable eigenmodes which, linearly, exhibit exponential decay. In spite of their stability, these damped modes are driven to significant amplitude by nonlinear coupling. Thus, distinct physical processes occur at the same scales - 1) unstable eigenmodes injecting fluctuation energy and driving outward transport, and 2) stable eigenmodes dissipating energy and (in fluid systems) driving inward transport. The outward transport, of necessity, is the dominant process, but the net transport is substantially diminished due to the damped eigenmodes. This is a much different paradigm than more traditional views of turbulence dynamics which rely on dissipation through energy transfer to small scales. Such views are largely inherited from hydrodynamic Navier-Stokes turbulence where there are no damped eigenmodes and dissipation can only occur at small scales.

Studies of damped eigenmodes in fluid models have established that any damped root of the linear dispersion relation is universally excited by nonlinear mode coupling and grows exponentially from an initial state in which amplitudes are infinitesimally small (28). It was also established that damped eigenmodes can saturate the instability, absorbing energy at a rate that is comparable to the energy input rate (26), (27), that they modify transport fluxes (26), (29), and that they can modify cascade directions (30). From analysis of a diverse set of instability models, it has been established that damped eigenmode excitation is intrinsic to many physical systems and parameter regimes (27). The question of whether the damped eigenmode physics of reduced fluid models extends to comprehensive models like gyrokinetics is one of the motivations of this thesis.

The gyrokinetic model (which will be described in detail in Chap. II) describes turbulent fluctuations by evolving a perturbed gyrocenter distribution function, $g_{k_x,k_y}(z, v_{||}, \mu, t)$, where x and y are the radial and binormal directions, k_x and k_y are the associated

Fourier wavenumbers (appropriate for a local flux tube approximation as is used in this work), z is the direction parallel to the magnetic field, $v_{||}$ is the parallel velocity, μ is magnetic moment, and t is time. In this thesis the gyrokinetic GENE code (31) is the numerical tool used to produce gyrokinetic turbulence data.

A typical linear initial-value gyrokinetic simulation will solve for the perturbed gyrocenter distribution function, g, of the most unstable eigenmode for a selected wavevector (k_x, k_y). (In this description a particle species index for the distribution function has been suppressed consistent with the adiabatic electron assumption). There is typically a range of instability for small $k_\perp$ (e.g. $k_\perp \rho_i \lesssim 0.5$ for ITG driven turbulence, where ρ_i is the ion gyro-radius) outside of which all eigenmodes are stable. Within the range of instability the most unstable mode will grow to dominate the solution, which will be of the form $g_{k_x,k_y}(z, v_{||}, \mu, t) = f_{k_x,k_y}(z, v_{||}, \mu)e^{-i(\omega_{k_x,k_y}+i\gamma_{k_x,k_y})t}$. This defines a fixed eigenmode structure f, which oscillates in time according to its linear mode frequency, ω, and grows exponentially according to its growth rate, γ. If one looks at the same wavevector (k_x, k_y) in a nonlinear simulation, the fluctuations are much more complex and, at times, bear little resemblance to the structure of the unstable eigenmode. Many degrees of freedom (vastly more than the two or three in a fluid model) are available to the fluctuation spectrum. In order to characterize this complexity we introduce as an analysis tool a mode decomposition, which is the basis of many of the result presented in this thesis,

$$g_{k_x,k_y}(z, v_{||}, \mu, t) = \sum_n f^{(n)}_{k_x,k_y}(z, v_{||}, \mu)h^{(n)}_{k_x,k_y}(t). \tag{1.1}$$

The first mode in the decomposition, $f^{(1)}_{k_x,k_y}(z, v_{||}, \mu)$, corresponds to the unstable eigenmode structure and fluctuates in time according to $h^{(1)}_{k_x,k_y}(t)$ - a balance of the effects of linear drive and nonlinear stabilization. The remaining modes $f^{(n)}_{k_x,k_y}(z, v_{||}, \mu),(n >$

1) are also defined by fixed mode structures and fluctuate according to their time amplitudes, $h^{(n)}_{k_x,k_y}(t)$, $(n > 1)$. These modes fluctuate according to a balance of linear damping (dissipating energy from the fluctuations) and nonlinear drive in such a way that the nonlinear state is exactly reproduced at each moment in time. Specific examples of this type of mode decomposition will be given in Chap. III. The $n > 1$ modes exist at the same perpendicular scales (k_x, k_y) as an unstable mode $(n = 1)$, but have smaller amplitude. As such, the $n > 1$ modes will be called subdominant modes throughout this thesis. Subdominant *unstable* modes exist in some parameter regimes where multiple instabilities coincide at the same scales. For example, ITG turbulence and collisionless trapped electron mode (CTEM) turbulence can coexist and simultaneously contribute to transport dynamics as described in Ref. (32). In other common parameter regimes, including that defined by the well-known cyclone base case (CBC) parameters (18) (which will be discussed in detail in Chap. II), there is at most one unstable eigenmode per wavevector (k_x, k_y). The remaining linear eigenmodes are stable in the sense that they dissipate energy from the fluctuations (*not* in the sense that they are characterized by negligible amplitude). In either case (one or multiple linear instabilities) the vast majority of subdominant modes in a mode decomposition are damped modes (note that the terms damped and stable will be used interchangeably). This work represents the first quantitative analysis of the effects of subdominant stable modes in gyrokinetic simulations.

The damped eigenmode paradigm adds an extra dimension to some of the more standard ways of interpreting the dynamics of plasma microturbulence. For example, things such as energy transfer or nonlinear coupling are often examined only in the two dimensional space of perpendicular wavevectors (k_x, k_y). Analysis of damped eigenmodes allows one to consider energy transfer in an extra dimension of subdominant modes. Nonlinear interactions not only involve coupling between different

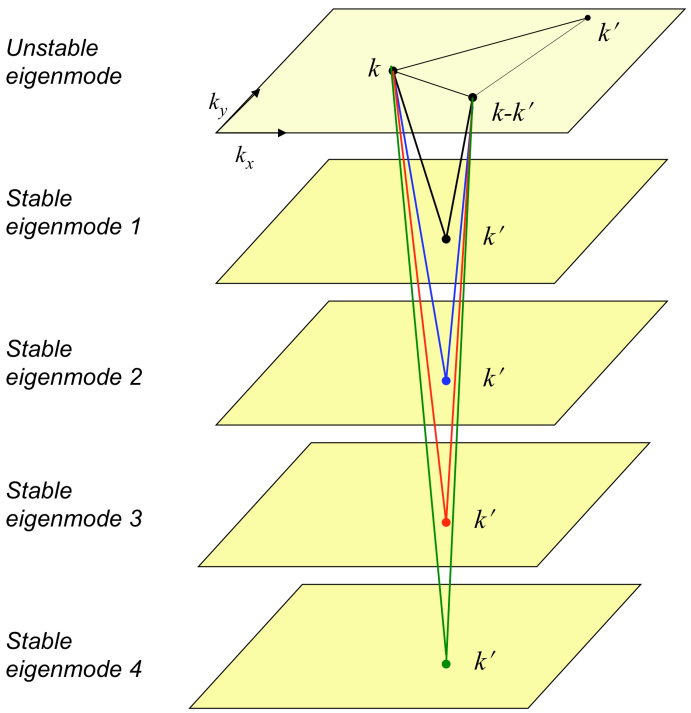

Figure 1.2: Schematic representation of damped mode paradigm. Energy transfer and nonlinear coupling occur between a series of modes at the same perpendicular scales.

wavevectors, but also coupling between a variety of *modes* ($f^{(n)}_{k_x,k_y}(z, v_{||}, \mu)$) at different wavevectors. This is illustrated schematically in Fig. 1.2, where the upper plane represents the most unstable eigenmode at different wavevectors and the lower planes represent subdominant stable modes defined on the same space of wavevectors. The results presented in this thesis show that this extra dimension of energy transfer is crucial for understanding many aspects of plasma microturbulence.

1.3 Outline of Thesis

This thesis will proceed as follows. Chapter II will provide a brief introduction to gyrokinetics. A description of the assumptions and ordering scheme used to derive the model will be provided. The conserved energy quantity for the gyrokinetic

equation will then be described and discussed. Then numerical energy diagnostics that have been developed in the GENE code (31) will be described. In Chap. III the relation between the mode decompositions used in this work and the linear eigenmode decomposition used in previous work with fluid models will be discussed. Following that, two types of mode decompositions will be described - linear eigenmode decompositions, and proper orthogonal decomposition (POD). Some results from each of these decompositions will be presented in this chapter. In Chap. IV, POD will be used to determine the role of damped modes in the saturation of ion temperature gradient (ITG) driven turbulence. It is shown that the excitation of damped modes causes dissipation to peak at the same scales as the driving instabilities. A novel form of equipartition of a dissipation-like quantity among damped modes will also be described in this chapter. In Chap. V the role of subdominant modes in electromagnetic turbulence will be described. Recent gyrokinetic studies have demonstrated the development of magnetic stochasticity due to microscale magnetic fluctuations. For most parameter regimes, the magnetic fluctuations associated with the most unstable modes are non-resonant - i.e., they are incapable of breaking magnetic flux surfaces and causing reconnection. In this chapter, it is shown that subdominant modes with tearing parity are the main cause of the observed magnetic stochasticity. In Chap. VI higher order singular value decomposition (HOSVD) will be described. This chapter departs from the previous chapters in the sense that there is limited direct relevance to damped mode phenomena, but continues the theme of analyzing the complexity of kinetically described turbulence. HOSVD is a tensor decomposition that is particularly well suited to analyzing and compressing high-dimensional data-sets. As such, it is a useful tool for extracting information from the six-dimensional (5-D plus time) gyrokinetic distribution function from a nonlinear simulation. A description will be provided of the underlying mathematics of the HOSVD, numerical implementation of

an HOSVD algorithm, and physical insight gained from its application to gyrokinetic data. In Chap. VII a preliminary examination of damped mode effects in gyrokinetic turbulence is recounted. Many of the results have been superseded by those reported in Chaps. II-V, but much of the discussion is instructive with regard to, e.g., possible ways to identify damped mode effects in experiments. Chapter VIII will summarize the major results of this thesis, offer conclusions, and discuss possible directions for future work.

CHAPTER II

The Gyrokinetic Equation and Gyrokinetic Energetics

2.1 The Gyrokinetic Equation

Plasma microturbulence in fusion devices has the favorable (for theorists) property of being characterized by length and time scales that are distinctly separate from other scales in the system. This facilitates a robust ordering scheme that allows for the perturbative treatment that is the basis for the gyrokinetic model. The scale lengths perpendicular to the background magnetic field are on the order of the ion gyroradius (for ion fluctuations) and much smaller than macroscopic scale lengths

$$k_\perp \rho_i \sim \mathcal{O}(1), \text{ and } \frac{\rho_i}{L} \equiv \rho_* \ll 1, \tag{2.1}$$

where L represents a macroscopic scale length such as the major radius, ρ_i is the ion gyro-radius, and the ratio of the two, ρ_* (pronounced rho-star), is used as the small quantity for a perturbation analysis. In practice ρ_* is, indeed, a legitimately small number ($\mathcal{O}(10^{-3})$ for current Tokamaks, and this will decrease as Tokamaks trend toward larger size and stronger magnetic fields). In contrast with the perpendicular

scales, the fluctuations are extended in the direction along the magnetic field line,

$$\frac{k_{||}}{k_{\perp}} \sim \mathcal{O}(\rho_*). \tag{2.2}$$

The time scales of interest are small compared to the gyro-frequency

$$\frac{\omega}{\Omega_i} \sim \mathcal{O}(\rho_*), \tag{2.3}$$

where ω is some dynamic times scale such as the unstable mode growth rate or frequency, and Ω_i is the ion gyro-frequency. In addition, the fluctuating quantities are small compared to the background quantities,

$$\frac{e\delta\phi}{T_0} \sim \frac{\delta B}{B_0} \sim \mathcal{O}(\rho_*). \tag{2.4}$$

Velocity space coordinates are defined in such a way that they are related to the background magnetic field. One coordinate, $v_{||}$, represents particle velocity in the direction parallel to the magnetic field, and the magnetic moment, $\mu = \frac{mv_{\perp}^2}{2B_0}$, defines the magnitude of the velocity perpendicular to the magnetic field (note that this representation for velocity space is not universal among gyrokinetic codes). One additional velocity coordinate is necessary to define the three dimensional velocity vector. This is the gyro-angle, λ, which denotes the orientation of the perpendicular component of the velocity.

In the spatial dimensions, guiding-center coordinates are used to define the position of the centers of the particle gyro-orbits

$$\vec{X} = \vec{x} - \rho_j(cos(\lambda)\hat{x} + sin(\lambda)\hat{y}), \tag{2.5}$$

where $\vec{X}$ is the position of the guiding-center, $\vec{x}$ is the particle position, and the remaining term is the gyroradius. These coordinates facilitate a separation of the fast gyro-motion from the more important drift motion.

The gyrokinetic equation is derived from the Vlasov equation (33),

$$\left(\frac{\partial}{\partial t} + \mathbf{v}\cdot\frac{\partial}{\partial \mathbf{x}} + q_j[\mathbf{E}(\mathbf{x},t) + \mathbf{v}\times\mathbf{B}(\mathbf{x},t)]\cdot\frac{\partial}{\partial \mathbf{v}}\right) f_j(\mathbf{x},\mathbf{v},t) = 0, \tag{2.6}$$

where f_j is the distribution function for particle species j. This equation is an expression of the conservation of the phase space volume of the particle distribution function.

The gyrokinetic equation is derived by first transforming the Vlasov equation into guiding-center coordinates. The gyro-motion is much faster than the time scales of interest (see Eq. 2.3) and can be formally eliminated by averaging over the gyro-angle, λ. This eliminates the fast time scale, reduces the problem from six dimensions to five (three spatial and two velocity), and puts the 'gyro' in gyrokinetics. In addition, the distribution function can be split into a background Maxwellian and a perturbed distribution function, δf_j, that represents the fluctuations: $f_{full_j} = F_{M_j} + \delta f_j$. This splitting of the distribution function, in conjunction with the ordering scheme defined Eqs. 2.1-2.4, facilitates a perturbative treatment wherein terms of different order in ρ_* are equated and, when possible, solved (for derivations of the gyrokinetic equation see Refs. (34)-(36)). The result is the coupled gyrokinetic-Maxwell system. The gyrokinetic equation defines the evolution of the perturbed distribution function

$$\frac{\partial g_j}{\partial t} = \mathcal{L}[g_j] + \mathcal{N}[g_j], \tag{2.7}$$

where g_j is related to the full perturbed distribution f_j function through

$$f_j = g_j - \frac{2q_j}{m_j v_{Tj}} v_{||} \bar{A}_{||} F_{0j}. \tag{2.8}$$

Note that the distribution functions in Eq. 2.8 are perturbed distribution functions but the δ prefix is dropped - a convention followed throughout this thesis. In Eq. 2.7, $\mathcal{L}$ represents the linear gyrokinetic operator, and $\mathcal{N}$ represents the nonlinearity. The gyrokinetic Poission equation

$$\phi = \frac{\sum_j n_{0j} \pi q_j B_0 \int J_0(\lambda_j) g_j dv_{||} d\mu}{k_\perp^2 \lambda_D^2 + \sum_j \frac{q_j^2}{T_{0j}} n_{0j} (1 - \Gamma_0(b_j))}, \tag{2.9}$$

and Ampere's law,

$$A_{||} = \frac{\sum_j \frac{\beta}{2} q_j n_{j0} v_{Tj} \pi B_0 \int v_{||} J_0(\lambda_j) g_j dv_{||} d\mu}{k_\perp^2 + \sum_j \frac{\beta q_j^2}{m_j} n_{0j} \pi B_0 \int v_{||}^2 J_0^2(\lambda_j) F_{0j} dv_{||} d\mu}. \tag{2.10}$$

define the self-consistent electromagnetic fields that are part of the linear and nonlinear operators. Expressions for these operators, along with definitions and descriptions of all other terms in Eqs. 2.7-2.10 are given in Appendix A.

A field following coordinate system is used to exploit the spatial scales of the fluctuations; one can maintain an extended domain along the field line and a much smaller domain in the perpendicular dimensions. Such a coordinate system is defined by Clebsch coordinates, α and ψ, such that

$$\mathbf{B_0} = \nabla\alpha \times \nabla\psi. \tag{2.11}$$

The radial coordinate, ψ is labelled by the poloidal magnetic flux and will be called the x coordinate. The binormal coordinate, α (which will be called the y coordinate),

is related to the the toroidal ϕ and poloidal θ angles through $\alpha = \phi - q(\psi)\theta$, where q is the safety factor. The third spatial coordinate follows the background magnetic field. This coordinate - the distance along the field line - is labelled by the physical poloidal angle and will be called z.

A Fourier representation is used in the binormal y direction. In addition, even though the radial x direction is inhomogeneous (e.g., the background profiles and thus gradients vary with x), a Fourier representation is also made possible in this coordinate by application of the local flux-tube approximation (37),(38). This approximation assumes that the turbulence can be resolved in a domain that is small enough that all variations in background quantities can be approximated as linear functions of x, and that this variation is weak enough such that the turbulence is statistically identical at each end of the radial box. Additionally, due to magnetic shearing of the simulation domain, a complex boundary condition is necessary in the parallel direction wherein different k_x modes are linearly coupled: $f_{k_x,k_y}(z = \pi) = cf_{k_x+2\pi\hat{s}k_y,k_y}(z = -\pi)$, where c is a constant phase factor. This boundary condition is described in Appendix B.

2.2 Ion Temperature Gradient Instability and the Cyclone Base Case Parameters

The gyrokinetic model is capable of describing a wide variety of instabilities and the turbulence they produce. Examples of such instabilities are the ion temperature gradient (ITG) instability(18), electron temperature gradient (ETG) instability (39),(40), collisionless trapped electron mode (CTEM) (41)-(43), kinetic ballooning mode (44), and micro-tearing mode (45). Recent studies have even examined the interplay between multiple of these instabilities (46),(32). This work is restricted

largely to an examination of ITG driven turbulence. ITG turbulence is the most studied, and, in many experiments, the most important of these instabilities.

A simple diagram illustrating the ITG instability is shown in Fig. 2.1 (taken from Ref. (17)). The perturbation of the equilibrium pressure profile shown in Fig. 2.1 creates alternating (in the poloidal direction) regions of hot and cold plasma. The temperature and charge (q_j) dependences in the gradient and curvature drifts,

$$\vec{v_{d_j}} = \frac{m_j \left(\frac{1}{2}v_\perp^2 + v_{||}^2\right)}{q_j B} \frac{\vec{B} \times \vec{\nabla} B}{B^2}, \tag{2.12}$$

cause a charge buildup on the interface between the hot and cold regions - upward drifting electrons in the hot region catch the more slowly upward drifting electrons in the cold region (and vice versa for the ions). This causes an alternating perturbed electric field - oriented upward in the hot regions and downward in the cold regions. This activates alternating $E \times B$ drifts,

$$\vec{v_E} = \frac{\vec{E} \times \vec{B}}{B^2}. \tag{2.13}$$

Since the $E \times B$ drift produces a bulk flow (no charge dependence), the plasma moves in a way that reinforces the original perturbation - radially outward in the hot regions and inward in the cold regions. Note that this instability occurs on the outboard side of the torus where the magnetic field gradient is oriented to produce these results. On the inboard side of the torus, the magnetic field gradient is in the same direction, but the temperature gradient reverses, thus eliminating the instability. See Refs. (17) and (48) for similar discussions of the ITG instability.

ITG turbulence was the focus of an important early benchmarking project, the Cyclone project (18), which compared simulations from several gyrokinetic and gyrofluid

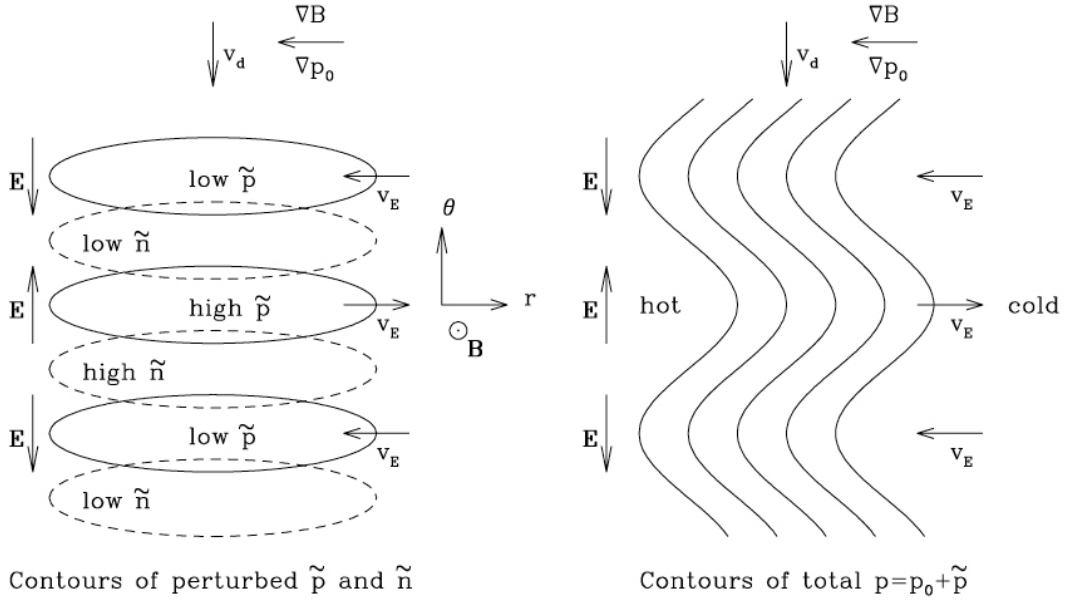

Figure 2.1: Diagram illustrating the underlying processes of the ITG instability. Source: Ref. (17)

q	$\hat{s}$	$\epsilon = r/R$	$n_i/n_e = T_i/T_e$	R/L_T	R/L_n	β	ν
1.4	0.8	0.18	1.0	6.9	2.2	0.0	0.0

Table 2.1: Cyclone base case parameters. The parameters are safety factor q, magnetic shear $\hat{s}$, inverse aspect ratio r/R, ion (electron) density $n_{i(e)}$, ion (electron) temperature $T_{i(e)}$, inverse temperature gradient scale length R/L_T, inverse density gradient scale length R/L_n, plasma β, and collision frequency ν. Variations are used for different simulations in this paper. Finite collisionality ν is used in Chap. IV and finite β is used in Chap. V.

codes. This project defined a set of experimentally relevant parameters - the Cyclone base case (CBC) - which have served as a reference point for many future gyrokinetic studies. The CBC parameters (with occasional variations therefrom) are used for the analysis in this thesis. The aim has been to demonstrate the excitation and importance of damped modes, a previously unidentified phenomenon in gyrokinetics, in the most-examined and best-understood parameter regime. The CBC parameters are shown in Table 2.1.

2.3 Gyrokinetic Energy Quantity

In order to study saturation one must first define a conserved energy-like quantity. The quantity of interest in gyrokinetics is (49),(50)

$$E = \int dv_{||} d\mu B_0 \pi \frac{n_0 T_0}{F_0} |g|^2 + D(k_\perp)|\phi|^2, \tag{2.14}$$

where B_0 is the background magnetic field, ϕ is the electrostatic potential, n_0 and T_0 are the background density and temperature, and D is a function of z and the perpendicular wavenumbers. This energy quantity has several useful properties; it provides a measure for the intensity of the turbulence, it is nonlinearly conserved, and its

sources and sinks (heat flux and collisional and numerical dissipation) are associated with intuitive physical (and numerical) quantities. Although this quantity is derived from an entropy $f \log f$ (50), here it will be called energy in order to emphasize its similarity with $|u|^2$ energy in the Navier-Stokes equation, and other quadratic energy quantities in plasma fluid models which play a similar role in turbulence. For simplicity, the discussions in this chapter are restricted to a single particle species and the electrostatic regime. Generalization to multiple kinetic species and electromagnetic effects is straightforward, and a derivation of the energy evolution equation, Eq. 2.14, which includes these details, is provided in Appendix C.

The gyrokinetic energy quantity includes two terms - one entropy-like term, (proportional to $|g|^2/F_0$), and a wave-energy term (proportional to $|\phi|^2$). The wave energy is a quantity that can be understood intuitively - it provides a measure of the intensity of the electrostatic potential which is closely related to things like $E \times B$ flow velocity, and transport fluxes. On the other hand, the entropy term can be quite unrelated to the quantities, like electromagnetic fields and low order moments, that are usually of interest. For example, if one expands the Maxwellian, F_0, in a Taylor series, it is seen that the entropy term contains moments of the distribution function at all orders. Thus it captures features like fine scale structure in velocity space.

For the purpose of the following discussion, an energy operator is defined

$$W[F,G] \equiv \sum_{k_x,k_y} \int dv_{||} d\mu dz J(z) \frac{\pi B_0 n_0 T_0}{F_0} \Gamma[F]^* G, \tag{2.15}$$

where F and G represent functions of the form of the perturbed distribution function, g_j, $J(z)$ is a Jacobian, and $\Gamma = g + \frac{qF_0}{T_0}(\bar{\phi} - v_T v_{||} \bar{A}_{||})$. The operation $W[g,g]$ reproduces the energy quantity in Eq. 2.14. An energy evolution equation is derived by operating on the gyrokinetic equation: $W[g, \mathcal{L}[g_j] + \mathcal{N}[g_j]]$. All but two of the resulting terms

vanish due to things like periodicity and other boundary conditions. The energy equation is,

$$\left.\frac{\partial E_k}{\partial t}\right|_{N.C.} = Q_k + C_k \tag{2.16}$$

where $Q = \int dv_{||} d\mu \pi n_0 T_0 B_0 (v_{||}^2 + \mu B_0) \omega_T g i k_y \bar{\phi}$ (the over-bar denotes a gyro-average) is a term proportional to the heat flux and represents the turbulent drive, C represents collisional dissipation (and in a simulation, whatever artificial dissipation is used). The subscript N.C. denotes that this equation describes only non-conservative processes, i.e., processes that inject or dissipate net energy from the system.

At first glance it may be surprising that all sources and sinks of the gyrokinetic system are subsumed in a heat flux Q_k, and collisional dissipation, C_k. A brief example may be helpful in offering some insight into the energetics. Landau damping (51) is a very important and well known mechanism for collisionless damping of plasma waves, and yet is not represented in any of the terms in the energy equation. This is due to the fact that the gyrokinetic energy quantity includes both wave energy *and* entropy. Landau damping merely transfers energy between these two - it reduces wave energy while producing fine scale structure in velocity space in the distribution function. The fine scale structure represents an increase in the entropy and the total energy is conserved. The fine scale structure, in turn, increases the collisional dissipation which dissipates energy from the system.

2.4 Energy Diagnostics

2.4.1 Solution of $v_{||}$ Boundary Problem

In order to identify the effects of damped modes on the saturation of turbulence, numerical energy diagnostics were developed for the GENE code. In the course of implementing these diagnostics, it was discovered that the GENE code produced solutions with spurious contributions to the energy balance. These issues and their solution will be discussed in this subsection.

In order to test the numerical validity of Eq. 2.16, the following quantity was calculated in the code: $W[g, \mathcal{L}[g] + \mathcal{N}[g]]$. This was examined term by term to ensure that the appropriate terms cancel and the sources and sinks are restricted to the quantities in Eq. 2.16. The initial results are shown in Fig. 2.2 where it is seen that that most of the terms behave as expected with the exception of the two parallel derivative terms (shown in Eq. 2.17) which should cancel exactly but fail to do so numerically.

$$W[g, v_{Tj} v_{||} \frac{\partial \Gamma_j}{\partial z}] = -W[g, \frac{v_{Tj}\mu}{2} \frac{\partial B_0}{\partial z} \frac{\partial f_j}{\partial v_{||}}] \text{ (analytically)} \tag{2.17}$$

Application of integration by parts in the z and $v_{||}$ directions to the LHS and RHS of Eq. 2.17, respectively, produces exactly the same result:

$$\sum_{k_x, k_y} \int dv_{||} d\mu dz J(z) \frac{n_0 \pi v_T v_{||} \mu \partial_z B_0}{F_0} |g|^2 \tag{2.18}$$

In order for this integration by parts to be reproduced numerically, terms such as $|g|^2/F_0$ must cancel at the boundaries. This is violated most blatantly at the $v_{||}$ boundaries. Note that a well behaved distribution function should decrease to small amplitude at the $v_{||}$ boundary. This is, in fact, the case as shown in Fig. 2.3. However,

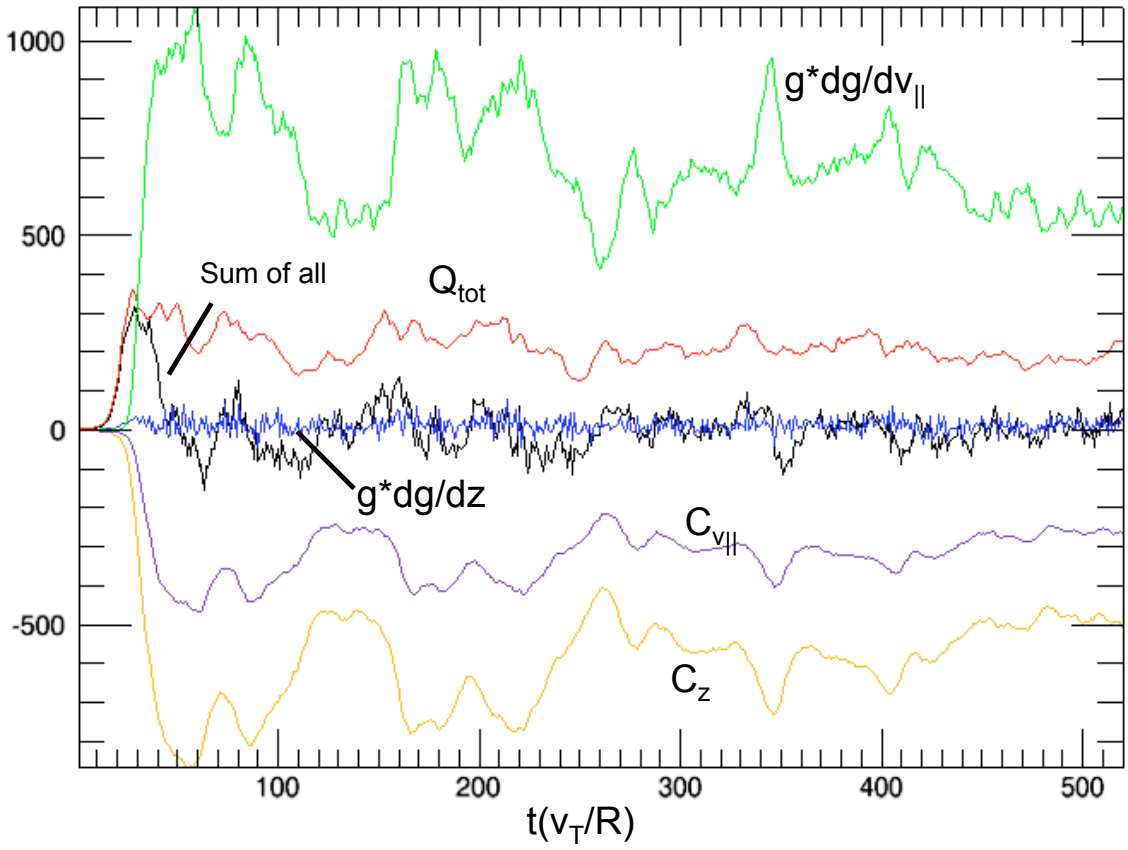

Figure 2.2: Plot of the non-vanishing terms in the energy equation. The terms denoted $g^* dg/dz$ and $g^* dg/dv_{||}$ cancel analytically but fail to do so numerically creating a spurious energy drive in the simulation.

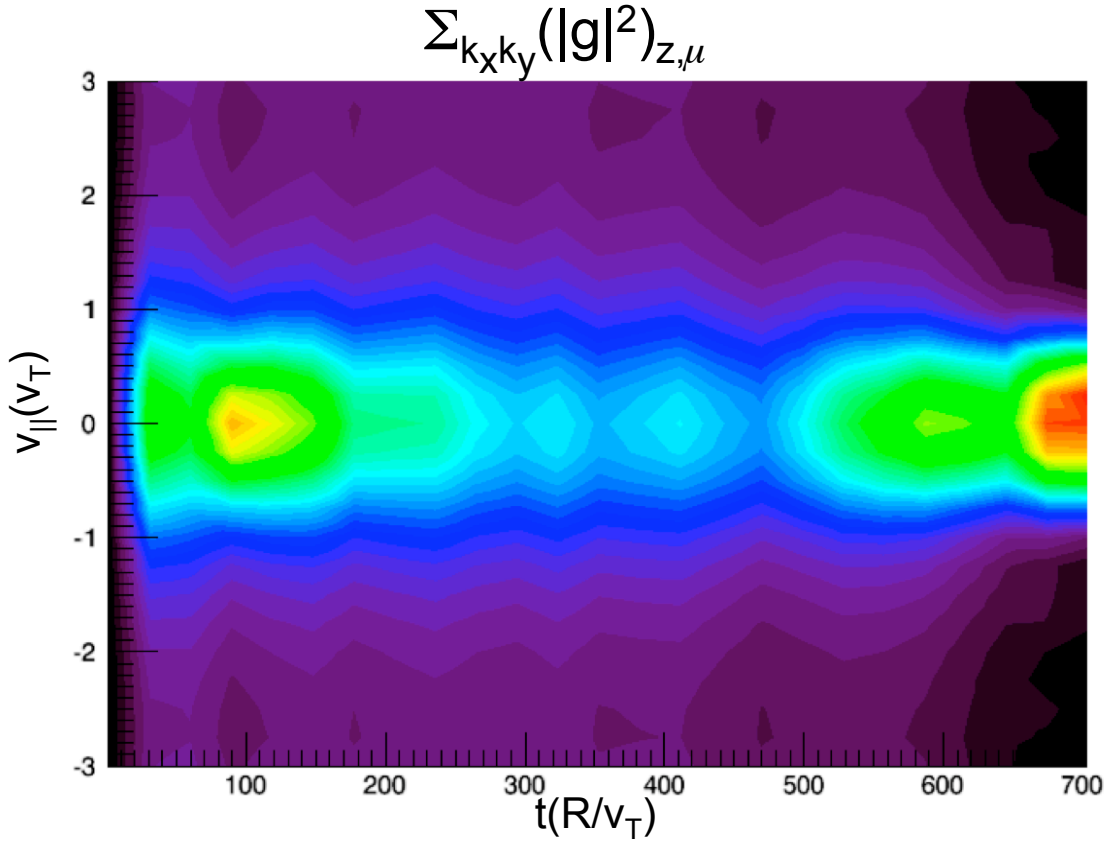

Figure 2.3: Plot of the squared amplitude of the distribution function, $|g|^2$, as a function of $v_{||}$ and time and summed or integrated over all other coordinates. The solution appears to be well behaved, decreasing to small amplitude at the $v_{||}$ boundary.

these small values for g at the high parallel velocities are divided by F_0 - another even smaller number. Thus a very small number is divided by an extremely small number and a high degree of numerical precision is necessary in order for this quantity to be meaningful. In Fig. 2.4 the quantity $|g|^2/F_0$ is plotted, showing that $|g|^2$ does not fall off fast enough to overcome the F_0 normalization. Note that this deficiency is quite unrelated to typical quantities of interest (like low order moments and transport quantities), and only becomes apparent when examining the energetics.

The most obvious solutions (increased resolution and / or artificial dissipation)

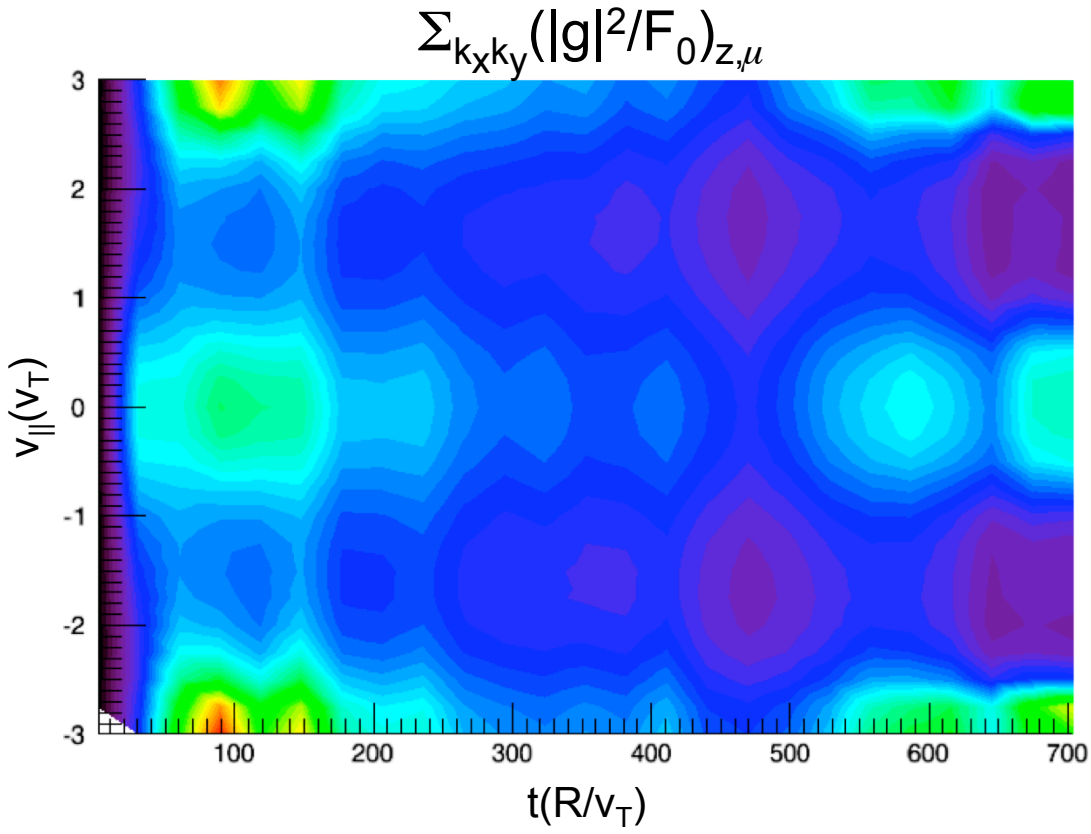

Figure 2.4: Plot of the squared amplitude of the distribution function normalized by a Maxwellian, $\frac{|g|^2}{F_0}$, as a function of $v_{||}$ and time and summed or integrated over all other coordinates. This quantity exhibits an unphysical large amplitude at the $v_{||}$ boundary.

were unsuccessful at solving this problem. A modification of the phase space grid was required to produce well behaved solutions for $|g|^2/F_0$. This modification eliminates points in velocity space that belong to those first order particle orbits which at some point leave the (square) computational grid. The constant energy particle orbits follow trajectories in $(z, v_{||}, \mu)$ that obey $E_0 = v_{||}^2 + \mu B_0(z)$. For a given value of μ (which is conserved along particle orbits), a particle obtains its maximum parallel velocity at the outboard midplane, $z = 0$, where the magnetic field is at a minimum. Consider a particle orbit, associated with a value of μ_0, whose velocity at $z = 0$ is the maximum velocity, $v_{||,max}$ resolved by the simulation. This particle's energy is $E_{max} = v_{||,max}^2 + \mu_0 B_0(z = 0)$. For this value of μ_0, any particle orbit with a higher energy than E_{max} will cross the $v_{||}$ boundary at some point on its orbit. The modified velocity grid eliminates all grid points associated with these orbits from the simulation. This modification, in conjunction with judicious selection of resolution and artificial damping parameters, produced well behaved energy quantities. The resulting $v_{||}$ dependence of $|g|^2/F_0$ is shown in Fig. 2.5, and the resulting energy terms are shown in Fig. 2.6 where it is seen that the parallel derivative terms largely cancel. This solution allowed for the discovery of many of the results presented in Chap. IV, but has been superseded by the implementation of an Arakawa differencing scheme (52) by members of the GENE development team. This modification eliminates the problems discusses here.

It is of note that some gyrokinetic codes use the particle energy, $v_{||}^2 + \mu B_0$, as a velocity coordinate in place of the parallel velocity (54),(53). As such, all particle orbits lie exactly on grid-points and none leave the computational box. In addition, this representation eliminates the $v_{||}$ derivative term from the gyrokinetic equation. Hence, the issues described in this subsection would not be problematic in such treatments. It should be noted that this representation limits the code in other ways like,

for instance, its ability to treat complex geometries (like that of a stellarator (55)) which differ significantly from a typical tokamak equilibrium.

2.4.2 Comments on Nonlinear Energy Conservation

This chapter will conclude with some comments regarding numerical nonlinear energy conservation. One of the most important properties of a turbulent energy quantity is nonlinear conservation - i.e., the nonlinearity only serves to transfer energy to and from different scales but does not dissipate or inject energy into the system. As shown in Appendix C, this is satisfied analytically for the quantity in Eq 2.14. However, the energy conservation is violated, to a degree, numerically. In a simulation, the change in energy from time t_n to t_{n+1} is $\delta E_n = E_{n+1} - E_n$. In terms of the the distribution functions at these time steps, this can be written

$$\delta E_n = W[g_{n+1}, g_{n+1}] - W[g_n, g_n] = W[g_n + \delta g_{n(L)} + \delta g_{n(N)}, g_n + \delta g_{n(L)} + \delta g_{n(N)}] - W[g_n, g_n]. \tag{2.19}$$

where δg denotes the change in the distribution function from one time step to the next, and the subscripts L and N denote the contribution from the linear operator and the nonlinear operator, respectively. The RHS of Eq. 2.19 includes a term that is quadratic in the nonlinearity, $W[\delta g_{n(N)}, \delta g_{n(N)}]$. Since the term is quadratic, it doesn't vanish (in contrast with a term like $W[g_n, \delta g_{n(N)}]$ which does vanish as described in Appendix C). Thus the nonlinearity can produce a finite contribution to the change in net energy at each time step - a violation of nonlinear energy conservation. When the time step is well chosen, δg will presumably be small and a δg^2 term will be smaller still. It is observed that in large part this is the case, as shown in Fig. 2.7 where the

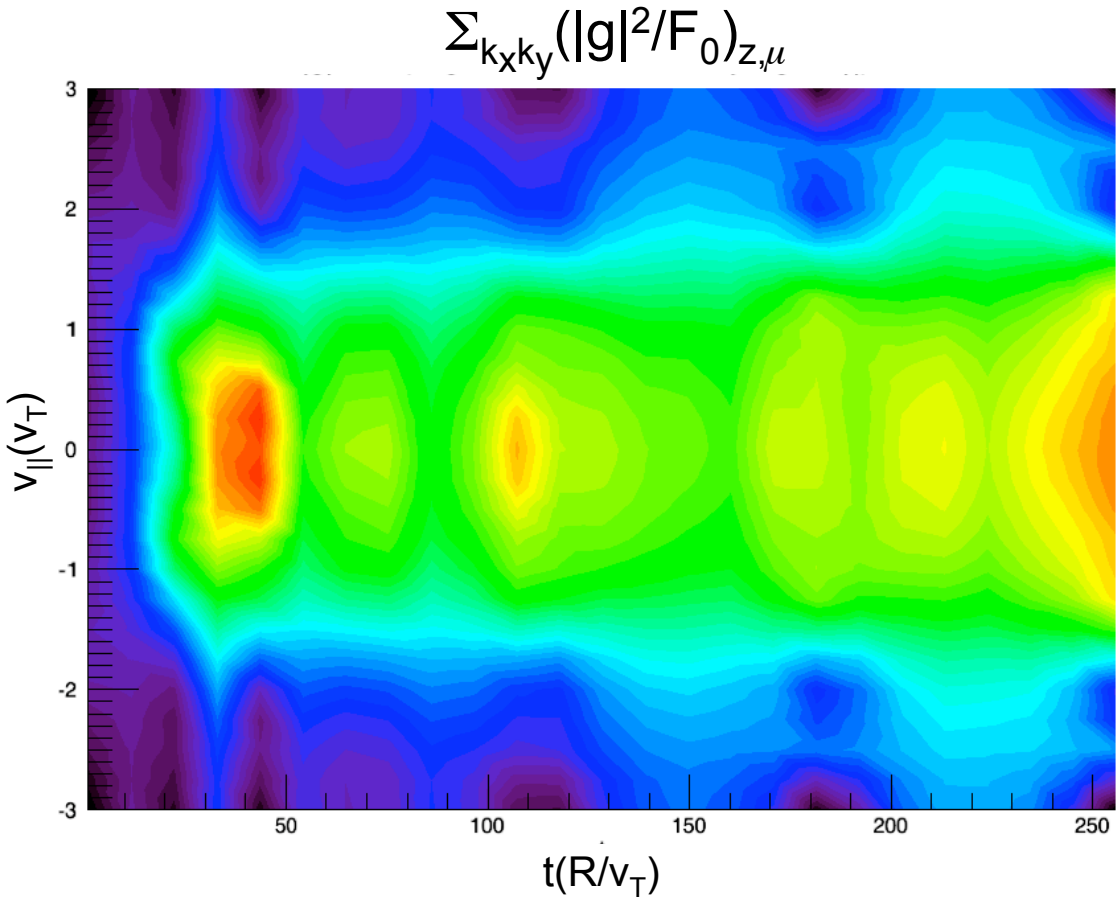

Figure 2.5: Plot of the squared amplitude of the distribution function normalized by a Maxwellian, $\frac{|g|^2}{F_0}$, as a function of $v_{||}$ and time and summed or integrated over all other coordinates. This quantity now decreases to small amplitude at the boundary due to the with the modification of the phase space grid described in Sec. 2.4.1.

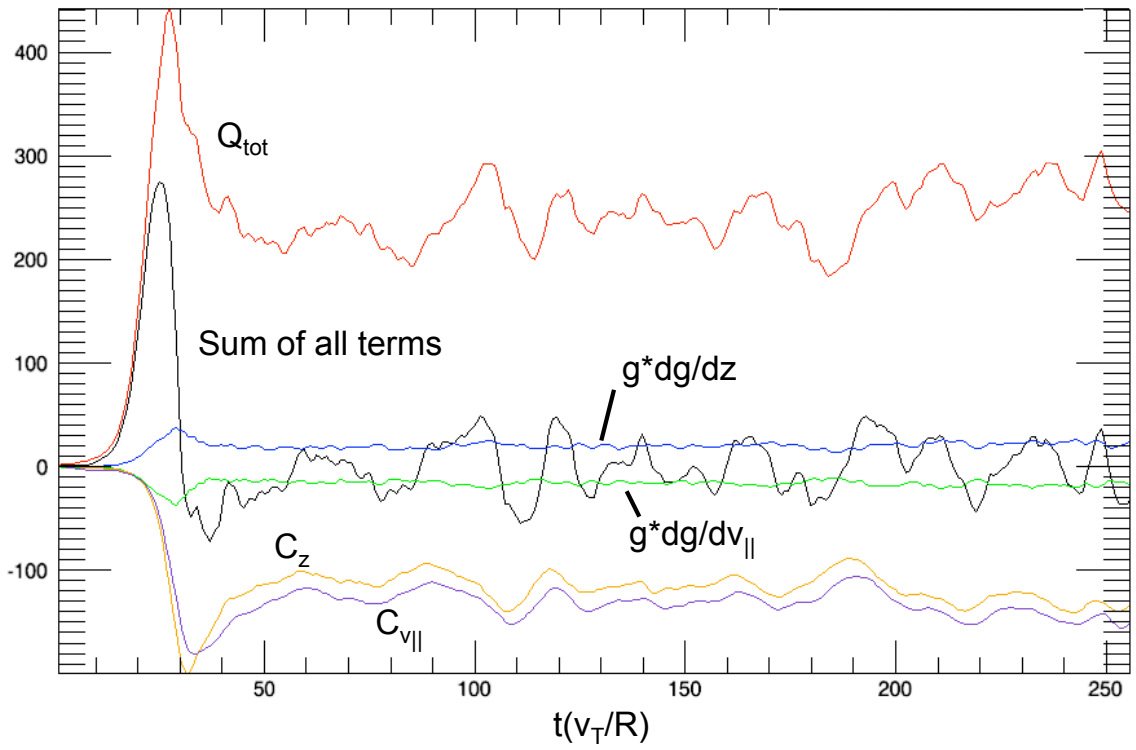

Figure 2.6: Plot of the non-vanishing energy terms. The parallel derivative terms (blue and green) now largely cancel after the modification of the phase space grid described in Sec. 2.4.1. The non-vanishing terms are now limited to those defined in Eq. 2.16.

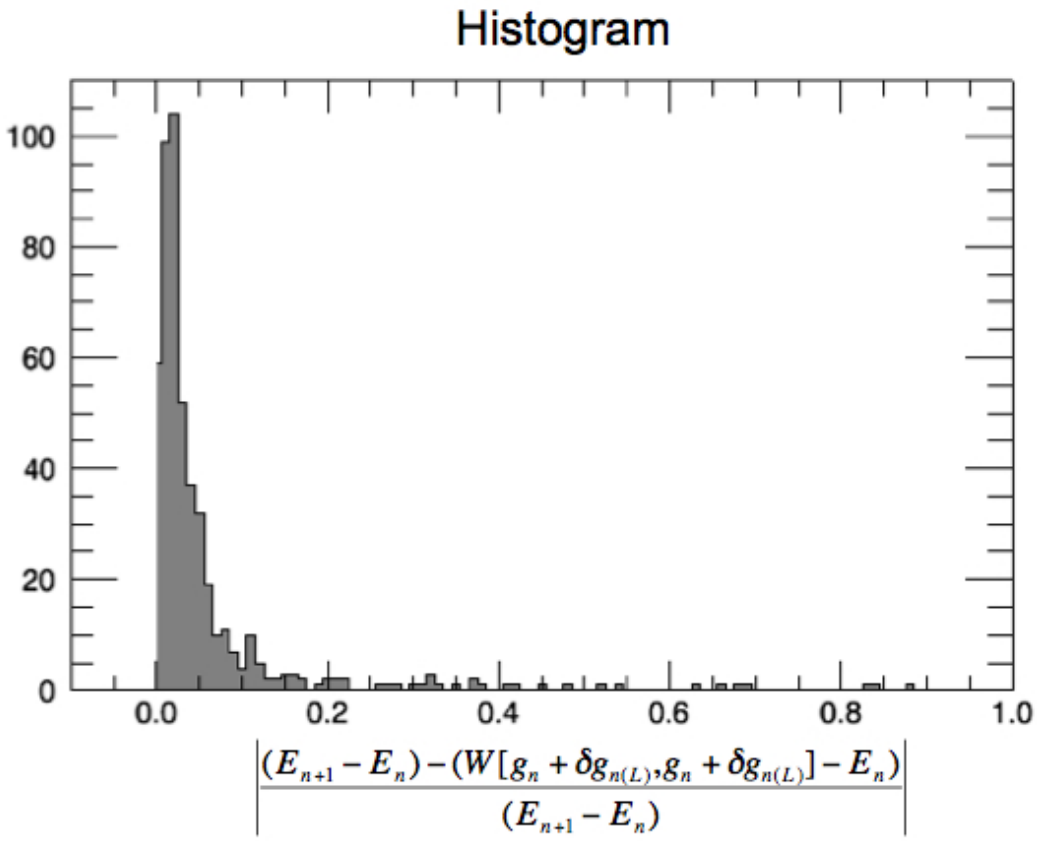

Figure 2.7: Plot of a histogram of the normalized difference between the total change in energy over one time step and the change in energy due only to linear contributions over the time step. The difference indicates a numerical violation of nonlinear energy conservation but is typically less that 5%.

difference between the full change in energy and the change in energy accounting for only the linear contributions is compared in the form of a histogram. The error in nonlinear energy conservation is typically less than 5 %. For most purposes this is satisfactory, but one should be aware of this issue if a very high degree of nonlinear energy conservation is necessary for a certain application.

CHAPTER III

Mode Decompositions of the Gyrokinetic Distribution Function

3.1 Introduction

The concept of a mode decomposition was introduced briefly in the introduction. The form of a mode decomposition is reproduced here for easy reference:

$$g_{k_x,k_y}(z, v_{||}, \mu, t) = \sum_n f^{(n)}_{k_x,k_y}(z, v_{||}, \mu) h^{(n)}_{k_x,k_y}(t). \tag{3.1}$$

A mode decomposition can be constructed by post-processing data from a nonlinear gyrokinetic simulation. One can output the distribution function for selected wavevectors (k_x, k_y) of interest. This distribution function is then projected onto a set of modes. This facilitates an analysis of the contribution of different modes to the dynamics.

Previous work has studied the effect of subdominant damped eigenmode excitation in two and three field fluid models of plasma microturbulence (26)-(30). These fluid models are systems of coupled ODE's. For example, a two field model for trapped electron mode turbulence (TEM) (26) evolves two equations - one each for the vortic-

ity and the fluctuating electron density. The linear system can be solved analytically for the two linear eigenmodes each of which is defined by linear combinations of the two fields. One of the eigenmodes is unstable for a range of wavenumbers and the other eigenmode is stable for all wavenumbers. Fluctuation data can be projected onto this basis of eigenmodes and the contribution of each eigenmode to physical processes such as transport can be calculated. In general the linear eigenmodes are not orthogonal, but the limited number of modes makes this issue manageable when interpreting results.

In contrast to fluid models, the gyrokinetic model is defined by a system of integro-partial differential equations. However, upon numerical discretization, the gyrokinetic model is also reduced to a system of ODE's albeit an extremely large system. For each wavevector (k_x, k_y), the linear gyrokinetic operator is defined by a matrix, and each point in phase space $(z, v_{||}, \mu)$ is the mathematical analogue of a field in a fluid model. The linear eigenvalues and eigenvectors are simply the eigenvalues and eigenvectors of this matrix; the eigenvector/eigenvalue pair with the largest growth rate (imaginary part of the eigenvalue) is identical to the solution to the corresponding linear initial value problem. This most unstable mode is one of $N = N_z \times N_{v_{||}} \times N_\mu$ total eigenvectors, almost all of which are stable. If these eigenmodes are linearly independent then they form a complete basis for the distribution function which is, numerically, a vector with $N = N_z \times N_{v_{||}} \times N_\mu$ elements.

3.2 Linear Eigenmode Decomposition

In light of the extensive work using linear eigenmode decompositions in fluid models, it is a reasonable first step to perform the analogous decomposition for gyrokinetic data. The GENE code is well suited for this application as it is equipped with powerful

scalable eigenmode solvers that can resolve the entire spectrum of linear eigenmodes for moderate resolution (56). The linear gyrokinetic operator is non-Hermitian (56) and so, as in the fluid models, the resulting eigenvectors are non-orthogonal. However, a mode decomposition can be constructed by using the *left* eigenvectors of the linear operator as projection operators to extract the time amplitudes of the *right* eigenvectors (See Appendix D for a definition of left eigenvectors and a demonstration of their orthogonality with regard to right eigenvectors). It can be shown that the left eigenvectors are orthogonal with regard to the right eigenvectors, i.e., $f_i^{(l)} \cdot f_j^{(r)} = \delta_{i,j}$ where $f_i^{(l)}$ is the left eigenvector associated with the ith eigenvalue and $f_j^{(r)}$ is the right eigenvector associated with the jth eigenvalue. A mode decomposition of the form of Eq. 3.1 can be constructed for a selected wavevector by operating with the left eigenvectors on the distribution function from a nonlinear simulation; using the notation in Eq. 3.1, the time amplitude of the n^{th} right eigenvector is determined by $h^{(n)}(t) = \langle f^{(n),left}(z, v_{||}, \mu), g_{k_x,k_y}(z, v_{||}, \mu, t)\rangle$, where $\langle , \rangle$ denotes a numerical sum over $(z, v_{||}, \mu)$. However, in contrast with fluid systems, the non-orthogonality of the eigenmodes makes interpretation of the results unwieldy; the seemingly largest amplitude modes are pairs of nearly parallel vectors which largely cancel in the sum. This is illustrated in Fig. 3.1 where the time averaged square amplitudes, $\int |h^{(n)}(t)|^2 dt$, of all 8192 eigenvectors are plotted for wavevector $k_y\rho_i = 0.3, k_x\rho_i = 0.0$. The eigenvalue of the unstable mode is seen at the right of the figure (in yellow) and does not appear to be among the most prominent modes (red). This is, however, merely an artifact of the non-orthogonality of the largest amplitude modes.

Nonetheless, significant information can be gained from this kind of decomposition by considering separately the properties of the unstable mode and the collective

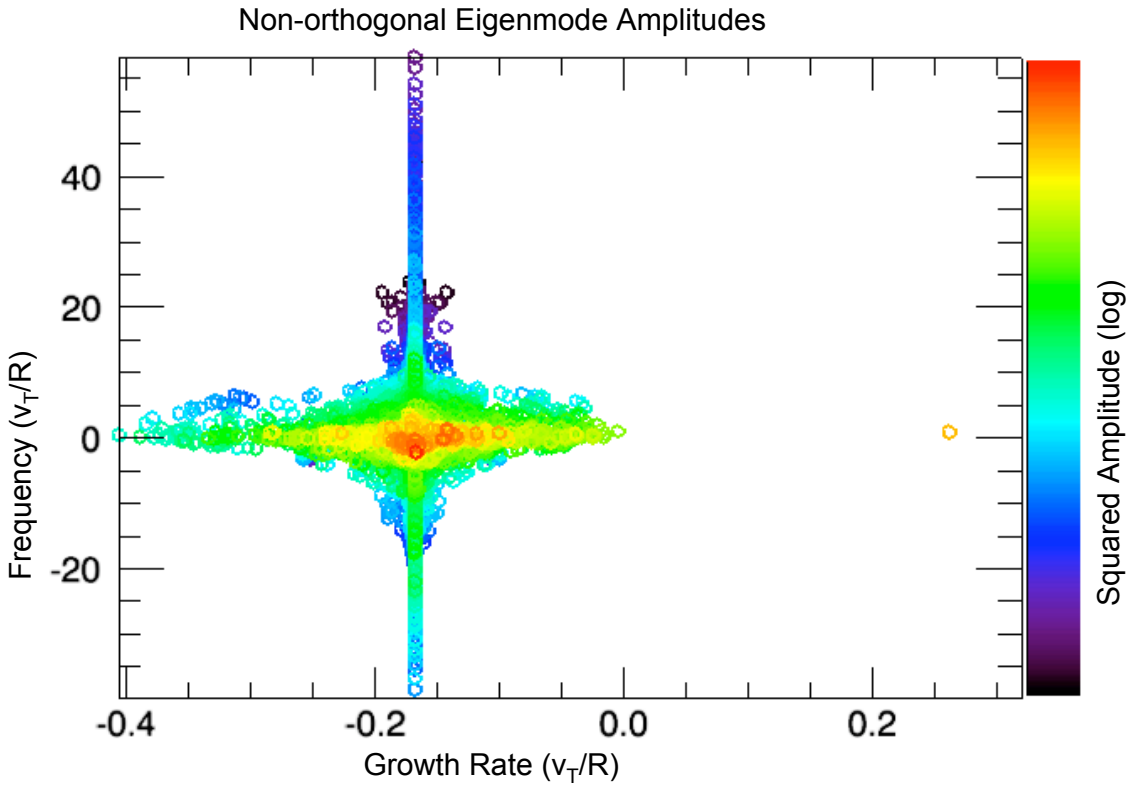

Figure 3.1: Plot of the time averaged squared amplitudes $\int |h^{(n)}|^2 dt$ of all eigenmodes in an eigenmode decomposition plotted on the complex plane defined by the mode growth rates and frequencies. The large amplitudes in the central part of the 'cloud' are due to a high degree of non-orthogonality rather than being representative of the importance of the eigenmodes to the dynamics.

properties of the subdominant modes. This defines a modified decomposition,

$$g_{k_x,k_y}(z,v_{||},\mu,t) = f^{(1)}_{k_x,k_y}(z,v_{||},\mu)h^{(1)}_{k_x,k_y}(t) + f^{(res)}_{k_x,k_y}(z,v_{||},\mu)h^{(res)}_{k_x,k_y}(t), \tag{3.2}$$

where

$$f^{(res)}_{k_x,k_y}(z,v_{||},\mu)h^{(res)}_{k_x,k_y}(t) = \sum_{n>1} f^{(n)}_{k_x,k_y}(z,v_{||},\mu)h^{(n)}_{k_x,k_y}(t), \tag{3.3}$$

and is called the residual distribution function. The non-orthogonality between these two groups is very manageable - when quadratic quantities are calculated, the cross terms can be considered separately or alternatively grouped with the residual terms. This method was productively applied to analysis of the initial transient of developing ETG turbulence as modeled with a fluid model in Ref. (57).

3.3 Orthogonalized Linear Eigenmode Decomposition

In order to circumvent the problem of non-orthogonality, one can orthogonalize the linear eigenmodes using the Gram-Schmidt method (58). This requires an ordering of the eigenvectors. It has been found that starting with the unstable mode and orthogonalizing the eigenvectors in order of increasing damping rate produces an effective orthogonal basis set. With this basis set a mode decomposition can be constructed by operating with the basis vectors on the distribution function from a nonlinear simulation: $h^{(n)}(t) = \langle f^{(n)}(z,v_{||},\mu), g_{k_x,k_y}(z,v_{||},\mu,t)\rangle$. Application of this decomposition shows that the unstable mode is the dominant eigenmode in the nonlinear fluctuations. Other eigenmodes are also excited to significant amplitudes. The amplitudes of the eigenmodes decrease as the mode damping rates increase and also as the mode frequencies deviate from the frequency of the unstable mode. This is

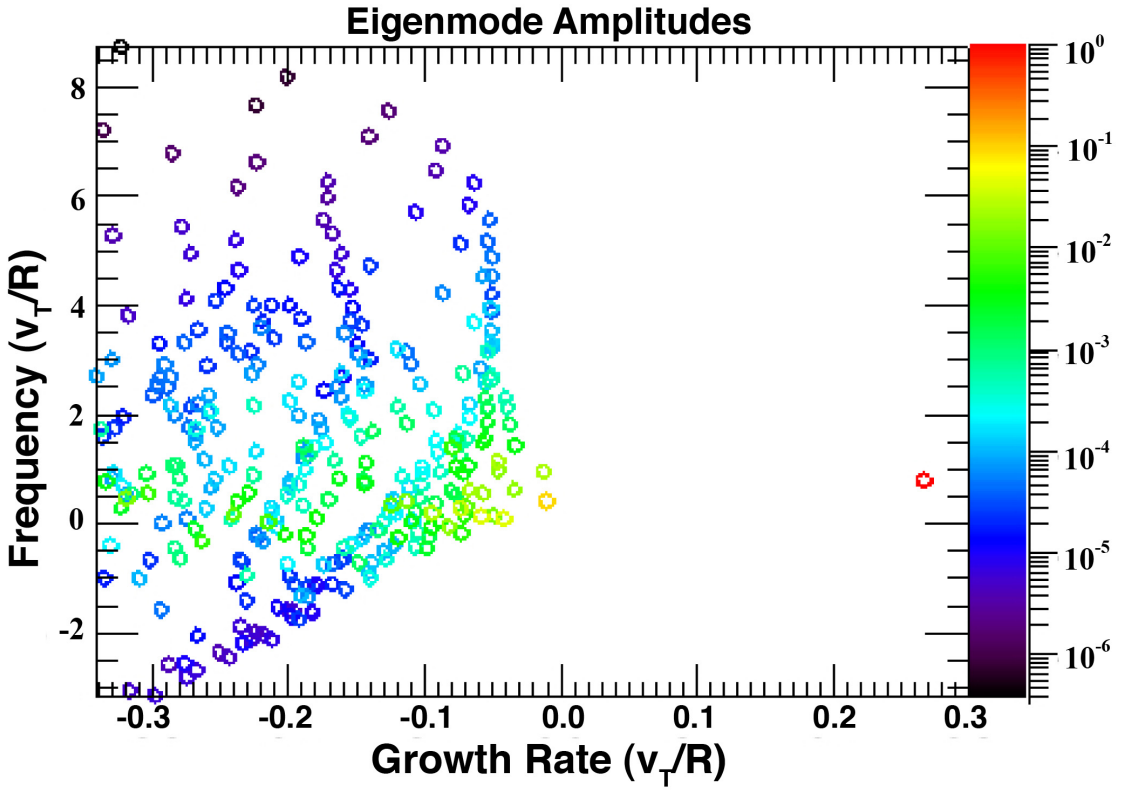

Figure 3.2: Plot of the squared mode amplitudes of the 315 (of 8192) least damped eigenmodes, orthogonalized in order of decreasing growth rate, for Fourier mode $k_y\rho_i = 0.3, k_x\rho_i = 0.0$ plotted in the plane defined by the mode growth rates and frequencies. The mode amplitudes decrease as damping rates increase and as the mode frequencies deviate from the unstable mode.

shown in Fig. 3.2 where the time-averaged eigenmode squared-amplitudes are plotted on the complex plane defined by the eigenmode frequencies and linear growth rates. This projection was performed for the 315 (of 8192) least damped modes for wavevector $(k_x\rho_i = 0.0, k_y\rho_i = 0.3)$ (results are similar for other important wavevectors). These 315 modes capture 83% of the fluctuation energy at this wavevector as shown in Fig. 3.3.

One drawback of the orthogonalization process is that it modifies the eigenvec-

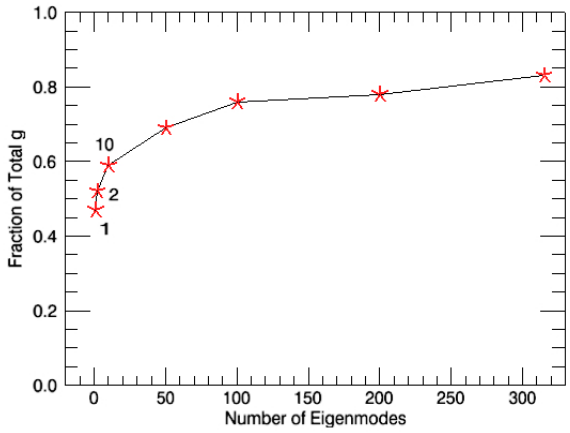

Figure 3.3: Plot of the fraction of the total energy captured by the first n eigenmodes in the orthogonalized eigenmode decomposition shown in Fig. 3.2. These 315 most weakly damped modes capture 82% of the energy.

tors - i.e., the orthogonalized eigenvectors are no longer eigenvectors of the linear operator. For the data described in the previous paragraph, it is expected that the orthogonalized vectors still have much in common with the original eigenvectors since the most severe non-orthogonality occurs for eigenvectors in a different part of the eigenvalue spectrum (see Fig. 3.1).

3.4 Proper Orthogonal Decomposition

Proper orthogonal decomposition (POD) can also be used to construct mode decompositions. POD has been used extensively in the hydrodynamic turbulence community (59), and more recently in plasma turbulence applications (60), (61). POD uses the singular value decomposition (SVD)(62) of a matrix to analyze fluctuation data. The SVD of a matrix is $A = U\Sigma V^{*T}$ where U is a unitary matrix whose columns are called left singular vectors, V is a unitary matrix whose columns are called right singular vectors, and Σ is a diagonal matrix whose elements (singular

values, s_n) indicate the relative importance of the orthonormal vectors making up U and V (more mathematical properties of the SVD Sec. 6.2). In order to construct a mode decomposition, each column of the input matrix A consists of a time slice, $g_{k_x,k_y}(z, v_{||}, \mu, t_i)$ at time t_i, of the nonlinearly evolved gyrokinetic distribution function for a selected wavevector. The non-spectral coordinates $(z, v_{||}, \mu)$ are 'vectorized' - unravelled to one dimension, e.g., as the data would be stored in computer memory. These distribution functions are pre-weighted in such a way that the scalar products in the SVD routine become equivalent to integrals over the coordinates:

$$g^{(weighted)} = g\sqrt{J(z)dzdv_{||}d\mu} \tag{3.4}$$

Now a standard numerical vector dot product is equivalent to a numerical integral over the coordinates:

$$\sum_{z,v_{||},\mu} g^{(weighted)*} g^{(weighted)} = \sum_{z,v_{||},\mu} J(z)dzd_{v_{||}}d\mu g^* g = \int\limits_{(numerical)} J(z)dzd_{v_{||}}d\mu g^* g \tag{3.5}$$

It would be desirable for the scalar products to produce the gyrokinetic energy, E, rather than merely an integral over the coordinates. However, the integrals that produce ϕ^2 in the wave energy cannot be reversed - i.e., it is not possible to recover distribution functions from the resulting POD modes.

Since this analysis is constructed in such a way that the non-spectral coordinates vary along the *columns* of the input matrix, the *left* singular vectors become the mode structures [$f^{(n)}(z, v_{||}, \mu)$ in Eq. 3.1]. Since the time coordinate varies along the *rows* of the input matrix, the *right* singular vectors become time traces of the amplitudes of the corresponding mode structures [these multiplied by the singular values correspond to $h^{(n)}(t)$ in Eq. 3.1]. By construction, the left singular vectors

are orthonormal under an integral over the coordinates, $\int f^{(i)^*} f^{(j)} J(z) dz dv_{||} d\mu = \delta_{i,j}$, where $J(z)$ is a Jacobian, and the right singular vectors are orthogonal under a time integral, $\int h^{(i)^*} h^{(j)} dt = s_i s_j \delta_{i,j}$. The orthogonality of the right singular vectors is a very useful property. For example, in Chap. IV, the contribution of each mode to the energy sources and sinks (Q_k and C_k, which are quadratic in the distribution function, g) is calculated. The POD modes are orthogonal under an integral over the coordinates, but are not necessarily orthogonal for the calculation of the energy terms. Taking a time integral activates the orthogonality of the time traces, $h^{(n)}(t)$, and extracts a distinct contribution of each mode to the energetics (this is discussed in more detail in Chap. IV). This is not possible for even an orthogonalized linear eigenmode decomposition.

Properties of the SVD ensure that the POD mode decomposition has the additional benefit of being 'optimal' in the following sense. This means that the POD decomposition captures more of the original data set (as measured by a Frobenius norm) in a truncated mode decomposition (i.e., a mode decomposition keeping only the first $r < N$ terms in the sum) than any other possible decomposition (see Sec. 6.2 for more details). Because of this property, a POD decomposition can be thought of as describing the data in the most efficient way, as opposed to forcing upon it a basis that may be quite unrelated to the the actual nonlinear dynamics. This property, along with the orthogonality of the right and left singular vectors makes the POD decomposition the most useful of the decompositions discussed in this section. The majority of the results in this thesis rely on POD mode decompositions. The remainder of this section will discuss general observations of POD mode decompositions of ITG turbulence data. The next two chapters will apply these mode decompositions to understanding saturation and magnetic fluctuations in ITG turbulence.

The POD decomposition for the wavevector of peak transport, $k_x \rho_i = 0.0, k_y \rho_i =$

0.2 will be examined in detail. This is for a simulation of ITG turbulence using CBC parameters as listed in Table 2.1. The parallel boundary condition for flux tube geometry connects the parallel mode structure for a central k_x wavevector with higher k_x wavevectors at the same k_y (37). Three such connections are included in this analysis ($k_x\rho_i = 0.0$ and $\pm k_x\rho_i = 1.0$) in order to extend the parallel mode structure beyond one poloidal circuit. It is observed that the $n = 1$ POD mode is very similar to that of the unstable eigenmode. The parallel mode structure of the electrostatic potential for this POD mode is shown in Fig. 3.4 A where the solid line represents the real part of the mode structure and the dashed line is the imaginary part. A scalar product $|\langle f^{(1)}, f^{unstable}\rangle|$,between the two provides a measure of similarity. This scalar product is typically above 0.9 (out of 1.0 for identical vectors) for wavevectors with strongly unstable eigenmodes. This is simply a verification of the expectation that the unstable eigenmode is the dominant structure in the nonlinear state. In the following chapters the $n = 1$ POD mode and the unstable linear eigenmode will often be conceptually equated, though it should be remembered that they are not necessarily exactly equivalent. In contrast to the unstable mode, the $n = 2$ POD mode exhibits odd parity about the outboard midplane, as can be seen in Fig. 3.4 B. This is the electrostatic version of electromagnetic modes with tearing parity that will be discussed in detail in Chap. V. This mode is also similar to a linear eigenmode - in this case the least damped eigenmode with negative growth rate. A comparison of the two electrostatic potential mode structures is shown in Fig. 3.5. The mode structures of additional POD modes ($n = 9$ and $n = 50$) are shown in Figs. 3.4 C and D. It is seen that finer scale structure develops as n increases. The $v_{||}$ dependence of the mode structures is shown in the right column of Fig. 3.4. It is observed that the $v_{||}$ structures have many features in common with the mode structures in z; they share the same parity (even or odd about $v_{||} = 0$) as the corresponding parallel structure

and also develop corresponding fine scale features as n increases. This development of fine scale structure is also illustrated in Fig. 3.6 where mode by mode Fourier spectra in the z, and $v_{||}$ coordinates are plotted. For the parameters studied here very little structure develops in the μ coordinate. The spectrum of singular values shown in Fig. 3.4 I indicates the relative amplitude of each of these modes in the nonlinear state. The spectrum decreases rapidly up to $n \sim 100$ followed by a region of weak exponential decay.

In order to illustrate how these modes reconstitute the nonlinear state, Fig. 3.7 shows the parallel mode structure for the electrostatic potential at a point in time when the mode structure deviates strongly from that of the unstable mode. In Fig. 3.7 the full decomposition is compared with a series of truncated decompositions - decompositions keeping all terms up to a number r. Fig. 3.7 A shows the $n = 1$ truncation, which deviates strongly from the nonlinear structure. The $n \leq 2$ truncation (shown in Fig. 3.7 B) captures much of the trend in the nonlinear structure but significant discrepancy remains. The $n \leq 100$ truncation reproduces the full structure very closely, as can be seen in Fig. 3.7 D.

The time amplitudes, $h^{(n)}(t)$, from the POD decomposition exhibit broadband frequency spectra which correspond closely (for low n) to the frequency spectra that would be calculated for a field such as the electrostatic potential. The time amplitudes for the $n = 1$ and $n = 100$ POD modes are shown in Figs. 3.8 A,B along with the frequency spectra for all the normalized modes in Fig. 3.8 C where it is seen that the modes are associated with increasingly fast time scales as n increases.

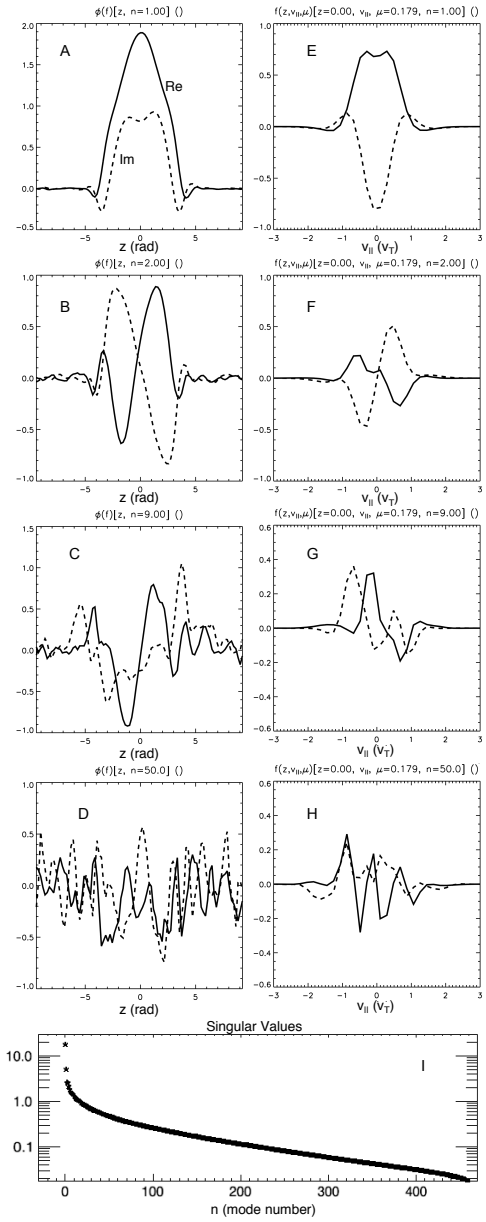

Figure 3.4: Plot of the mode structures of a POD decomposition of the wavevector $k_x\rho_i = 0.0, k_y\rho_i = 0.2$. Solid lines indicate the real part and dashed lines indicate the imaginary part. The parallel mode structures of the electrostatic potential are shown in the left column (A-D) for selected POD mode numbers. The structures in $v_{||}$ are shown in the right column (E-H). Fine scale structure develops as n increases. Solid lines indicate the real part and dashed lines indicate the imaginary part. The singular values which indicate the amplitude of each mode are shown in Fig. I.

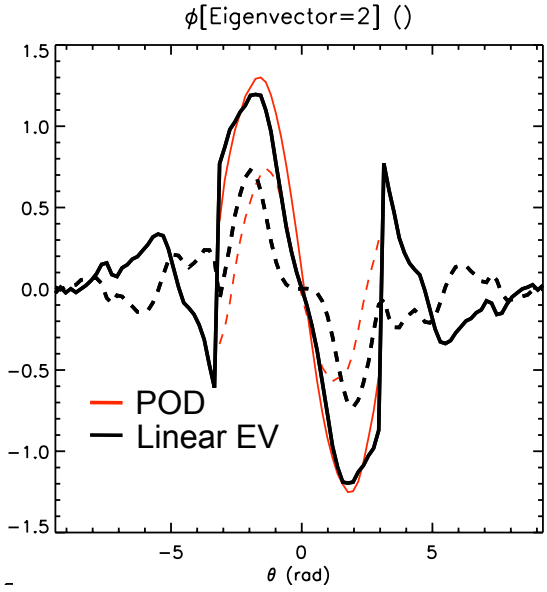

Figure 3.5: Plot of the parallel mode structure of the electrostatic potential for the $n = 2$ POD mode (red) and the least damped stable linear eigenmode (black).

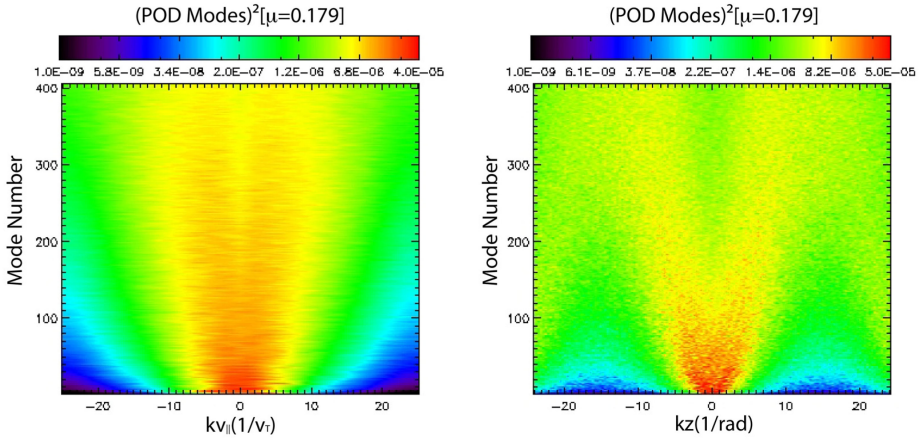

Figure 3.6: The $k_{v_{||}}$ spectrum summed over k_z (left) and k_z spectrum summed over $k_{v_{||}}$(right) of 406 normalized POD modes for wavenumber $k_y = 0.2$, $k_x = 0.0$ (two k_x connections). The modes achieve increasingly fine scale structure at high mode number.

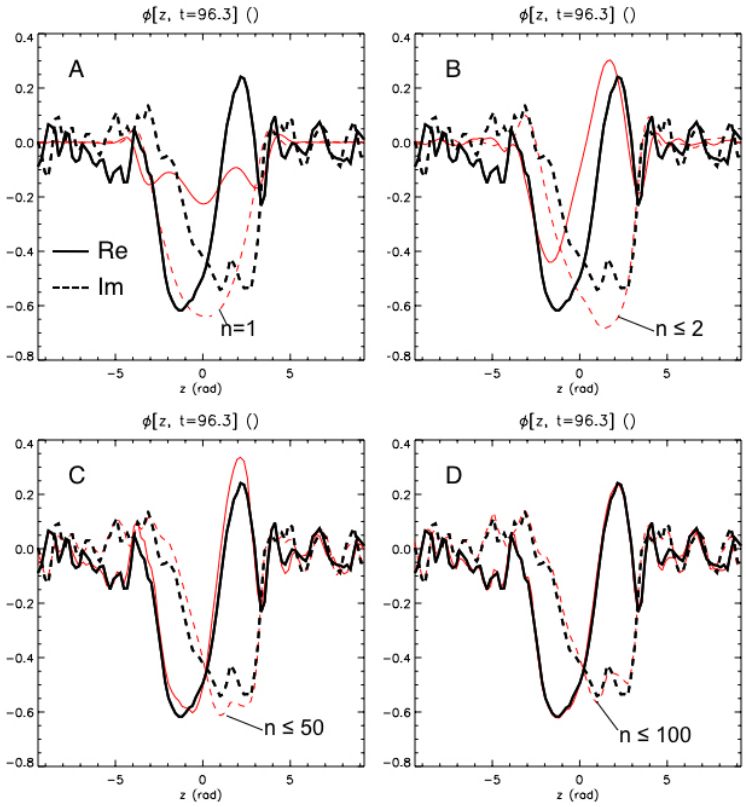

Figure 3.7: Demonstration of a POD decomposition reproducing the nonlinear state at a moment in time when the nonlinear mode structure deviates strongly from the unstable mode structure. The full decomposition (black) is compared against truncated decompositions (red) of rank 1, 2, 50, and 100 for Figs. A-D respectively.

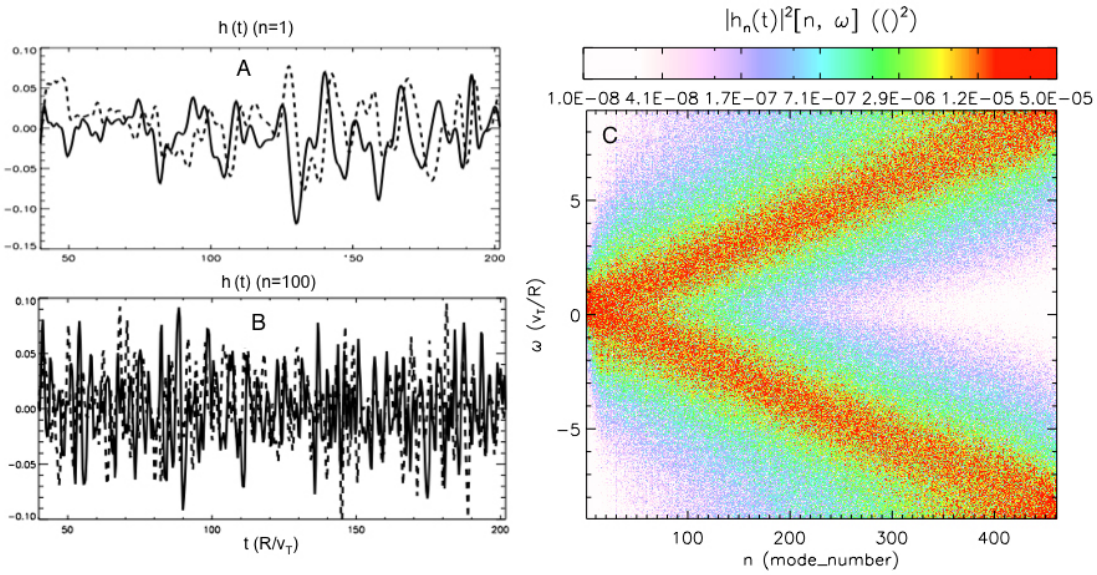

Figure 3.8: Plot of the POD time traces for $n = 1$ (A) and $n = 2$ (B). Fig. C shows the frequency spectrum for each mode demonstrating that the time scale increases with n.

3.5 Summary

In summary, a mode decomposition of the form of Eq. 3.1 is an analysis tool that facilitates a characterization of the complex fluctuations in the phase space, $(z, v_{||}, \mu)$, of nonlinearly developed gyrokinetic distribution functions. Two methods of constructing a mode decomposition are discussed.

First, the distribution function can be projected onto the basis of linear eigenmodes. However, the non-orthogonality of the eigenmodes makes this decomposition difficult to interpret. To get around this problem, the eigenvectors can be orthogonalized using the Gram-Schmidt method. This produces a basis set that is still strongly connected to the linear eigenmodes and their associated frequencies and growth rates. An orthogonalized linear eigenmode decomposition of gyrokinetic data reveals that the unstable mode is the dominant structure in the turbulence. Damped modes are also excited to significant amplitude. The mode amplitudes of damped modes decrease as the mode damping rates increase and the mode frequencies deviate from that of the unstable mode.

Proper orthogonal decomposition constructs a basis set from a matrix decomposition (SVD) of the nonlinear data. This basis set is optimal in that it reproduces the data more efficiently than any other possible basis set. It also has the useful property of producing basis functions *and* time traces that are orthogonal. This make it possible to define distinct contributions from each mode to quadratic physical quantities. POD decompositions of gyrokinetic data demonstrate the excitation of a hierarchy of modes. The dominant mode is very similar to the unstable eigenmode. The subdominant modes develop successively finer scale structure in the z and $v_{||}$ coordinates. The time histories of these modes are characterized by increasingly fast time scales as mode number increases.

CHAPTER IV

Role of Subdominant Modes in Saturating Turbulence

4.1 Introduction - the Kolmogorov Saturation Paradigm and Dissipation at Small Scales

A familiar turbulence paradigm, which describes the saturation of homogeneous high Reynolds number hydrodynamic turbulence, is the Kolmogorov paradigm (63): Fluctuation energy is injected into the turbulence at large scales. This energy cascades through a broad inertial range of scales where conservative nonlinear energy transfer dominates - i.e., very little energy is injected or dissipated from the fluctuations. At very small scales viscous effects dominate and the energy is dissipated. The processes that inject energy occur at distinct scales from the processes that dissipate the energy, as is illustrated schematically in Fig. 4.1. The turbulence saturates when the rate of energy injection at large scales is balanced by the rate of energy dissipation at small scales. Many aspects of this saturation paradigm have features in common with theories describing saturation in plasma microturbulence. In two dimensional, small scale ($k_\perp \rho_i \gg 1$), homogeneous plasma turbulence, saturation occurs via a dual cascade in perpendicular spatial scales and velocity space (μ in this case) (64), (65),

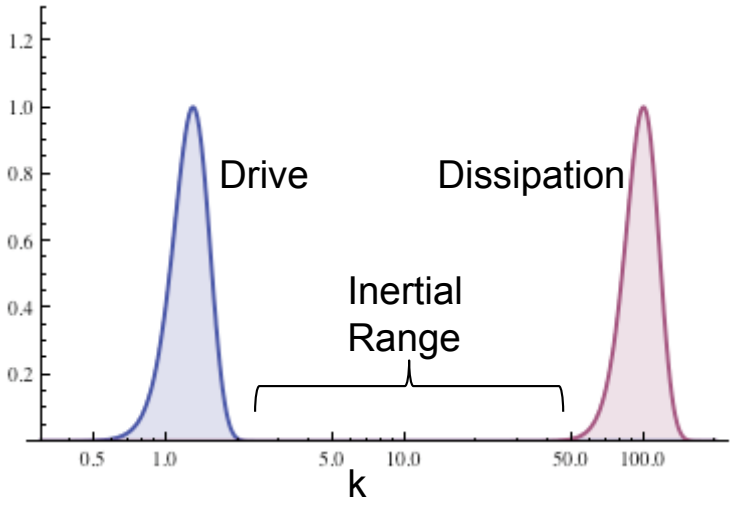

Figure 4.1: Schematic diagram of the typical hydrodynamic saturation scenario. The scale ranges of the drive and dissipation are separated by a broad inertial range. Contrast this with Fig. 4.2 which shows the analogous picture for gyrokinetics.

(66). Another example is the concept of turbulent suppression due to shearing by zonal flows whereby energy is transferred to small radial scales (67). In contrast to the Kolmogorov paradigm, and other saturation scenarios that emphasize small scale dissipation, here we will show that toroidal ITG driven turbulence saturates largely due to dissipation on subdominant modes at large perpendicular scales - the same scale range as the driving instabilities. The results in this chapter follow closely the presentation in Refs. (68) and (69).

4.2 Saturation of ITG turbulence - Dissipation at Large Perpendicular Scales

In this section, the role of damped modes in relation to energy balance and saturation of the turbulence will be examined. Details of the gyrokinetic energy quantity are described in Secs. 2.3 and 2.4. The energy is defined in Eq. 2.14, and its time

evolution equation is shown in Eq. 2.16. The data set used in this section uses the CBC parameters as defined in Table 2.1 with the exception that here we use a linearized Landau-Boltzmann collision operator, rather than exclusively artificial dissipation, in order to model physical dissipation processes. The collision frequency is $\nu(R/v_T) = 3.0 \times 10^{-3}$ which is much less than the dynamic time scales of the system. In these runs C_k is dominated by collisional dissipation but also includes contributions from fourth order hyper-diffusive dissipation in the z and $v_{||}$ coordinates. The perpendicular box size is $(L_x, L_y) = (126\rho_i, 126\rho_i)$, and the number of grid points is $48 \times 48 \times 8$ for the $(z, v_{||}, \mu)$ coordinates respectively. The perpendicular spatial resolution consists of 128 grid points in the x direction giving $k_{x,max}\rho_i = 3.12$, and 64 k_y Fourier modes for $k_{y,max}\rho_i = 3.15$. In this section, POD decompositions are applied to only a single k_x value, omitting higher k_x connections, in order to isolate dissipation at small scales from dissipation at large scales.

The scale dependence of the energy terms is shown in Fig. 4.2 where the drive Q and dissipation C are plotted as a function of k_x summed over k_y (A) and a function of k_y summed over k_x (B). The scales of peak drive and dissipation overlap and there is no inertial range of scales. Contrast this with the analogous picture for high Reynolds number hydrodynamic turbulence where the drive is localized at large scales, the dissipation is localized at small scales and there is a broad inertial range with no energy injection or dissipation.

The POD decomposition facilitates the calculation of the contribution of individual structures to the terms in the energy equation at each scale (k_x, k_y). The energy quantities, Q and C, are quadratic in the distribution function g, so some sort of orthogonality is necessary in order to isolate the impact of each mode. Recall that, as discussed in Sec. 3.4, the POD mode structures $(f^{(n)})$ are orthogonal under an integral over the non-spectral coordinates $(z, v_{||}, \mu)$, but this does

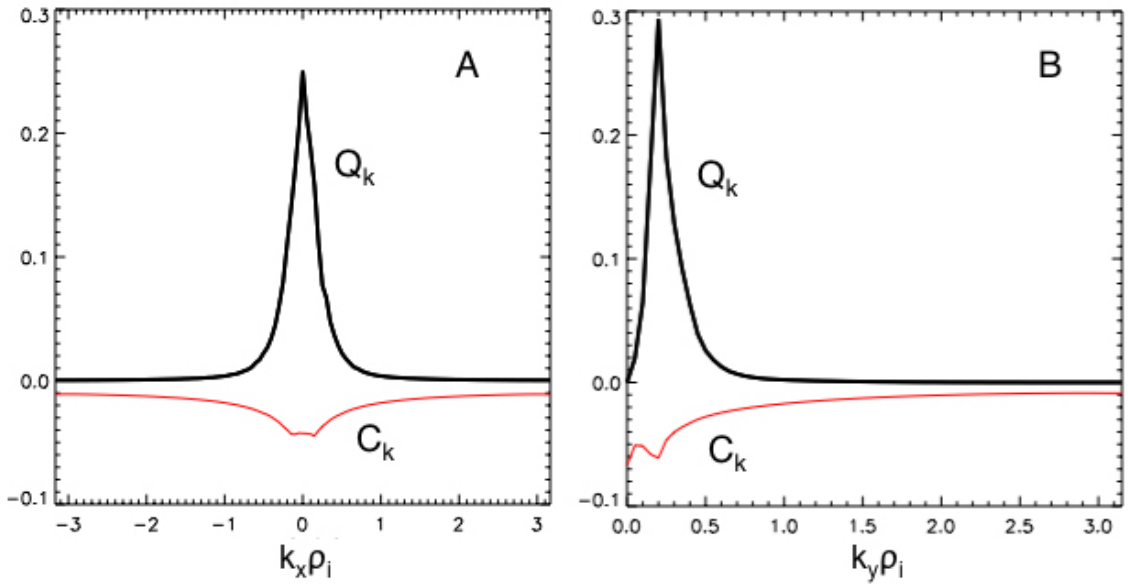

Figure 4.2: Plot of the energy drive Q_k and dissipation C_k averaged over z and time, as a function of k_x (summed over k_y) (A) and k_y (summed over k_x) (B). The drive and dissipation peak at the same scales.

not guarantee orthogonality under other operations like Q and C. Fortunately the *right* singular vectors, $h^{(n)}(t)$, are also orthogonal. Thus taking a time integral isolates distinct contributions from each mode to the total energy quantities, e.g., $\int C_k(g_{total})dt = \sum_n C_k(f^{(n)}) \int |h^{(n)}(t)|^2 dt$.

In order to get a picture of the k-dependence of the energetics, mode decompositions are explored over a scan of wavevectors centered about the peak of the spectrum - $k_x\rho_i = 0.0, k_y\rho_i = 0.2$. The unstable mode achieves its largest amplitude (in an absolute sense as well as in relation to subdominant modes) at this peak wavenumber. As a result, this scan can be thought of as defining a lower bound on the magnitude of the effects of subdominant modes in relation to the effect of the unstable mode. The scan consists of a series of increasing k_x values at $k_y\rho_i = 0.2$, and a scan of k_y values at $k_x\rho_i = 0.0$. The mode by mode dissipation, $C_k(f^{(n)}) \int |h^{(n)}(t)|^2 dt$, is shown for a subset of the k_y scan in Fig. 4.3 (top), and for the k_x scan in Fig. 4.3 (bottom).

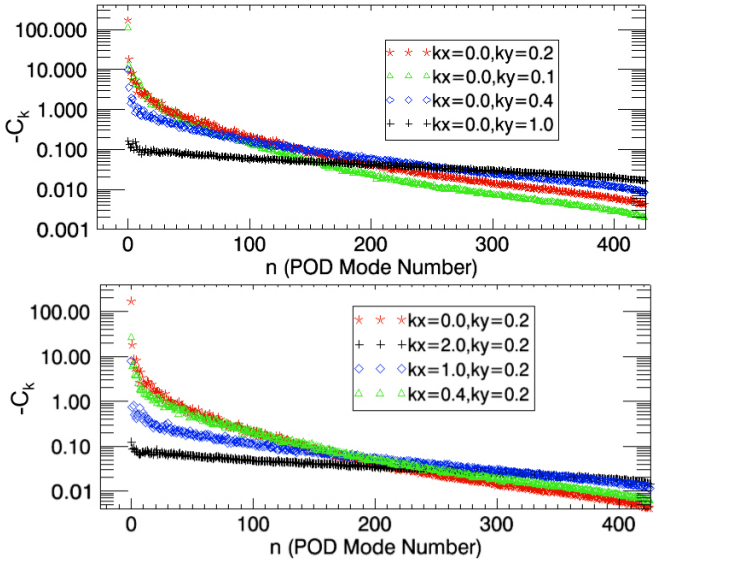

Figure 4.3: Plot of the mode by mode dissipation $C_k(f^{(n)}) \int h^{(n)}(t)^2 dt$ for a range of k_y values at $k_x\rho_i = 0$ (top) and a range of k_x values at $k_y\rho_i = 0.2$. A large number of modes contribute to the dissipation.

This quantity drops off steeply at low n and decreases exponentially at high n. A large number of modes contribute a non-negligible fraction to the dissipation. The decreasing dependence on n is due to the drop-off in the mode amplitudes (singular value spectrum, as seen in Fig. 4.4 A). The dissipation rate $C_k(f^{(n)})$ for each normalized mode (i.e., using the mode structures without amplitude information) is smallest for $n = 1$ and strongly increases with n as seen in Fig. 4.4 C. This is because of a transition from smooth, large scale velocity space structure at low n to increasingly fine scale velocity space structure as n increases (as demonstrated in Figs. 3.4 and 3.6). Only when amplitude information is included in the calculation of C_k is the decreasing n-dependence shown in Fig. 4.3 recovered. The mode by mode behavior of the energy drive, Q_k, is shown in Fig. 4.4 and will be discussed below.

In order to demonstrate that the k-dependence of the dissipation (peaking at large perpendicular scales as shown in Fig. 4.2) is due to the excitation of subdominant

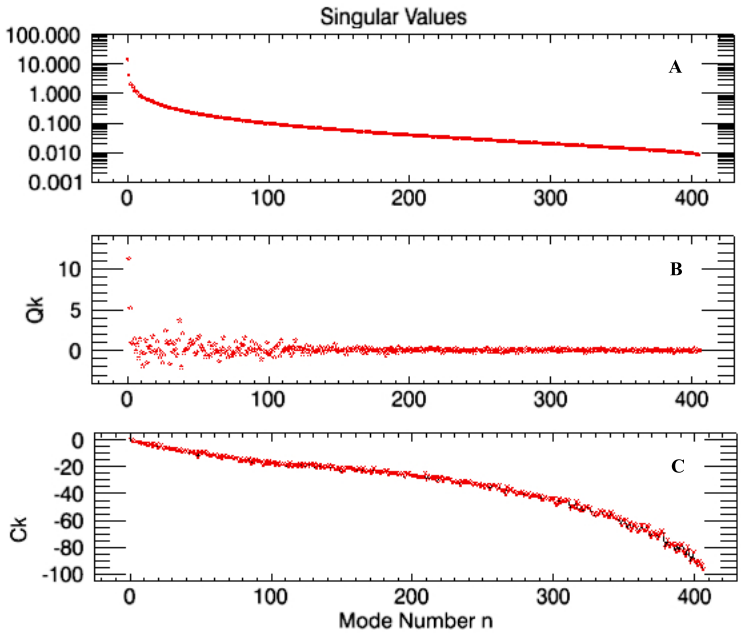

Figure 4.4: The spectrum of singular values (A), energy drive Q_k for each normalized POD mode (B), and dissipation C_k for each normalized mode (C). For $k_y\rho_i = 0.2, k_x\rho_i = 0.0$.

modes, one must separate the dissipation associated with the $n = 1$ mode from the dissipation associated with subdominant ($n > 1$) modes. This is shown in Fig. 4.5 for the wavevector scan described above. The red squares indicate the total dissipation at certain wavevectors. The green plus signs indicate the dissipation associated with the $n = 1$ mode and the blue diamonds indicate the dissipation due to subdominant modes (the sum of all $n > 1$ in Fig. 4.5). The dissipation due to the $n = 1$ mode is comparable to the $n > 1$ dissipation only near the peak in the spectrum where the $n = 1$ mode achieves its largest relative amplitude. In other regions the $n > 1$ modes dominate the dissipation and in aggregate define the dominant energy sink. Note that the $n = 1$ mode has the smallest dissipation rate $[C_k(f^{(1)})]$; its net dissipation, $C_k(f^{(1)}) \int |h^{(1)}(t)|^2 dt$, is significant only because of its large amplitude. Also, the significant dissipation associated with the $n = 1$ mode is not inconsistent with its role as the driving instability; the energy drive, $Q_k(f^{(1)}) \int |h^{(1)}(t)|^2 dt$, associated with this

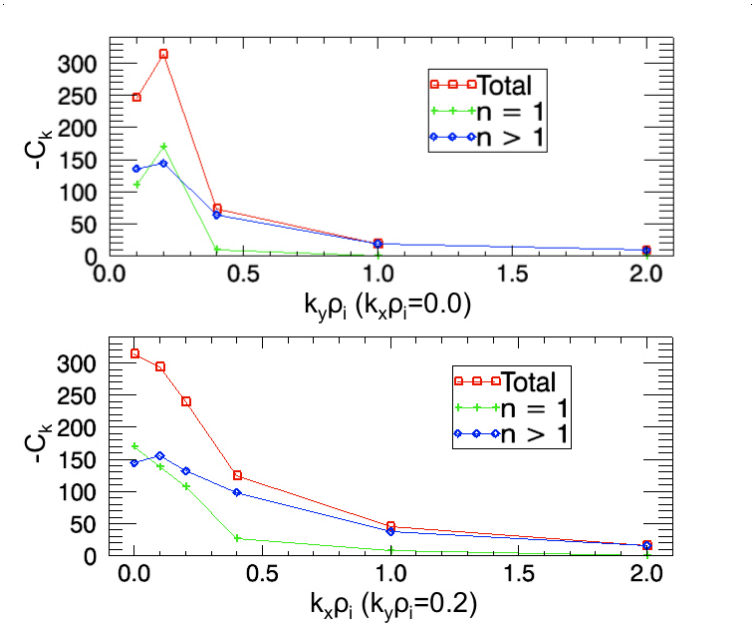

Figure 4.5: Plot of the dissipation $C_k(f^{(n)}) \int h^{(n)}(t)^2 dt$ for all modes (red squares), the $n = 1$ mode (green plus signs), and all $n > 1$ modes (blue diamonds), for a range of k_y values at $k_x\rho_i = 0$ (top) and a range of k_x values at $k_y\rho_i = 0.2$. The dissipation due to subdominant ($n > 1$) modes is the dominant contribution.

mode far outweighs its dissipation.

In contrast with the above results for the dissipation C_k, performing the same analysis on the energy drive Q_k reveals that it is dominated by the $n = 1$ mode. The contribution to the energy drive of $n > 1$ modes is positive and typically less than 5% of that of the $n = 1$ mode for the most important wavevectors. Beyond $n \sim 3$ the drive rates, $Q_k(f^{(n)})$, are randomly distributed about zero (as illustrated in Fig. 4.4 B) - i.e., some modes drive an inward heat flux, other modes drive an outward heat flux and in sum these modes produce very little net transport. It is expected that in situations like this, certain quasilinear estimates could be meaningful in spite of the active participation of subdominant modes in the fluctuation spectrum. This result is very different from the behavior of damped modes in fluid models, where damped modes usually contribute significant inward fluxes and strongly reduce transport levels

from quasilinear expectations (26)-(28).

It should be noted that, although the direct contribution of damped modes to the net transport is quite small, this is not an indication that they are insignificant with regard to transport. In Sec. 7.3.2 it is described how the excitation of subdominant modes decreases transport levels from certain quasilinear estimates even when the flux due to subdominant modes is positive (outward). This occurs when subdominant modes drive transport at a rate less than that of the unstable mode so that the net transport associated with a given degree of turbulent intensity is less than the transport that would occur if the same amount of intensity resided solely in the unstable mode.

Another likely role of damped mode excitation with relation to transport is as follows: In the absence of damped eigenmode excitation at large scales, a reorganization of the fluctuation spectrum would be necessary in order to facilitate a cascade transferring *all* the energy to small dissipative scales. This would almost certainly increase the transport levels, although an explicit demonstration of this has not yet been constructed. One only need look to the extensive literature on zonal flows for an example of a phenomenon which has no direct contribution to the transport, but plays a critical role in moderating the processes that do carry the transport (67).

4.3 Net Contribution of Modes to Energy Balance

Thus far in this section separate consideration has been given to the physical processes that are responsible for the energy drive, Q_k, and the energy dissipation, C_k. Another approach is to consider the *net* contribution to the energy balance, $[Q_k(f^{(n)}) + C_k(f^{(n)})] \int |h^{(n)}(t)|^2 dt$, for each mode in a mode decomposition. It is observed that a small number of subdominant modes have a net positive contribution

to the energy balance even for CBC parameters where there is one linearly unstable mode per wavevector. For example, the $n = 2$ POD mode has a value of $[Q_k(f^{(2)}) + C_k(f^{(2)})] \int |h^{(2)}(t)|^2 dt$ that is slightly positive ($\sim$ 2.5% of the value for the $n = 1$ mode for $k_x\rho_i = 0.0, k_y\rho_i = 0.2$) even though the most similar linear eigenmodes (modes with similar parallel mode structure) are weakly damped. In Figs. 4.6 A and C $[Q_k(f^{(n)}) + C_k(f^{(n)})] \int |h^{(n)}(t)|^2 dt$ is plotted over the wavevector scan for the unstable mode $n = 1$ (blue triangles) and for the sum of all modes with a net positive value of $[Q_k(f^{(n)}) + C_k(f^{(n)})] \int |h^{(n)}(t)|^2 dt$ (red asterisks). In Figs. 4.6 B and D this is plotted for all subdominant modes ($n > 1$) (blue triangles) and for all subdominant modes with net negative values of $[Q_k(f^{(n)}) + C_k(f^{(n)})] \int |h^{(n)}(t)|^2 dt$ (red asterisks). In Fig. 4.6 D the blue triangle at $k_x\rho_i = 0.1$ is slightly positive, indicating that for this wavevector the net effect of subdominant modes is a slight positive contribution to the energy balance (these effects are more pronounced when examined using a linear eigenmode decomposition). This is a variant of subcritical instability, which normally describes instability to finite amplitude perturbations in a system that is stable to perturbations of infinitesimal amplitude (70),(71). Here the system is unstable, or supercritical. At $k_x\rho_i = 0.1, k_y\rho_i = 0.2$ it is more unstable at finite amplitude (due to subdominant mode excitation) than it is at infinitesimal amplitude, where there is only the linear instability. At other wavenumbers the system is less unstable at finite amplitude, describing the relatively much larger role of subdominant modes in saturating the linear instability. Both effects were observed and described for a simpler fluid model of trapped electron mode turbulence (26).

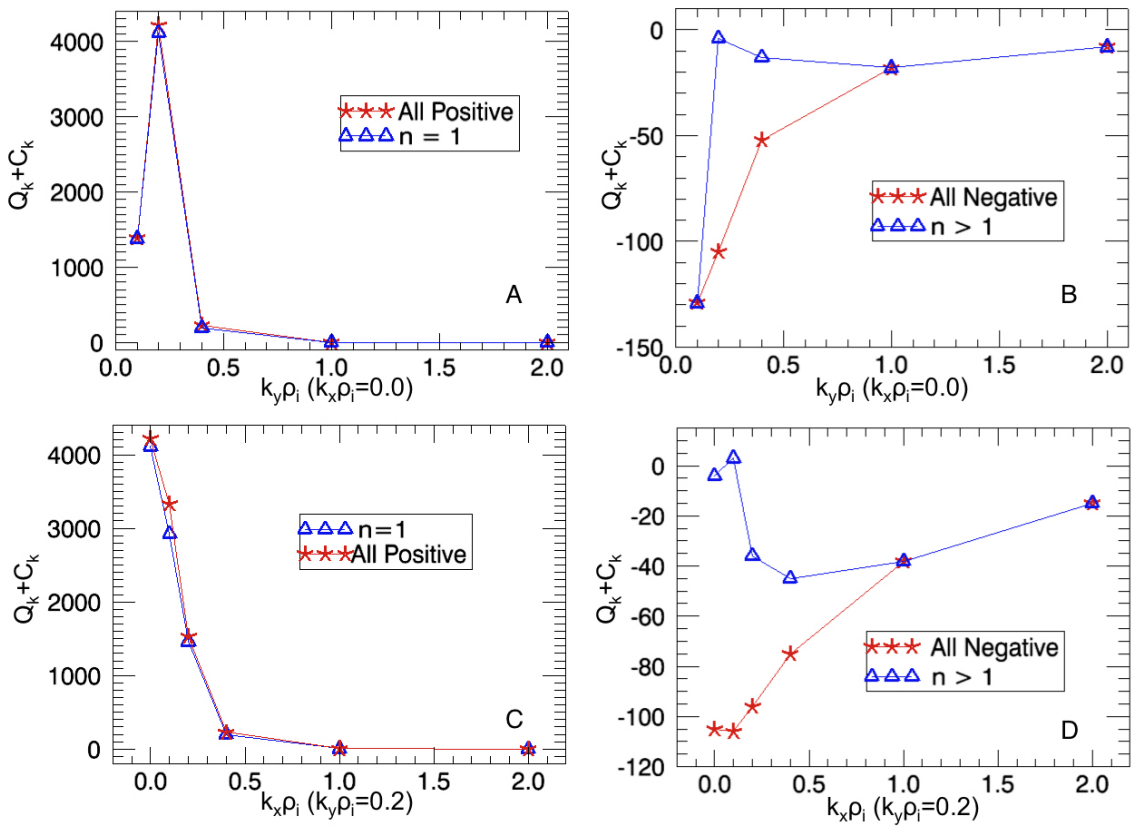

Figure 4.6: Plot of the net energy contribution, $(Q_k(f^{(n)}) + C_k(f^{(n)})) \int |h^{(n)}(t)|^2 dt$, of all modes with net positive values (red asterisks) and the $n = 1$ mode (blue triangles) in A and C. The slightly larger values of the red asterisks indicates the presence of some subcritical instability. In Figs. B and D the net energy contribution is plotted for the sum of all negative modes (red asterisks) and all $n > 1$ modes (blue triangles).

4.4 Equipartition of Amplitude Attenuation

This application of POD to the question of saturation mechanisms also reveals an underlying principle for the organization of damped mode excitation; for a certain range of mode numbers (typically $n \gtrsim 150$) a form of equipartition is observed. The mode amplitudes and dissipation rates balance in such a way that the quantity $s_n[Q_k(f^{(n)}) + C_k(f^{(n)})]$ clusters about a constant value for a broad range of mode numbers as seen in Fig. 4.7 (right). This phenomenon is termed equipartition of amplitude attenuation rate (72). Fig. 4.7 (left) shows the results of a calculation of the same quantity ($s_n[Q_k(f^{(n)}) + C_k(f^{(n)})]$) for a data set (from the same simulation) with time steps selected at a 2.5 times greater frequency. It is speculated that the equipartition occurs only among modes that are uncorrelated in time. A simplified analytic analysis predicts both this equipartition and the decrease at low n by assuming that the dominant nonlinear coupling is between the unstable mode and damped modes (rather than between damped modes). This sort of equipartition allows for a novel statistical treatment of damped eigenmode excitation that finds many parallels in statistical mechanical descriptions of an ideal gas. These concepts are currently being refined and developed.

4.5 Summary

In summary, POD decompositions have been used to examine the saturation of ITG driven turbulence. It is found that dissipation peaks at large perpendicular scales due to the excitation of damped modes at these wavenumbers. Damped modes dissipate energy through collisional dissipation. This is strongly activated by the fine scale structure in velocity space which characterizes the modes as n increases. Thus it is found that damped modes facilitate saturation, but in a very different way

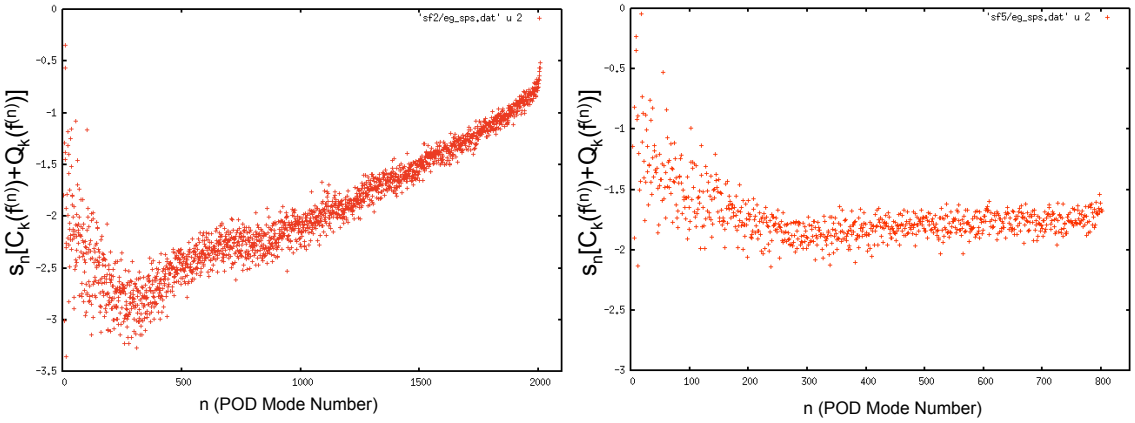

Figure 4.7: Plots demonstrating equipartition of amplitude attenuation rate. The decomposition which produced the results shown in the figure on the left (which does not exhibit equipartition) sampled time steps at a 2.5 times greater rate than that for the figure on the right (which does exhibit equipartition).

from the mechanism identified in fluid models. In fluid models the damped modes contribute to saturation by contributing strong inward transport fluxes. In contrast, the transport associated with the subdominant gyrokinetic POD modes largely cancel out so that the unstable mode is the only major contributor to the transport. A degree of subcritical instability is identified - structures that are expected to be linearly stable are found to produce a slight net contribution to the energy drive. Finally, a novel form of equipartition has been identified and is currently being explored in detail.

CHAPTER V

Role of Subdominant Modes in Magnetic Fluctuations

5.1 Introduction

In recent years, gyrokinetic studies have examined electromagnetic (finite β - the ratio of plasma pressure to magnetic pressure) effects in microturbulence for both ITG (73), (44) and CTEM (74). The ITG studies described in Refs. (73) and (44) consider an extension of CBC parameters consisting of a β-scan ranging from the electrostatic limit to $\beta \sim 0.01$. It was found that the ion heat transport decreases mildly over this scan. Electron heat transport can be divided into an electrostatic part (due to $E \times B$ advection) and an electromagnetic part (due to radial streaming along the perturbed magnetic field). It was found that that the electron heat transport was somewhat smaller than the ion heat transport. The electromagnetic electron heat flux starts from zero in the electrostatic limit and increases with a β^2 dependence up to $\sim \beta = 0.008$, at which point it is comparable to the electrostatic heat transport. It has recently been discovered that this modest electromagnetic heat transport is, somewhat surprisingly, accompanied by a high degree of magnetic stochasticity throughout the β-scan (75). This has been studied in depth for the extended CBC parameters where

the most unstable modes are not resonant and therefore unable to reconnect magnetic field lines. In this chapter the causes of this magnetic stochasticity are examined and it is concluded that the dominant underlying mechanism is the active presence of subdominant modes with tearing parity in the nonlinear fluctuation spectrum.

Much of the analysis in this chapter is applied to data from simulations that were first reported in Ref. (44). These simulations cover values of β ranging from 0.001 to ~ 0.1. The perpendicular box size is $(L_x, L_y) = (101\rho_i, 126\rho_i)$, and the number of grid points is $24 \times 48 \times 8$ for the $(z, v_{||}, \mu)$ coordinates respectively (for $\beta > 0.007$ the z resolution is increased to 48 grid-points). The perpendicular spatial resolution consists of 192 k_x modes and 24 (positive) k_y modes. In this chapter, a central point of $\beta = 0.003$ is used for the most detailed analysis.

This chapter will proceed as follows: In Sec. 5.2 symmetries of the gyrokinetic equation will be discussed in relation to resonant (tearing) and non-resonant mode structures. Linear analysis of subdominant modes with tearing parity will be described in Sec. 5.3. In Sec. 5.4 POD analysis is applied to the field data to determine what kinds of structures are excited in the nonlinearly developed turbulence. Finally, in Sec. 5.5 magnetic diffusion coefficients are calculated for the different structures that characterized the turbulence. A summary is provided in Sec. 5.6.

5.2 Tearing Parity and Symmetries of the Gyrokinetic Equations

The resonant component of a fluctuating magnetic vector potential, $A_{||}$, is extracted by integrating along the field line at a rational surface:

$$A_{||}^{res} = \langle A_{||}(x = x_{rat}(k_y), k_y, z)\rangle_z. \tag{5.1}$$

Thus, an $A_{||}$ mode structure that is odd about the outboard midplane ($z = 0$) has no resonant component and cannot contribute to magnetic reconnection. On the other hand, a mode with even parity for $A_{||}$ can be resonant. In this section, symmetries of the gyrokinetic equation and the resulting possible sources of resonant magnetic field fluctuations will be discussed.

Consider the special case of $k_x = 0$ for the gyrokinetic equation (see Appendix A). This special case is significant because it defines the scale where the growth rates of the micro-instabilities peak and also where the nonlinear spectra peak. As will be shown here, it also extracts symmetries in the gyrokinetic equation that are broken for $|k_x| > 0$. This selection of $k_x = 0$ reduces $k_\perp$ in the gyroaveraging operator, $J_0((\frac{2B0\mu}{m_j})\frac{k_\perp}{\Omega_j})$ to $k_\perp = \sqrt{1 + |\hat{s}z|}k_y$ - an even function of z. In addition, the k_x curvature term, $v_d K_x i k_x \Gamma_j$ goes to zero. Now consider the linear eigenvalue problem that defines the linear eigenmode structures, growth rates, and frequencies,

$$\mathcal{L}[g_{k_x,k_y}] = \omega_{k_x,k_y} g_{k_x,k_y} \tag{5.2}$$

Since, ω_{k_x,k_y} is a scalar, whatever symmetries are present in g must also be present in $\mathcal{L}[g]$. It can be shown that every term in the linear operator, $\mathcal{L}$, exhibits the following symmetry: $\mathcal{L}(z, v_{||}) = \mathcal{L}(-z, -v_{||})$. As an illustration of this, the parallel advection term can be schematically represented as

$$\begin{aligned} & v_{Tj} v_{||} \left(\frac{\partial g_j}{\partial z} + \frac{qF_{0j}}{T_{0j}} \frac{\partial \chi_j}{\partial z} + v_{Tj} v_{||} \frac{qF_{0j}}{T_{0j}} \mu \partial_z B_0 A_{||} \right) \\ \rightarrow\ & v_{||} \partial_z [g] + v_{||} F_0 \partial_z [J_0(|z|)\Phi[g] + v_{||} J_0(|z|) A_{||}[g]] + v_{||}^2 F_0 \partial_z B_0 A_{||} \end{aligned} \tag{5.3}$$

where only coefficients that contain $z, v_{||}$ dependence are retained. From the following properties one can see that the even symmetry is maintained in each term: $B_0(-z) =$

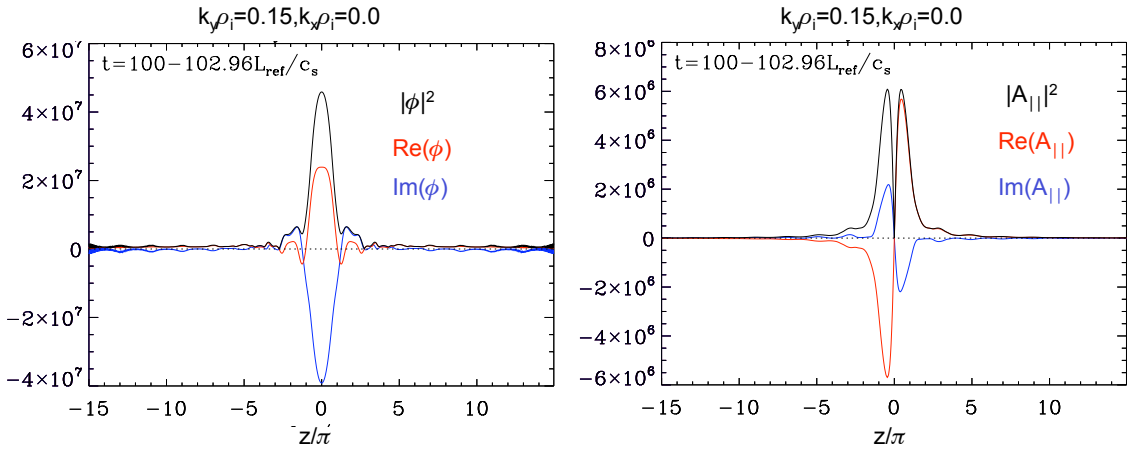

Figure 5.1: Linear mode structures of the electrostatic potential (A) and parallel magnetic vector potential (B) of the most unstable linear eigenmode at $k_y\rho_i = 0.15, k_x\rho_i = 0.0$. The potential is even about $z = 0$ and the magnetic vector potential is odd (non-resonant).

$B_0(-z)$ (see Eq. A.6), $F_0(-z, -v_{||}) = F_0(z, v_{||})$ (see Eq. A.6), $v_{||}\partial_z = (-v_{||})\partial_{-z}$, $J_0(|z|) = J_0(|-z|)$, $\Phi[\cdot](z, v_{||}) = \Phi[\cdot](-z, -v_{||})$, as can be seen in Eq. A.8, and $v_{||}A_{||}[\cdot](z, v_{||}) = (-v_{||})A_{||}[\cdot](-z, -v_{||})$, as can be seen in Eq. A.9. Similar analyses demonstrate that each term in the gyrokinetic equation has this same property. As such, every linear eigenmode at $k_x = 0$ must exhibit either even parity, $g(z, v_{||}) = g(-z, -v_{||})$, or odd parity, $g(z, v_{||}) = -g(-z, -v_{||})$. In addition, if the eigenmode has even parity, then its corresponding electrostatic potential structure is even about the outboard midplane, and its parallel magnetic vector potential structure is odd about the outboard midplane (due to the $v_{||}$ in the integral shown in Eq. A.9). For the parameter space covered by the extended-CBC β-scan, the most unstable mode at every binormal wavenumber belongs to the class of even parity solutions with even ϕ structures and odd (non-resonant) $A_{||}$ structures. An example of this is shown in Fig. 5.1 for $k_y\rho_i = 0.15, k_x\rho_i = 0.0$, at $\beta = 0.008$.

At $|k_x| > 0$ the symmetry is no longer perfectly enforced. This is due to terms

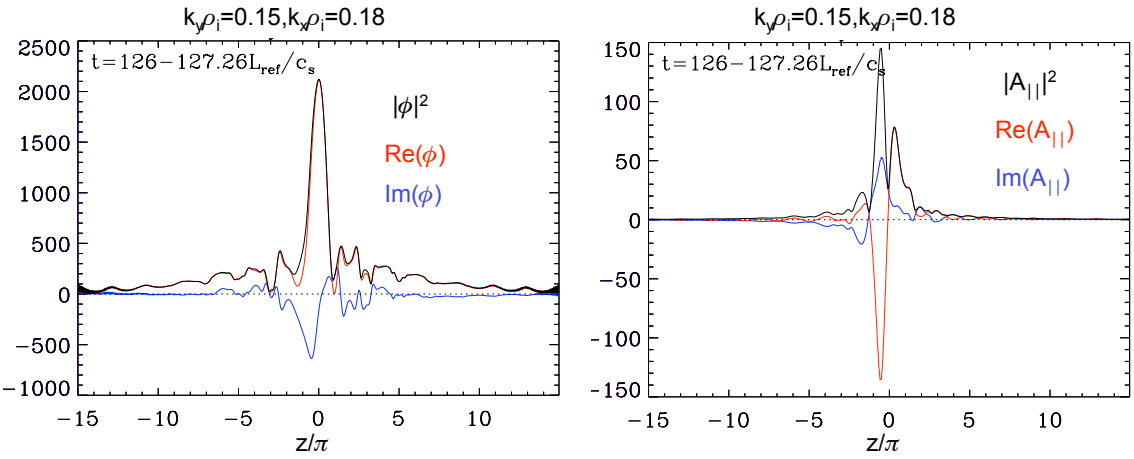

Figure 5.2: Linear mode structures of the electrostatic potential (A) and parallel magnetic vector potential (B) of the most unstable linear eigenmode at $k_y\rho_i = 0.15, k_x\rho_i = 0.18$. The magnetic vector potential is no longer perfectly odd about $z = 0$ so that there exists a resonant component.

with odd z dependence in both the gyro-average operator, $J_0((\frac{2B0\mu}{m_j})\frac{k_\perp}{\Omega_j})$, where $k_\perp^2 = (k_x+\hat{s}zk_y)^2+k_y^2$, and also the radial curvature term, $v_d K_x i k_x \Gamma_j$, where $K_x = -\sin(z)$. For $|k_x| > 0$, the most unstable modes still tend to retain a dominant element of even parity. The corresponding $A_{||}$ structures exhibit predominantly odd parity, but there remains a resonant component as well. An example of this is shown in Fig. 5.2 for $k_y\rho_i = 0.15, k_x\rho_i = 0.18$, at $\beta = 0.008$.

One could imagine a situation where the $|k_x| > 0$ unstable modes would combine to maintain the even parity. Consider a pair of degenerate (same frequency and growth rate) unstable eigenmodes, one at $+k_x$, and the other at $-k_x$ (for an up-down symmetric equilibrium, this would not be unexpected). Since these modes are degenerate, their superposition would also be a solution to the linear eigenproblem. The $A_{||}$ mode structures of these modes could plausibly mirror each other in such a way that they would maintain a net non-resonant mode structure: $A_{||_1}(z) = -A_{||_2}(-z)$. This would be an appealing way to extend symmetry properties to finite k_x modes.

However, there are two problems with this. First, in the nonlinear state there would be no linear coupling between these modes - i.e., they would often attain different amplitudes at different times, thus breaking the symmetry. Second, Fourier transforming back to direct space (x, y) would extract a component that would necessarily break the symmetry: in the expression $A_{||_1}(z)e^{ik_x x} + A_{||_2}(z)e^{-ik_x x}$, the $\cos(k_x x)$ terms would maintain the symmetry but the $\sin(k_x x)$ terms would not.

In summary, there are two possible sources of resonant magnetic fluctuations: subdominant modes with tearing parity and unstable modes at $k_x > 0$. In Sec. 5.5, I will examine the impact of each of these on the perturbed magnetic field and show that subdominant modes are the dominant cause of magnetic stochasticity.

5.3 Linear Eigenmodes with Tearing Parity

In the previous section it was established that solutions to the linear eigenmode problem at $k_x = 0$ exhibit even or odd parity. The most unstable modes are characterized by even parity. It is of interest to explore the properties of subdominant linear eigenmodes with odd (tearing) parity. This is done using the GENE eigenmode solver (56). The GENE code can apply three different solution methods to the linear gyrokinetic problem. First is the standard initial value solution which can only find the most unstable mode at each wavevector. Second, is a package of iterative eigenvalue solvers, SLEPc (76). These are efficient at solving for 'fringe' eigenvalues (eigenvalues with the largest real or imaginary parts of all the solutions) but can often struggle finding solutions where several eigenvalues have similar values. The third method is unique to the GENE code - a scalable direct solver which uses a routine in the SCALAPACK (77) library to solve for all eigenvalues and eigenvectors of the linear operator. This is a powerful tool, but the algorithm scales poorly ($\mathcal{O}(N^3)$), (where

the matrix representing the linear operator is $N \times N$, and $N = N_{k_x} \times N_z \times N_{v_{||}} \times N_\mu$) and very large problems are not numerically tractable.

Electrostatic eigenvalue spectra (as discussed in Chap. II) show that subdominant modes with odd parity for ϕ are very weakly damped (small negative growth rates). In the electromagnetic case it was found that the iterative SLEPc solvers fail to converge when pointed at this region of the spectrum. When the iterative solvers are directed to find the modes with the largest growth rates, they converge on all unstable modes and a few weakly damped high-frequency modes that are unrelated to the eigenmodes of interest. Thus, the SCALAPACK direct solvers have been used to examine this problem. These eigenvalue runs use slightly reduced resolution ($N_{v_{||}} = 32$ with five k_x values) and thus may under-resolve some modes. The growth rates and frequencies of the most unstable mode differ slightly from (but are still quite close to) those calculated using a high-resolution initial value calculation as shown in Fig. 5.3 which will be described below. This should be kept in mind when interpreting these results and judging their robustness. Even with this reduced resolution, each solution requires $\sim$ 8000 cpu hours (a doubling of the resolution in any coordinate would increase this by a factor of eight).

The eigenvalue solver is used to solve for the linear eigenmodes over a scan of binormal wavenumbers ranging from $k_y\rho_i = 0.05$ to $k_y\rho_i = 0.7$ (at $k_x = 0$ and $\beta = 0.003$). The mode structures, frequencies, and growth rates of the ten least damped modes at each wavenumber are examined in detail. The modes are characterized by three criteria: 1) stability as determined by positive or negative growth rates, 2) sign of the frequency (i.e., positive indicates a phase velocity in the ion diamagnetic direction and negative indicates a phase velocity in the electron diamagnetic direction), and 3) parity of the parallel mode structures of the fields. Many of the important results are conveyed in Fig. 5.3 where the mode frequencies are plotted in the top panel and the

growth rates are plotted in the bottom panel. Modes with non-tearing parity are plotted with red plus signs (for modes with positive frequencies) and orange $\times$ marks (for modes with negative frequencies), while modes with tearing parity are plotted with blue squares (for modes with positive frequencies) and green triangles (for modes with negative frequencies). Note that the eigenvalues from a high-resolution initial value simulation (black asterisks) are quite close to the values for the most unstable modes calculated by the eigenvalue solver. The instability that dominates at $k_y\rho_i > 0.45$ is likely some manifestation of a CTEM or ETG instability and is largely suppressed as is evident from the low intensity of both ϕ and $A_{||}$ fluctuations at these wavenumbers. At low k_y the tearing parity modes are weakly damped (or in one case at $k_y\rho_i = 0.35$ weakly unstable), and at high k_y some modes become unstable and attain significant positive growth rates. This can be seen more clearly in Fig. 5.4 where the growth rates of the tearing parity modes are plotted on a smaller plot range. Also note that the tearing parity modes with ion diamagnetic frequencies are predominantly stable and clustered at low k_y, while the modes with electron diamagnetic frequencies favor high k_y and become unstable at these scales. This high-k_y region is where magnetic island overlap causes the stochasticity.

The tearing parity modes with ion diamagnetic frequencies have very standard mode structures; the $A_{||}$ (ϕ) mode structure looks very similar to the ϕ ($A_{||}$) mode structure of an unstable mode (see, e.g., Fig. 5.1). In contrast, the ϕ mode structures of the electron diamagnetic tearing-parity modes peak at the outboard midplane, but farther along the field line ($z = \pm 2\pi$ - i.e., the outboard midplane for higher k_x values) and have very little amplitude at $z = 0$ as seen in Fig. 5.5 A. The $A_{||}$ mode structures peak at $z = 0$ but also have extended structure along the field line as seen in Fig. 5.5 B. It is plausible that the stable ion diamagnetic modes are finite-β corrections to electrostatic modes (this is lent credence by the existence of very similar electrostatic

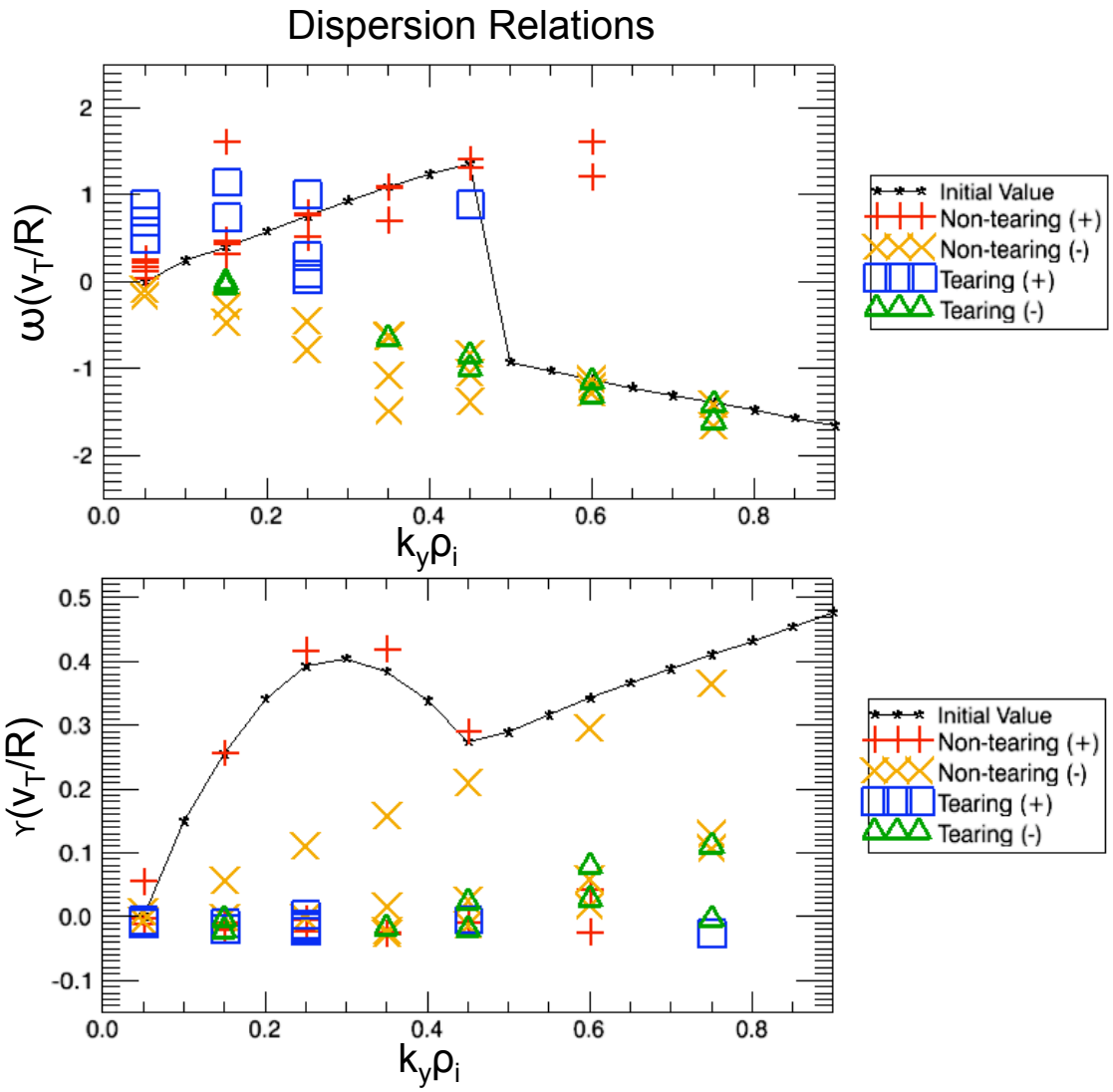

Figure 5.3: Frequencies (top) and growth rates (bottom) of the ten least damped modes for series of k_y values at $k_x = 0$. The modes are characterized as tearing (blue squares and green triangles) or non-tearing (red plus marks and orange x marks) and also characterized by ion diamagnetic frequencies (red plus marks and blue squares) and electron diamagnetic frequencies (orange x marks and green triangles).

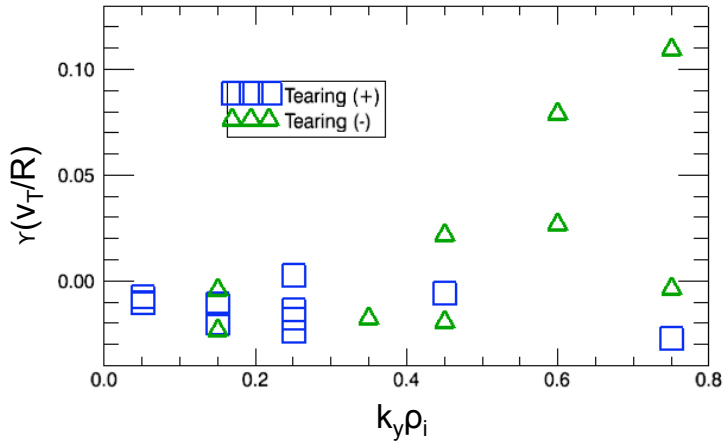

Figure 5.4: Growth rates of the tearing parity modes among the ten least damped modes for series of k_y values at $k_x = 0$. The blue squares denote ion diamagnetic frequencies and the green triangles denote electron diamagnetic frequencies.

modes as discussed in Sec. 3.4). Further study is necessary in order to classify the unstable electron diamagnetic modes.

To summarize, several subdominant linear eigenmodes with tearing parity are part of the eigenmode spectrum. At low k_y these are stable, they have standard mode structures, and positive frequencies. At smaller scales ($k_y\rho_i \gtrsim 0.35$), the modes become unstable, they have more mode structure extended along the field line, and negative frequencies. The next section will address the question of which kinds of modes are excited in the nonlinearly developed turbulence.

5.4 Subdominant Tearing-Parity Modes in the Nonlinear State

POD analysis of $A_{||}$ data from nonlinear simulations reveals that subdominant modes with tearing parity do, in fact, contribute to the fluctuation spectrum. The POD analysis is identical to that described in Sec. 3.4 except that the input data is limited to the fields, ϕ and $A_{||}$, (rather than the entire distribution function). For a selected wavevector, these are functions only of the parallel coordinate, z. Note that

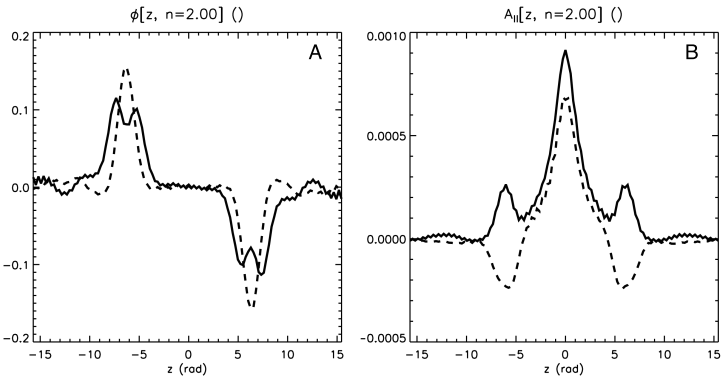

Figure 5.5: Parallel mode structures of the electrostatic potential (A) and the parallel magnetic vector potential (B) for a subdominant, unstable, linear eigenmode with tearing parity and electron diamagnetic frequency for $\beta = 0.003$ and $k_y\rho_i = 0.6, k_x\rho_i = 0$. This mode structure is representative of other tearing parity modes with electron diamagnetic frequencies.

when POD is applied to the ϕ and $A_{||}$ data-sets separately the mode structures for the two fields are not coupled to each other as they would be if POD were applied to the distribution function (in other words an even $n = 1$ ϕ mode structure need not be matched by an odd $n = 1$ $A_{||}$ mode structure). Certain higher k_x wavevectors are connected to the central wavevector through the parallel boundary condition (37), extending the parallel mode structure over several poloidal turns. All such connections are included in this analysis. For $k_x\rho_i = 0, k_y\rho_i \lesssim 0.35$ wavevectors, the $n = 1$ ϕ mode has even parity and the $n = 1$ $A_{||}$ mode has odd parity, as shown in Figs. 5.6 A and C for $k_x\rho_i = 0.2$ and $\beta = 0.003$. In contrast, the $n = 2$ ϕ mode has odd parity and the $n = 2$ $A_{||}$ mode has even (tearing) parity, as shown in Figs. 5.6 B and D. There are also additional subdominant modes with tearing parity and increasingly small scale structure in the parallel coordinate. For the electrostatic potential this situation is maintained as k_y increases. In contrast, for $A_{||}$, beyond $k_y\rho_i = 0.35$ the tearing parity mode becomes the dominant structure and the non-tearing parity mode (even in $A_{||}$) has smaller amplitude. This is shown in Fig. 5.7 where the singular values of the

first two modes are plotted for both the electrostatic potential (A) and the magnetic vector potential (B); at $k_y\rho_i = 0.35$ the two modes have comparable amplitudes and at larger k_y the $n = 1$ mode is characterized by tearing parity. This transition point ($k_y\rho_i = 0.35$) also marks the point beyond which the negative frequency tearing-parity modes become unstable. Note that the $A_{||}$ fluctuations (tearing and non-tearing) are smaller at high k_y than low k_y in spite of linear instability demonstrated in the previous section at high k_y. In addition, the $A_{||}$ mode structures at high k_y are more similar to the structures at low k_y (e.g. those seen in Fig. 5.6) than the mode structure of the unstable electron diamagnetic frequency modes like the one shown in Fig. 5.5. As expected, for $k_x > 0$ wavevectors, the $n = 1$ POD modes deviate from the exact parity exhibited in Fig. 5.6.

The situation described in Fig. 5.7 is replicated to a very close degree throughout the β-scan. This is shown in Fig. 5.8 for $\beta = 0.008$ where it is seen that many of the features at $\beta = 0.003$ are reproduced: the k-dependence, relative amplitudes of the two modes, and the k_y position of the switch in $A_{||}$ mode amplitudes are very close to what is observed at $\beta = 0.003$. The major difference is the amplitude of the $A_{||}$ fluctuations (both tearing and non-tearing) which, as would be expected, increases with β. These observations hold for a series of analyses ranging from $\beta = 0.001$ to $\beta = 0.01$.

While this POD analysis demonstrates the presence of modes with tearing parity in the nonlinearly developed turbulence, it does not define exactly how these modes are related to the linear eigenmodes discussed in the previous section. One easy comparison is between the mode structures of the POD modes with the linear eigenmodes. Figure 5.9 A shows the ϕ mode structure of the most unstable eigenmode (black) and the $n = 1$ POD mode (red) and demonstrates that there is little, if any, discernible difference between the two (this is for $k_y = 0.15$, $\beta = 0.003$). The $A_{||}$ mode structures

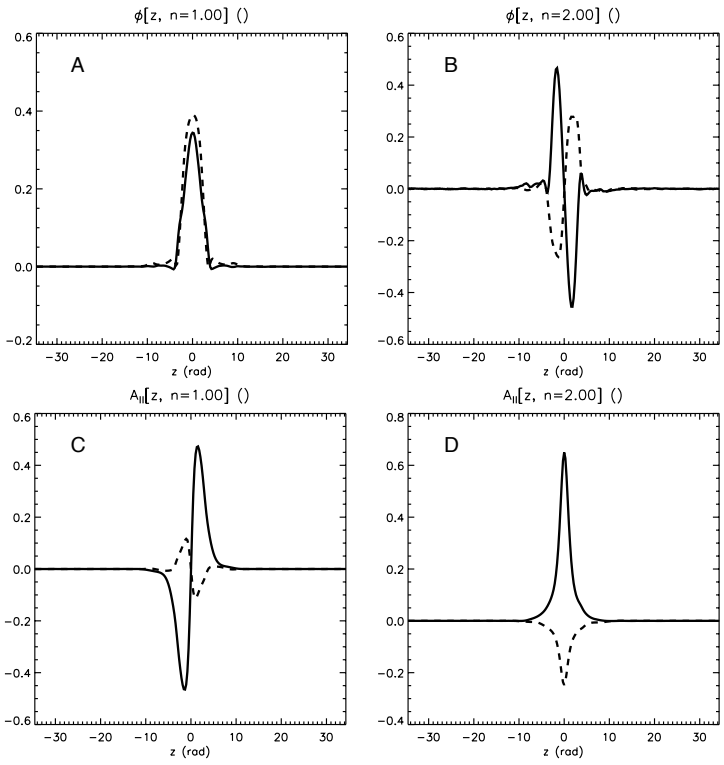

Figure 5.6: Plot of the POD parallel mode structures of the electrostatic potential for the $n = 1$ mode (A), and $n = 2$ mode (B). Plot of the magnetic vector potential of the $n = 1$ mode (C) and the $n = 2$ mode (D). For the magnetic vector potential the $n = 1$ mode has odd parity and so is not resonant, whereas the $n = 2$ mode has even parity and is resonant. This is for $k_x\rho_i = 0.0, k_y\rho_i = 0.2$.

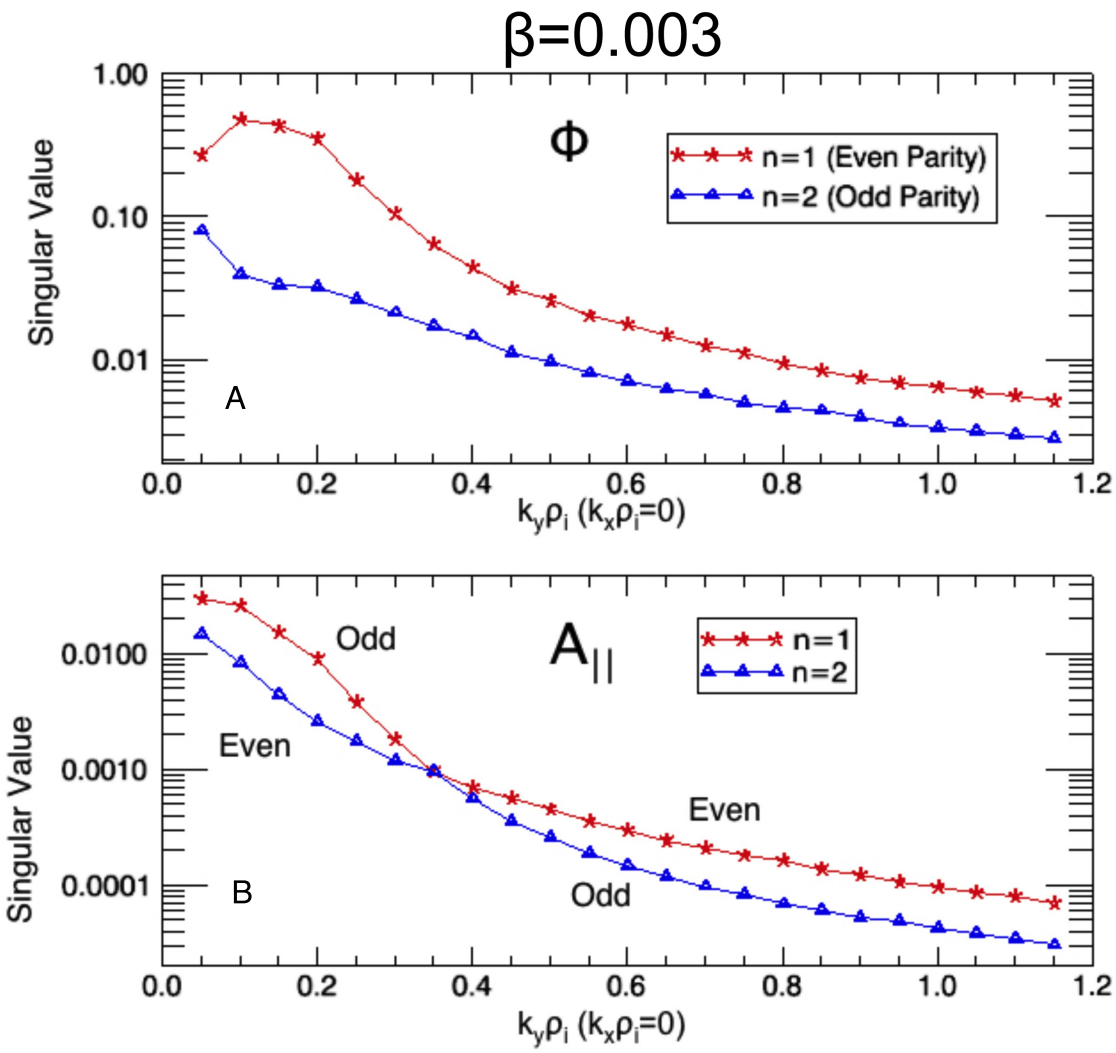

Figure 5.7: Plot of the singular values of the $n = 1$ POD mode (red asterisks) and the $n = 2$ POD mode (blue triangles) for the electrostatic potential (top) and the magnetic vector potential (bottom) as a function of k_y at $k_x = 0.0$ for $\beta = 0.003$. For the magnetic vector potential the $n = 1$ mode is the odd (non-tearing) mode at $k_y\rho_i < 0.35$ and the even (tearing parity) mode for $k_y\rho_i > 0.35$.

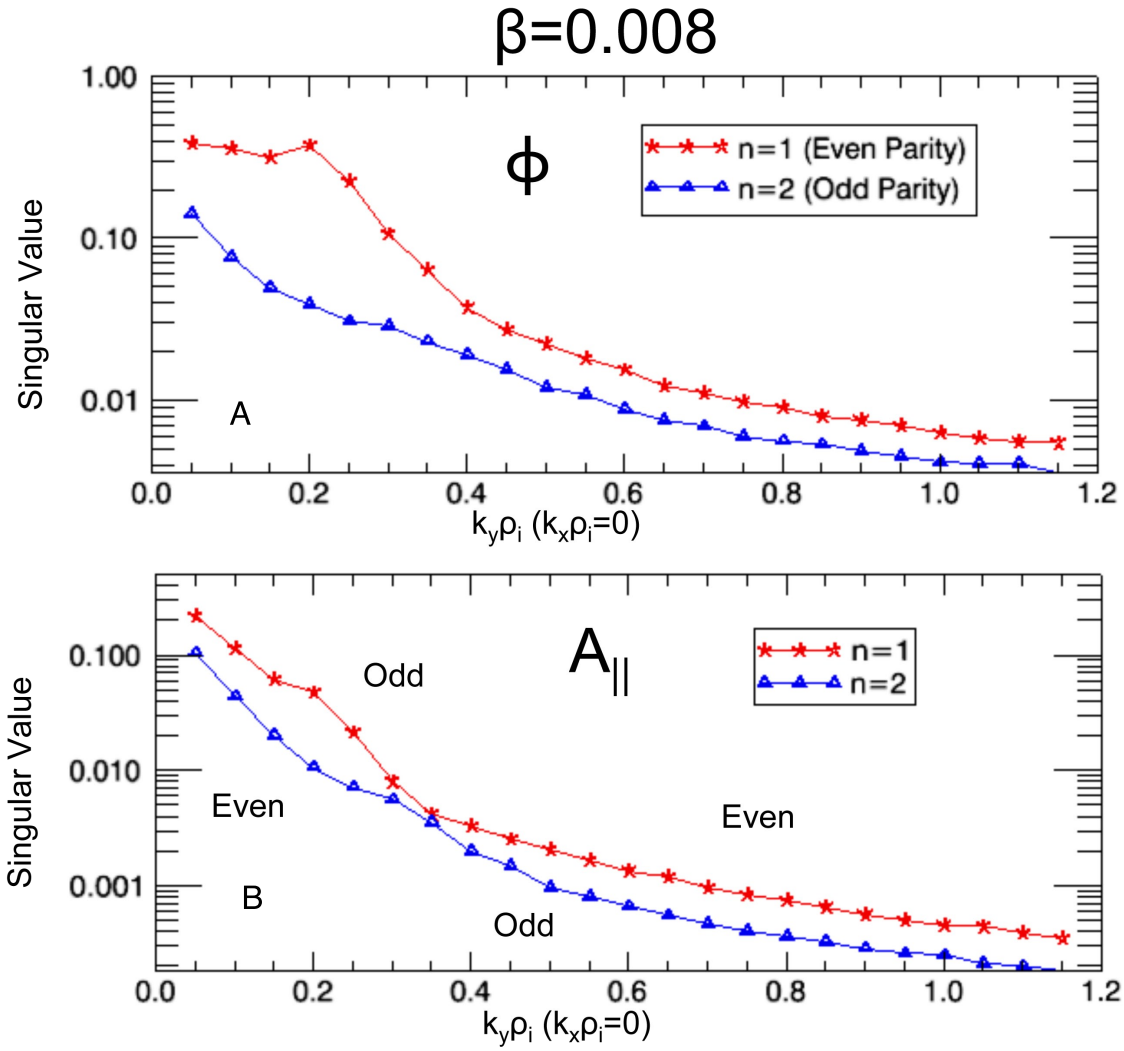

Figure 5.8: Plot of the singular values of the $n = 1$ mode (red asterisks) and the $n = 2$ mode (blue triangles) for the electrostatic potential (top) and the magnetic vector potential (bottom) as a function of k_y at $k_x = 0.0$ for $\beta = 0.008$. For the magnetic vector potential the $n = 1$ mode is the odd (non-tearing) mode at $k_y\rho_i < 0.35$ and the even (tearing parity) mode for $k_y\rho_i > 0.35$. A comparison with Figure 5.7 illustrates the β dependence: as β increases, the mode amplitudes maintain a similar ratio but the magnitude of the $A_{||}$ intensity increases.

for a tearing-parity mode have much in common (identical shape near the outboard midplane) but also exhibit noticeable differences (broader base for the POD mode) as is seen in Fig. 5.9 B. A linear eigenmode decomposition would be necessary in order to define the exact contribution of each mode to the nonlinear state, but for the purposes of this study such a distinction is not critical. It is clear that the POD analysis selects a dominant mode which is very similar to the unstable eigenmode and plays the same role as the energy drive. In addition, subdominant POD modes have many features in common with subdominant linear eigenmodes. There may not be a one to one correspondence between subdominant POD modes and subdominant linear eigenmodes, but the subdominant POD modes capture the same physical effects as the subdominant linear eigenmodes with similar structures.

5.5 Subdominant Modes and Magnetic Stochasticity

POD mode decompositions can be used to determine the contributions of different structures to magnetic stochasticity. A POD of $A_{||}$ data is constructed for every independent set of wavevectors (central k_x plus high k_x connections) in a $\beta = 0.003$ nonlinear simulation. The first two POD modes are generally similar to those shown in Figs. 5.6 for $k_x = 0$ wavevectors. For $k_x > 0$ wavevectors, the first two POD modes still typically exhibit predominantly even or odd parity with some (typically rather small) degree of deviation. An algorithm is used to select from the first two POD modes those which have predominantly tearing parity and those which are predominantly odd parity. This algorithm calculates a parity factor, $P = \frac{\sqrt{|\int A_{||}(z)dz|^2}}{\sqrt{\int |A_{||}(z)|^2 dz}}$, for each of the first two POD modes. Whichever of the first two modes has the larger parity factor is grouped in a 'tearing parity group' and the other mode is grouped in a 'non-tearing parity group'. Note that this grouping does not guarantee that

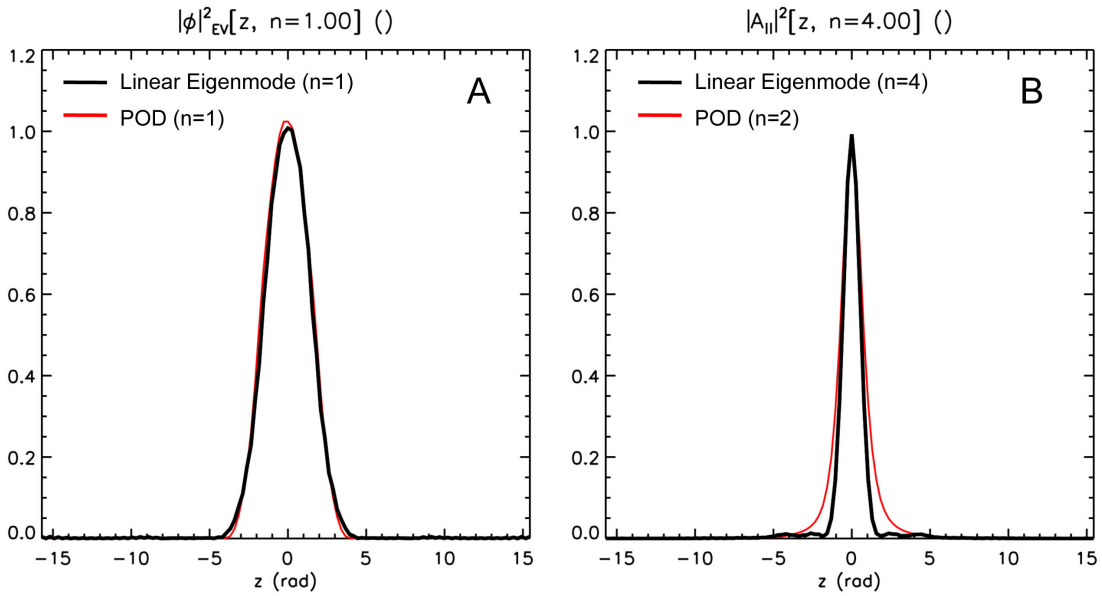

Figure 5.9: Comparisons of the squared parallel mode structures for POD modes and linear eigenmodes. Figure A shows the electrostatic potential parallel mode structures for the $n = 1$ POD mode (red) and most unstable linear eigenmode (black) for $k_y\rho_i = 0.15, k_x\rho_i = 0$ and $\beta = 0.003$, demonstrating that the mode structures are virtually identical. Figure B shows the parallel magnetic vector potential mode structures for the $n = 2$ POD mode (red) and least damped linear eigenmode with tearing parity (black) for $k_y\rho_i = 0.15, k_x\rho_i = 0$ and $\beta = 0.003$. The $A_{||}$ mode structures are very similar but not identical.

the tearing parity group will be the dominant contributor to magnetic stochasticity; the non-tearing parity group contains $|k_x| > 0$ modes that have some component of tearing parity as well. If these modes are achieve high enough amplitude (relative to the tearing parity modes), their resonant components could be the dominant cause of the stochasticity. This grouping produces a decomposition of the total $A_{||}$ (including all wavevectors)

$$A^{(total)}_{||_{k_x,k_y}}(z,t) = A^{(1)}_{||_{k_x,k_y}} + A^{(2)}_{||_{k_x,k_y}} + A^{(res)}_{||_{k_x,k_y}}, \tag{5.4}$$

where $A^{(1)}_{||_{k_x,k_y}}$ is the group of predominantly odd modes, $A^{(2)}_{||_{k_x,k_y}}$ is the group of predominantly even modes, and $A^{(res)}_{||_{k_x,k_y}}$ consists of all $n > 2$ modes in the decomposition. The contribution of each of these groups to the structure of the magnetic field can then be considered.

A routine (78) is used to follow the perturbed magnetic field over several poloidal cycles for each term in Eq. (5.4). A measure of the impact of each group to the perturbed magnetic field can be quantified by calculating a magnetic diffusion coefficient (79), $D_{fl} = \lim_{l\to\infty} \dfrac{\langle [r_i(l) - r_i(0)]^2 \rangle}{2l}$. To illustrate this, Fig. 5.10 shows D_{fl} for 100 field lines (evenly distributed in the radial direction) as calculated over several poloidal cycles for $A^{(total)}_{||}$ at $t(v_T/R) = 98$. Fig. 5.11 shows D_{fl} averaged over 500 poloidal cycles (black) and the after the final poloidal cycle (red) for $A^{(total)}_{||}$ for a series of time steps (averaged over all field lines). These calculations are performed for all the terms in Eq. 5.4. The results are shown in Fig. 5.12 where the final value of D_{fl} is plotted for a series of time steps for each term. The predominantly odd modes produce a diffusion coefficient that is an order of magnitude smaller than the other contributions. The tearing parity modes produce magnetic diffusion coefficients that are comparable in amplitude to the total. This is surpassed, to a degree, by the resid-

ual ($n > 2$) modes, which are defined by finer scale structure in the parallel direction, and include many modes with tearing parity. This indicates that a large number of modes, which represent a variety of scales and structures in phase space $(z, v_{||}, \mu)$, contribute in a significant way to the structure of the magnetic field. This is similar to the results on energy dissipation discussed in Sec. 4.2 where it was noted that a large number of modes contribute to the energy dissipation.

5.6 Summary

In summary, it has been shown that the linear gyrokinetic equation at $k_x = 0$ allows for linear eigenmodes with $A_{||}$ mode structures which are either even (tearing) or odd (non-tearing) about the outboard midplane. The most unstable modes are characterized by non-tearing parity. At $|k_x| > 0$, this parity restriction is broken, and the most unstable modes may possess a slight resonant component. Linear analysis reveals subdominant modes with tearing parity at $k_x = 0$. At low k_y these modes are weakly damped and have frequencies in the ion-diamagnetic direction. At higher k_y an unstable mode with tearing parity and an electron diamagnetic frequency appears. POD analysis reveals the excitation of modes with even $A_{||}$ structures in the nonlinear fluctuations. Below $k_y\rho_i = 0.35$ such modes are the second most important structures in the $A_{||}$ fluctuations, whereas above $k_y\rho_i = 0.35$ the tearing parity mode is dominant. Analysis of the resulting magnetic fields associated with different groupings of POD modes demonstrates that the primarily non-tearing parity modes produce a relatively small degree of magnetic diffusivity. The largest tearing parity modes produce a substantial degree of magnetic diffusivity. This is surpassed by the amount of magnetic diffusivity produced by the residual ($n > 2$) modes demonstrating that a large number of damped modes provide a significant contribution to the magnetic

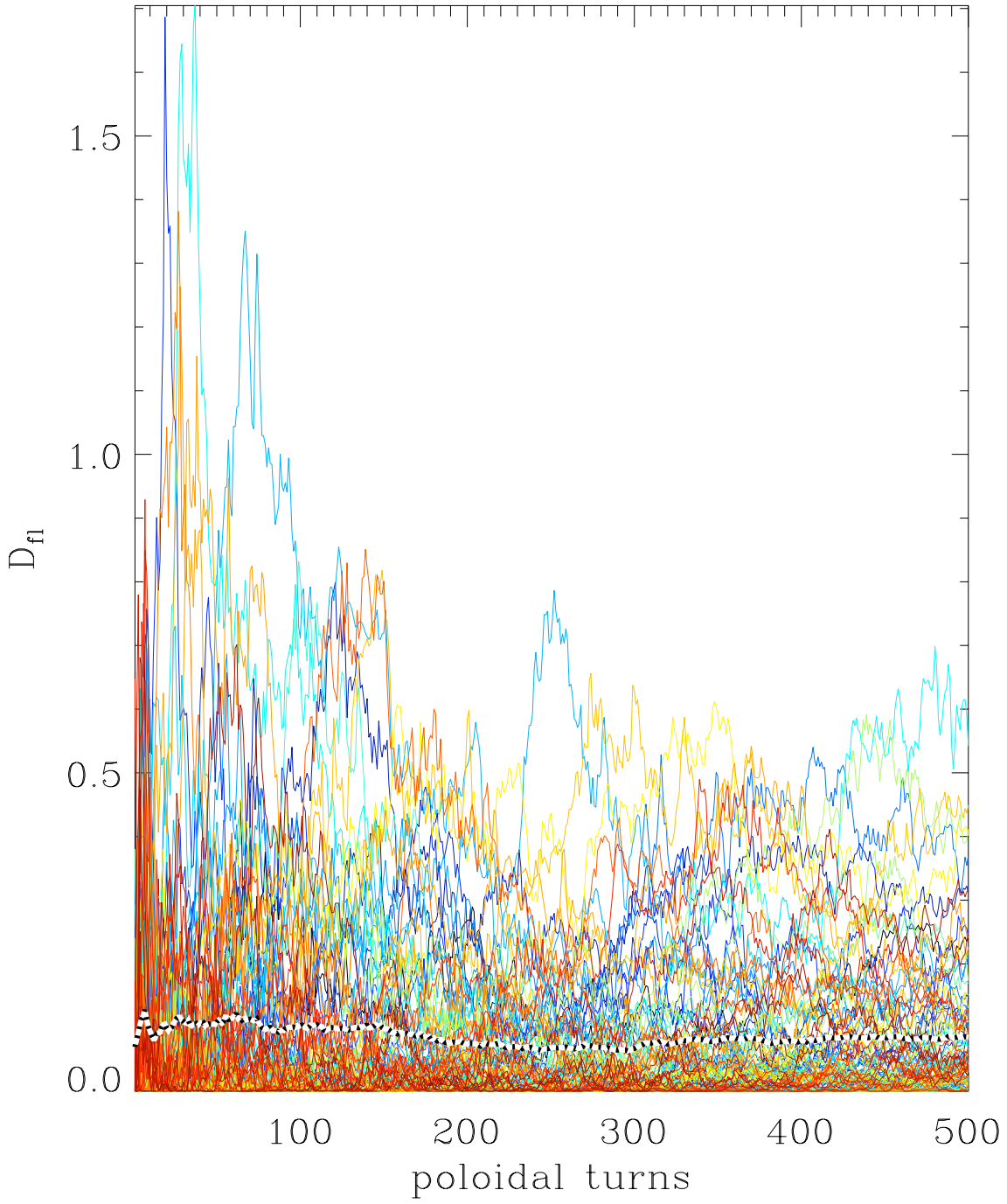

Figure 5.10: Plot of the magnetic diffusivity at $t(v_T/R) = 98$ for each of 100 field lines as a function of number of poloidal turns. The dashed line near the bottom of the plot denotes the average of the field lines.

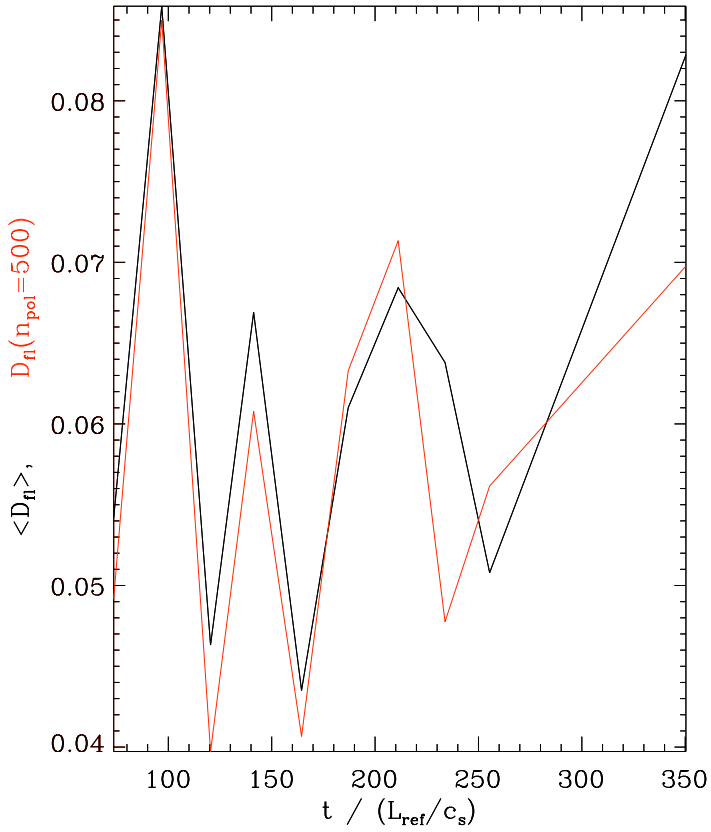

Figure 5.11: Plot of the magnetic diffusivity averaged over 100 field lines for a series of time steps. The black line denotes the average over all 500 poloidal turns and the red line denotes the final value (after turn 500).

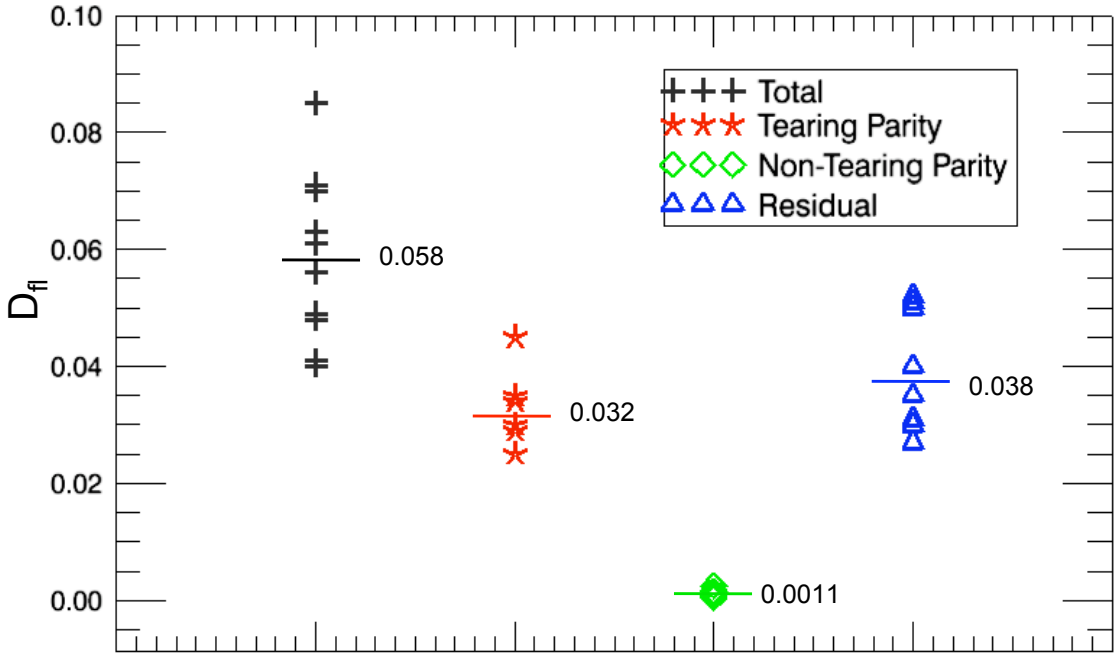

Figure 5.12: Plot of the magnetic diffusivities for a series of time steps for the terms in Eq. 5.4: total $A_{||}$ (black plus marks), the grouping of those of the top two POD modes with predominantly tearing parity (red asterisks), the grouping of those of the top two POD modes with predominantly non-tearing parity (green diamonds), and the grouping of all other ($n > 2$) POD modes (blue triangles). Averages are shown with horizontal lines

fluctuations.

CHAPTER VI

Higher Order Singular Value Decomposition

6.1 Introduction

Thus far in this thesis, the matrix decomposition, SVD, has been applied to several different problems. In this section I discuss applications of higher-order singular value decomposition (HOSVD) - a *tensor* decomposition. This is a variant of SVD that is well suited to analyzing high-dimensional data.

A matrix decomposition, like a matrix, is inherently two dimensional. The matrix decomposition, SVD, can be applied to higher dimensions by matricizing the data (unstacking it to two dimensions), as is described in Sec. 3.4. In Sec. 3.4 SVD is applied to selected wavevectors of the gyrokinetic distribution function from nonlinear simulations. Even for these reduced data sets (single wavevector), it is necessary to matricize the data (reducing the $(z, v_{||}, \mu)$ dependence to a vector) in order to perform a SVD. In this section HOSVD is used to analyze the *entire* gyrokinetic distribution function from a simulation - a very large, high-dimensional object.

Gyrokinetic simulations produce a very large amount of information, but only a small fraction of this is typically analyzed, or even output to a file. An extreme

Symbol	Name	Description
$M_{ijk(...)}$	Data tensor	Tensor containing data set of interest.
$i, (j, k, ...)$	1-coordinate index	Index which varies over the first coordinate of the data tensor.
$C^{(1)}_{pq}, (C^{(2)}_{pq}...)$	1-coordinate correlation matrix	
$u^{(m_1)}_i, (v^{(m_2)}_j...)$	1-modes	The eigenvectors of the 1-coordinate correlation matrix.
$\sigma^{(1)^2}_{m_1}, (\sigma^{(2)^2}_{m_2}, ...)$	1-coordinate eigenvalues	Eigenvalues of the 1-coordinate correlation matrix.
$S_{m_1 m_2 m_3(...)}$	Core tensor	Tensor defining weights of the the tensor products in a HOSVD.
$m_1, (m_2, m_3, ...)$	1-mode index	Index which varies over the 1-modes.
$\delta^{(r)}_{HOSVD} = \frac{Drn+r^D}{n^D}$	HOSVD inverse compression ratio	Ratio of data elements in a a decomposition to total data. (when $r = r_1 = r_2 = ...$)
$\delta^{(r_{SVD})}_{SVD} = \frac{r_{SVD}(1+2n^{D/2})}{n^D}$	SVD inverse compression ratio	Ratio of data stored in a a decomposition to total data.
$\| \mathcal{A}\|_F = \sum_{i,j,k...} A^2_{ijk...}$	Squared Frobenius norm	Sum of the squares of all elements in a tensor
$\epsilon^{(r)} = \|\mathcal{A} - \mathcal{A}^{(r)}\|_F$	Truncation error	Measure of fraction of 'energy' lost in a truncation

Table 6.1: Table defining notation and naming conventions used in this paper. In sections where the coordinates are named, '1-coordinate' will be replaced by the name of the coordinate: e.g., '1-coordinate correlation matrix' becomes 'radial correlation matrix', and '1-mode' becomes 'radial mode'.

example of this is when the only information considered is a set of diffusivities. Often, data output is limited to a few moments of the distribution function (consisting of the three spatial dimensions and time). Relatively little has been done to characterize velocity space dynamics (for exceptions see Refs. (49), (64), and (80)), in part because of the high-dimensional, memory-intensive nature of the task. Thus, a technique that can compress large data-sets and facilitate their analysis could be very valuable. In this section HOSVD is used to construct tensor decompositions of such data sets in an attempt to characterize the full distribution function and gain insight into the turbulence it describes. Another, very practical, application is in data compression.

HOSVD was first developed and applied in the field of psychometrics (81). Its use has been much more limited than SVD, particularly with regard to analysis of turbulent systems. Nonetheless it has found a variety of applications in such fields as chemometrics, econometrics, image processing, and biomedical signal processing (for specific examples see references (84) and (82) and references therein). Recently HOSVD has also been used to compress aerodynamic databases (85). Here HOSVD is applied to analysis of the full five-dimensional (plus time) gyrocenter distribution function from gyrokinetic simulations.

Three measures of merit are used to compare the utility of HOSVD against that of the more standard SVD: 1). What degree of computer resources are necessary to use the decomposition (or alternatively, how large of a dataset can be realistically analyzed)? 2). How effectively does the decomposition compress the data set of interest? And 3). how useful is the decomposition in providing insight and facilitating a physical understanding of the data-set. It is found that SVD is superior with regard to the first criterion (although this is probably due only to the exhaustive optimization of SVD routines motivated by its widespread use), HOSVD is superior for criterion two, and with regard to the third criterion, both techniques have certain advantages

depending on the application. These measures of merit will be discussed throughout this chapter and summarized in the conclusion.

This chapter will proceed as follows: in Sec. 6.2, the mathematics of the HOSVD will be outlined. I will discuss in what sense HOSVD is a natural extension of SVD, define notation and naming conventions, and explain the procedure for constructing a HOSVD. In Sec. 6.3, numerical optimization and implementation of an efficient, scalable HOSVD routine is discussed. In Sec. 6.4 I introduce the data sets that are used. In Sec. 6.5, the HOSVD of the full distribution function data-set is used to analyze and understand the underlying turbulence. In Sec. 6.6, a series of truncated HOSVDs are performed on the full gyrokinetic distribution function and numerical performance, compression and truncation are discussed. In Sec. 6.7, results regarding compression and performance of HOSVD and SVD are presented. In Sec. 6.8, I will summarize results and discuss advantages and disadvantages of HOSVD and SVD.

6.2 Mathematics of HOSVD

In this section some of the mathematical basics of the SVD will be reviewed, followed by a mathematical description of the HOSVD. As mentioned above, the HOSVD is a higher-dimensional variant of the SVD. In this section I will draw some analogies between the two. There exists a much more fundamental and rigorous connection between the two decompositions which is described in Ref. (84).

The SVD decomposition of a matrix $M \in \mathbb{C}^{n_1 \times n_2}$ is

$$M = USV^{*T}, \tag{6.1}$$

where $U \in \mathbb{C}^{n_1 \times min(n_1,n_2)}$ and $V \in \mathbb{C}^{min(n_1,n_2) \times n_2}$ are unitary matrices and $S \in \mathbb{C}^{min(n_1,n_2) \times min(n_1,n_2)}$ is a positive definite diagonal matrix (the superscript $*T$ de-

notes a conjugate transpose). The columns of U are called left singular vectors, the columns of V are called right singular vectors, and the non-zero elements of S are called singular values. The singular values are positive and ordered in terms of magnitude.

The construction of the SVD of a matrix M is straightforward. The left singular vectors are the normalized eigenvectors of the correlation matrix MM^{*T}, and the right singular vectors are the normalized eigenvectors of the correlation matrix $M^{*T}M$. The square roots of the first $min(n_1, n_2)$ eigenvalues of either correlation matrix are the singular values.

An alternative notation for the SVD is,

$$M_{ij} = \sum_{l=1}^{min(n_1,n_2)} s_l u_i^{(l)} v_j^{(l)}, \tag{6.2}$$

where $u_i^{(l)}$ ($v_j^{(l)}$) are the left (right) singular vectors (the subscript labels the coordinate and the superscript labels the vector number), and the s_l are the singular values. This notation facilitates understanding of important properties of the SVD and will also be used in describing the HOSVD. This notation reveals the SVD to be a superposition of matrices defined by outer products between the left and right singular vectors. Since the singular vectors are normalized, all amplitude information is contained in the singular values, i.e., the matrices in the series are weighted according to the amplitude of their corresponding singular values. One important property of the SVD is 'optimality': a truncated decomposition, $M_{ij}^{(r)} = \sum_{l=1}^{r<min(n_1,n_2)} s_l u_i^{(l)} v_j^{(l)}$, (a decomposition keeping a reduced number $r < min(n_1, n_2)$ of outer products in the series) is guaranteed to reproduce the original matrix better than any other decomposition of

the same rank r. Formally this is described as

$$\epsilon^{(r)} = ||M - M_{SVD}^{(r)}||_F \leq ||M - \sum_{l=1}^{r} \vec{x_l} \otimes \vec{y_l}||_F \text{ for all } \vec{x_l} \in \mathbb{C}^{n_1}, \text{ and } \vec{y_l} \in \mathbb{C}^{n_2}, \quad (6.3)$$

where $||A||_F = \sum_{i,j} A_{ij}^2$ denotes the square of the Frobenius norm (note that the square root is omitted in order to give more meaning to the norm; squared physical quantities are often associated with energy-like quantities). The magnitude (as defined by the square of the Frobenius norm) of a matrix is equal to the sum of its singular values squared. Also, it can be shown that the truncation error is equal to the sum of the squares of the singular values corresponding to all truncated modes: $\epsilon^{(r)} = \sum_{l=r+1}^{min(n_1,n_2)} s_l^2$.

Now consider a three dimensional tensor, $M \in \mathbb{C}^{n_1 \times n_2 \times n_3}$ (in the discussion that follows, three dimensions will be used for simplicity of notation; it is a straightforward exercise to extend these results to higher dimensions). An appealing extension of the SVD decomposition to higher order tensors is to decompose an N-dimensional tensor as a series of outer products between N vectors with each term in the series weighted by a singular value,

$$M_{ijk} = \sum_{l=1}^{min(n_1,n_2,n_3)} s_l u_i^{(l)} v_j^{(l)} w_k^{(l)}. \quad (6.4)$$

Such a decomposition cannot, in general, be constructed (if such a decomposition were possible in general, the resulting compression would be enormous!). If one uses a generalized notion of a singular value, replacing a series of singular values with a tensor $S_{m_1 m_2 m_3}$, a feasible decomposition can be defined. The HOSVD is based on a decomposition of this form:

$$M_{ijk} = \sum_{m_1=1}^{n_1} \sum_{m_2=1}^{n_2} \sum_{m_3=1}^{n_3} S_{m_1 m_2 m_3} u_i^{(m_1)} v_j^{(m_2)} w_k^{(m_3)} \quad (6.5)$$

In this expression, the data tensor, M_{ijk}, is reproduced as a superposition of tensors - outer products between sets of modes defined independently for each coordinate. In this work the modes, $u_i^{m_1}$ ($v_j^{m_2}$ . . .) will be called one-modes (two-modes, . . .), or when the coordinates are explicitly named they will be identified with the name of the coordinate (e.g., radial modes or x-modes). The tensor $S_{m_1 m_2 m_3}$ will be called the core tensor. These conventions, along with other notation and naming conventions, are summarized in table 6.1.

The modes, $u_i^{m_1}$, in a HOSVD are calculated in a way that is similar to the process for calculating singular vectors of a SVD. Correlation matrices can be defined for each coordinate:

$$C_{pq}^{(1)} = \sum_{j=1}^{n_2} \sum_{k=1}^{n_3} M_{pjk}^* M_{qjk}, \tag{6.6}$$

for coordinate one, and,

$$C_{pq}^{(2)} = \sum_{i=1}^{n_1} \sum_{k=1}^{n_3} M_{ipk}^* M_{iqk}, \tag{6.7}$$

for coordinate two, etc. The eigenvectors of these correlation matrices are chosen to be the coordinate modes:

$$\sum_{q=1}^{n_1} C_{pq}^{(1)} u_q^{(m_1)} = \sigma_{m_1}^{(1)^2} u_p^{(m_1)}, \tag{6.8}$$

$$\sum_{q=1}^{n_2} C_{pq}^{(2)} v_q^{(m_2)} = \sigma_{m_2}^{(2)^2} v_p^{(m_2)}, \tag{6.9}$$

and so on. Note that the correlation matrices are Hermitian by construction and so the eigenvectors are orthogonal. For SVD the eigenvalues of the correlation matrices are directly related to the singular values. In contrast, the eigenvalues of the HOSVD correlation matrices, $\sigma_{m_1}^{(1)^2}$, are not directly related to the core tensor S_{ijk} (however, they do provide an error bound as will be described below). Rather, the orthogonality

of the coordinate modes can be exploited to solve for the core tensor:

$$S_{m_1 m_2 m_3} = \sum_{i=1}^{n_1} \sum_{j=1}^{n_2} \sum_{k=1}^{n_3} M_{ijk} u_i^{*(m_1)} v_j^{*(m_2)} w_k^{*(m_3)}. \tag{6.10}$$

This operator is often called the Tucker operator (82) and will be called by that name in this chapter. This defines a method for determining the elements of the core tensor and thus producing a decomposition of the form of Eq. 6.5.

Multiple truncation ranks are necessary to define a truncated HOSVD,

$$M_{ijk}^{(r_1 r_2 r_3)} = \sum_{m_1=1}^{r_1} \sum_{m_2=1}^{r_2} \sum_{m_3=1}^{r_3} S_{m_1 m_2 m_3} u_i^{(m_1)} v_j^{(m_2)} w_k^{(m_3)}, \tag{6.11}$$

where $r_1(r_2...)$ is the number of 1(2...)-modes kept in the decomposition. In analogy to SVD, the magnitude of the data tensor is equal to the sum of the squares of the elements of the core tensor: $\sum_{i=1}^{n_1} \sum_{j=1}^{n_2} \sum_{k=1}^{n_3} M_{ijk}^2 = \sum_{m_1=1}^{n_1} \sum_{m_2=1}^{n_2} \sum_{m_3=1}^{n_3} S_{m_1 m_2 m_3}^2$. Also, the truncation error is equal to the sum of the squares of the $m_n > r_n$ elements of the core tensor,

$$\epsilon_{HOSVD}^{(r_1 r_2 r_3)} = ||M_{ijk} - M_{ijk}^{(r_1 r_2 r_3)}||_F = \sum_{m_1=r_1+1}^{n_1} \sum_{m_2=r_2+1}^{n_2} \sum_{m_3=r_3+1}^{n_3} S_{m_1 m_2 m_3}^2. \tag{6.12}$$

It can be shown that the eigenvalues of the correlation matrices can be used to determine an error bound for a given set of truncation ranks:

$$\epsilon_{\text{Bound}}^{(r_1 r_2 r_3)} = \sum_{m_1=r_1+1}^{n_1} \sigma_{m_2}^{(2)^2} + \sum_{m_2=r_2+1}^{n_2} \sigma_{m_2}^{(2)^2} + \sum_{m_3=r_3+1}^{n_3} \sigma_{m_3}^{(3)^2} \geq \epsilon_{HOSVD}^{(r_1 r_2 r_3)} \tag{6.13}$$

This is a very useful property of the HOSVD. The most computationally expensive step in calculating the decomposition is the calculation of the core tensor (depending on the truncation ranks). This error bound allows one to determine a sufficient set

of truncation ranks for a specified error tolerance after solving the correlation matrix eigenproblems but before calculating the core tensor.

One drawback of the HOSVD is that there is no analogue to the SVD optimality theorem; one must perform the calculation in order to see if it has good properties in terms of compression or extracting important features. However, the error bound in Eq. 6.13 gives an indication why the HOSVD can be useful for these purposes; if the magnitudes of the coordinate eigenvalues decrease rapidly (as is often the case) then the truncation error is ensured to be correspondingly small.

6.3 Numerical Optimization and Implementation

Two challenges are presented in producing a numerical implementation of the HOSVD algorithm. First, due to its high-dimensional nature, the important operations in the HOSVD are tensor operations. Unfortunately, nearly all optimized numerical libraries cater to matrix operations rather than tensor operations. Second, the data-sets of interest are very large, so memory constraints quickly become an issue. The solution to the first problem is to 'matricize' the tensors and tensor operations, and the solution to the second problem is to parallelize the algorithm.

Recall from the previous section that there are three steps in calculating a HOSVD:

1). Calculation of the correlation matrices. For a D-dimensional tensor with $n = n_1 = ...$, this requires $\mathcal{O}(n^{D+1})$ operations.

2). Calculation of the eigenvectors and eigenvalues of the correlation matrices. Since each correlation matrix is only $n \times n$ (compared to the entire n^D tensor) this is a very inexpensive calculation; if the problem as a whole is tractable then this step is trivial.

3). Extraction of the core tensor. For the entire decomposition this scales as

$\mathcal{O}(n^{2D})$ (for every value of the core tensor (n^D), one must cycle through every element of the data-tensor as seen in Eq. 6.5). As such, optimization of this step is critical to producing an efficient implementation of the HOSVD algorithm.

The optimization strategy that has been used here is to formally map the data-tensor onto a 2-D matrix and then convert the tensor version of the Tucker operator into a matrix operator. At this point, standard optimized numerical libraries can be exploited to efficiently calculate the core tensor. The important steps are outlined in Refs. (83),(82). First the data-matrix must be matricized - mapped from a D-dimensional tensor onto a 2-dimensional matrix. Then the Tucker operator must be converted into a matrix operator. For a 6-D tensor (like those analyzed in this chapter) the tensor version of the Tucker operation is,

$$S_{m_1 m_2 m_3 m_4 m_5 m_6} = \sum_{i=1}^{n_1}\sum_{j=1}^{n_2}\sum_{k=1}^{n_3}\sum_{l=1}^{n_4}\sum_{m=1}^{n_5}\sum_{n=1}^{n_6} M_{ijklmn} u_i^{*(m_1)} v_j^{*(m_2)} w_k^{*(m_3)} x_l^{*(m_4)} y_m^{*(m_5)} z_n^{*(m_6)}. \tag{6.14}$$

The matricized version of this operation is,

$$S^{(6\to 2)} = (U \otimes V \otimes W) M^{(6\to 2)} (Z \otimes Y \otimes X)^T. \tag{6.15}$$

In this equation the notation $S^{(6\to 2)}$ is used to denote the remapping of a 6-D tensor to a 2-D matrix, and U, V (etc.) are the matrices containing the coordinate modes. The symbol $\otimes$ denotes the Kronecker product,

$$A \otimes B = \begin{pmatrix} a_{11}B & \cdots & a_{1a_2}B \\ \vdots & \ddots & \vdots \\ a_{a_1 1} & \cdots & a_{a_1 a_2}B \end{pmatrix}. \tag{6.16}$$

In this construction, the first three coordinates of M_{ijklmn} are mapped to the rows of

the matrix (so that U, V, and W are on the left side of the matrix multiplication) and the other three coordinates are mapped to the columns (so that Z, Y, and X are on the right side of the matrix multiplication). Note that the tensor version of the operation requires $\mathcal{O}(n^{12})$ operations, whereas the matrix version requires only $\mathcal{O}(n^9)$ operations, (two matrix multiplications of $n^3 \times n^3$ matrices). This corresponds to $\mathcal{O}(n^{2D})$ and $\mathcal{O}(n^{3D/2})$ for D-dimensions for the tensor and matrix versions, respectively. Thus the matrix version of the operation is not only suitable for optimized numerical linear algebra libraries, but also requires significantly fewer operations. For a small test problem, matricizing the HOSVD operator reduced computation time from ~ 25 minutes to ~ 5 seconds - a reduction by a factor of ~ 300.

As with the matricized HOSVD, the full SVD of a D-dimensional tensor also requires $\mathcal{O}(n^{3D/2})$ operations. Even so, trials indicate that a serial version of the HOSVD code used in this analysis is significantly slower than the LAPACK (87) SVD routine CGESVD. The HOSVD routine took ~ 34 seconds to perform a full HOSVD on a 13 MB, 5-dimensional, test data-set, and the SVD routine took ~ 12 seconds. The LAPACK SVD routine has been extensively optimized over several decades and also specifically tuned to the machine. In light of this fact, it is plausible that if an HOSVD routine were optimized to the same level, it may be competitive with SVD with regard to this performance measure.

In order to deal with large data-sets, parallelization is also necessary. The the PBLAS (77) matrix multiplication routine, PCGEMM, was used for the matrix multiplications in the matricized Tucker operator. A parallel routine for calculating the correlation matrices was written from scratch using MPI. Parallel scaling tests indicate that the code scales as expected with problem size; for a 6-dimensional test tensor (with equal length of n in each dimension), calculation of the full core tensor scales as n^9, and calculation of the correlation matrices scales as n^7 as is shown in

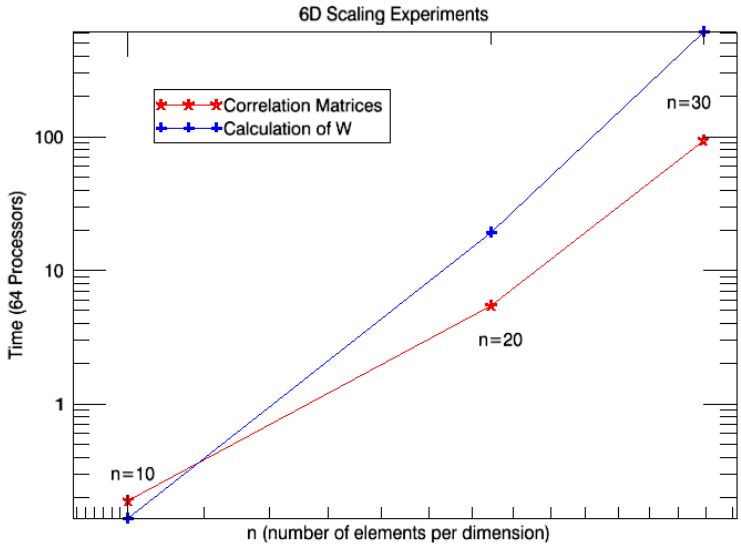

Figure 6.1: Computation time for calculating the full HOSVD of a set of 6-D test data-sets. The time to calculate the correlation matrices (red asterisks) scales like n^7 where n is the number of data elements in each dimension, and the time to calculate the core tensor scales like n^9.

Fig. 6.1. The matrix multiplication step took $\sim$ 10 cpu hours (600 seconds on 64 processors) for the largest data-set in this scan (6-D with $n = 30$ in each dimension which would correspond to 5.8 GB of single precision binary data). The calculation of the correlation matrices is comparatively slow - depending on truncation ranks, it often takes more time than the calculation of the core tensor. Efforts to optimize this step would be worthwhile if computer resources are limited.

6.4 Data-Set: Gyrokinetic Distribution Function

In the remainder of this chapter HOSVD is applied to the gyrocenter distribution function from a nonlinear simulation of ITG driven turbulence. As described in Sec. 2.1, the the gyrocenter distribution function is a function of three spatial coordinates and two velocity coordinates. In a tensor context, the gyrokinetic distribution function will be denoted as $\mathcal{G}$, or G_{ijklmn}. The parameters for the simulation are the

cyclone base case parameters discussed in Sec. 2.2 and summarized in Table 2.1. The perpendicular box size is $(L_x, L_y) = (126\rho_i, 126\rho_i)$, and the number of grid points is $16 \times 32 \times 8$ for the $(z, v_{||}, \mu)$ coordinates respectively. The perpendicular spatial resolution consists of 64 grid points in the x direction giving $k_{x,max}\rho_i = 1.56$, and 16 k_y Fourier modes for $k_{y,max}\rho_i = 0.75$. The full distribution function is output every 100 time steps. These parameters are identical to those in the standard parameter file distributed with each version of the GENE code, and define fairly standard (though rather low) resolution for this problem. The computation is performed in single precision and the total data set comprises ~ 8 gigabytes.

6.5 Mode Structures and Eigenvalue Spectra

This section presents information from coordinate modes and eigenvalues in order to illustrate the utility of the HOSVD in providing insight into the full gyrokinetic distribution function. In this section HOSVD is applied to a modified data-set; the full gyrokinetic distribution function is Fourier transformed from wavenumber space (k_x, k_y) to direct space (x,y) before it is analyzed. This is done in order to extract modes in the perpendicular directions that are more easily interpreted, and also has the benefit of converting the data set from complex to real data. This real (direct space) data set is only used to look at the mode structures; all other results (e.g., compression rates, etc.) use the raw data set. The eigenvalue spectra for both cases are very similar, indicating that the form (direct space or Fourier space) of the data set has little impact on such results.

For ITG turbulence with adiabatic electrons, zonal flows (67) (characterized, in part, as $k_y = 0$ fluctuations) are known to attain very high intensity. Thus it is unsurprising that the $n = 1$ binormal (y) mode structure represents this feature of

the turbulence - it is a near constant function of y as seen in Fig. 6.2. A series of other y modes are also shown in Fig. 6.2, where it is seen that the modes exhibit largely harmonic structures. Fig. 6.3 shows the Fourier spectra for the entire set of y modes. It is instructive to compare the mode structures in Fig. 6.2 with their Fourier spectra in Fig. 6.3. For instance, two scales are plainly visible for the $n = 10$ y mode as seen if Fig. 6.2. Fig. 6.3 verifies this by showing strong Fourier components at $k_y\rho_i = 0.25$, $k_y\rho_i = 0.1$, and $k_y\rho_i = 0.05$. Modes two through five have strong $k_y\rho_i = 0.2$, and $k_y\rho_i = 0.15$ components. Both of these examples suggest that there is some nonlinear phenomenon that couples certain scales. It is interesting to note that the growth rate peaks at $k_y\rho_i = 0.3$, but the nonlinear spectrum peaks at $k_y\rho_i = 0.2$. This observation of coupled scales could lend insight into this nonlinear downshift in the spectrum - a topic that could be pursued in future work. For $n > 10$ the Fourier spectra are strongly peaked about single wavenumbers indicating that a Fourier representation is well suited for those scales.

The radial mode structures exhibit many features in common with the binormal mode structures. The low n modes exhibit some coupling between different scales while the higher n modes are strongly peaked about single wavenumbers. A selection of radial mode structures is shown in Fig. 6.4 and the Fourier spectra are shown in Fig. 6.5.

A series of parallel mode structures is shown if Fig. 6.6. Again it is seen that the mode structures develop finer scale structure as n increases. Also, striking regularity is exhibited in their structure - they alternate between even and odd parity and add one additional peak with each increasing increment of n - a feature that is similar to many flavors of orthogonal polynomials. In spite of the lack of periodicity (for even numbers) in these modes, Fourier spectra are plotted in Fig. 6.7 in order to demonstrate their regularly decreasing scales.

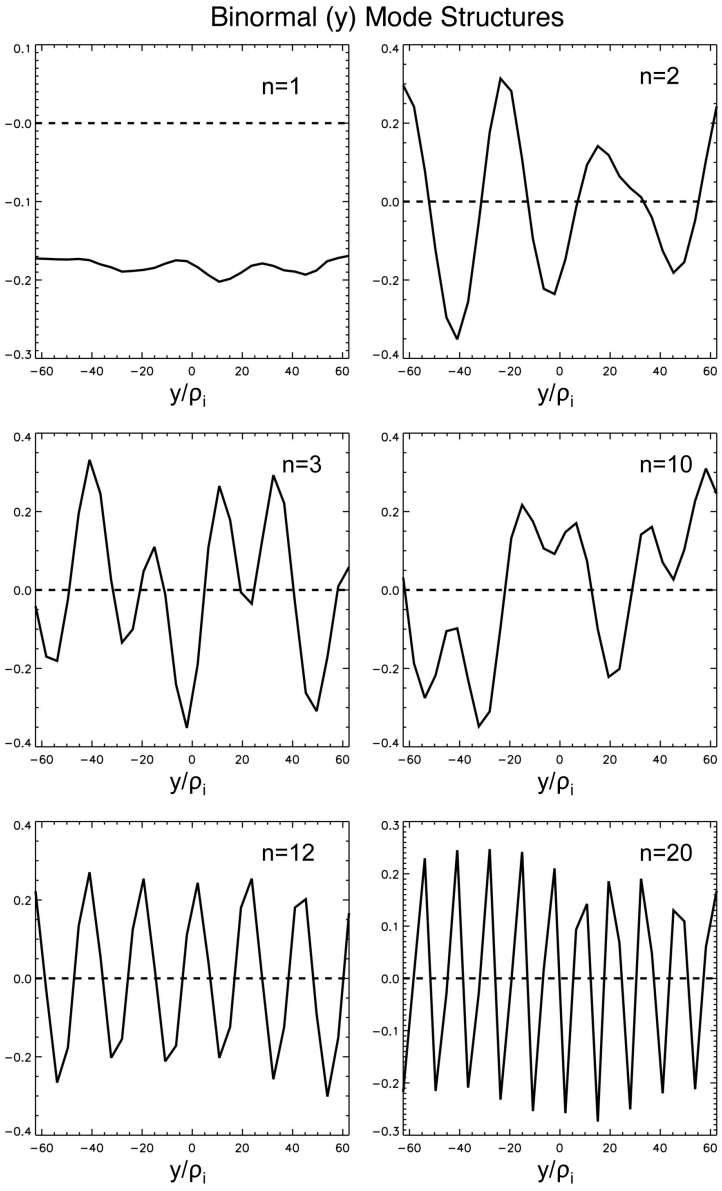

Figure 6.2: Selected mode structures for the binormal (y) coordinate.

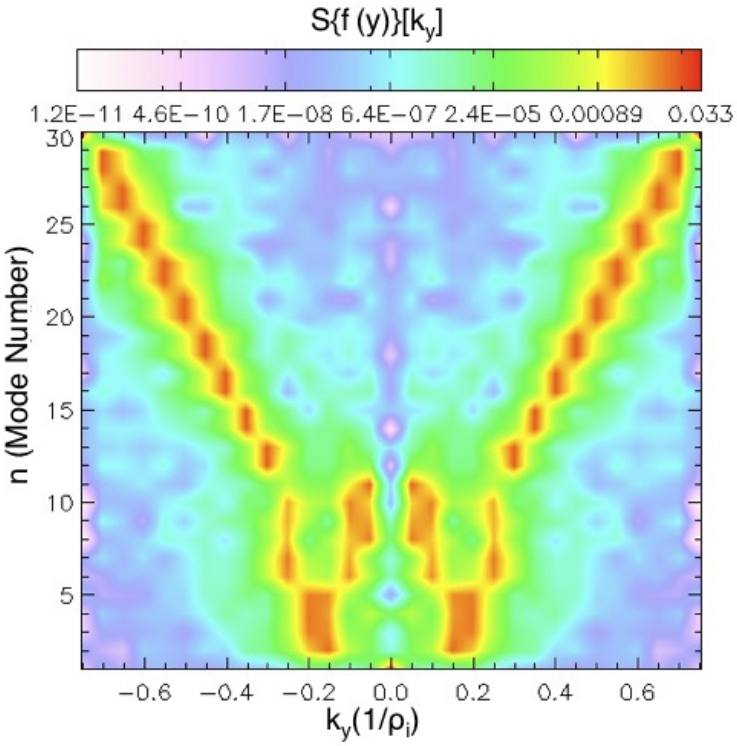

Figure 6.3: Fourier spectra of the y modes.

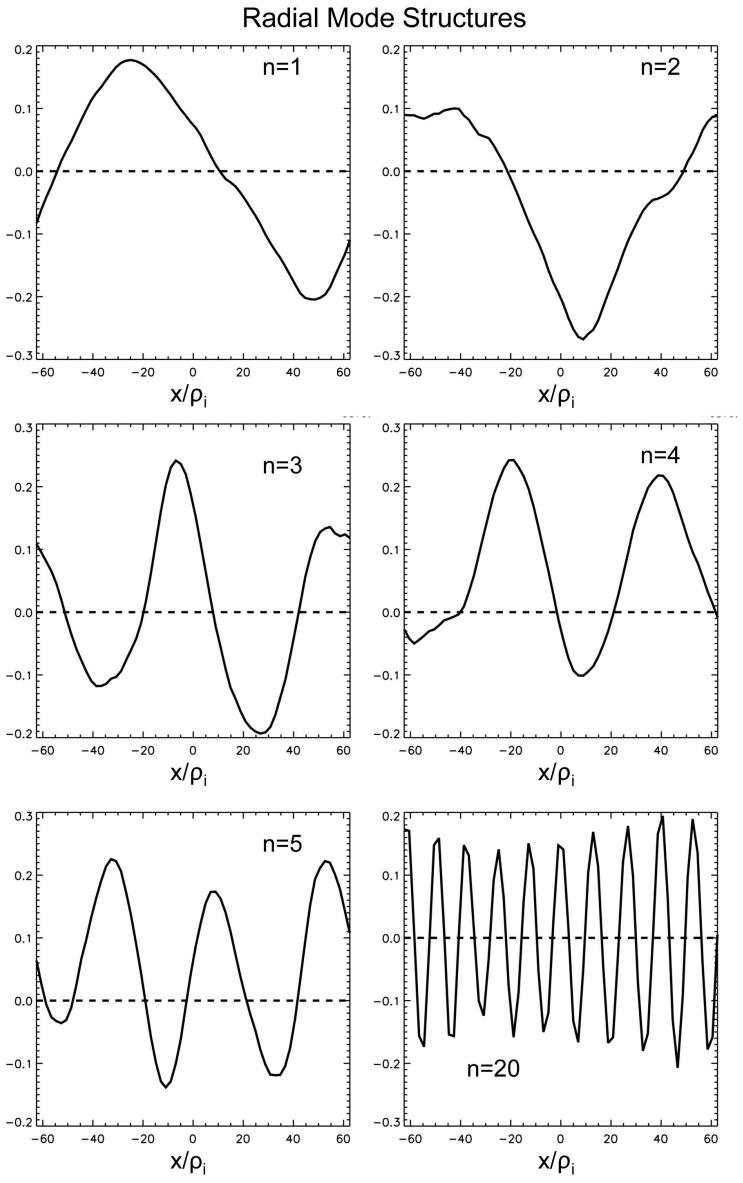

Figure 6.4: Selected mode structures for the radial (x) coordinate.

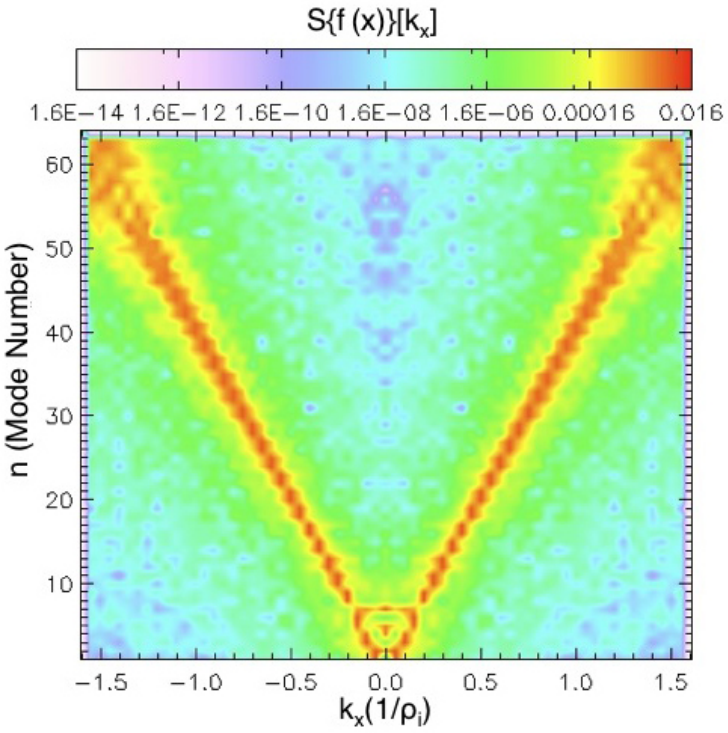

Figure 6.5: Fourier spectra of the x modes.

The $v_{||}$ modes also have a strong similarity to orthogonal polynomials; in this case they appear to be very similar to Hermite polynomials as seen in Fig. 6.8. This is verified for $n < 5$ in Fig. 6.9 where the Fourier spectra (A) and Hermite spectra (B) are plotted. It is seen that the Hermite spectra are sharply peaked at single values for $n < 5$. Certain studies (80) have analyzed $v_{||}$ dynamics in terms of Hermite polynomials and it appears that this representation is quite efficient for capturing the most important $v_{||}$ structures.

The μ modes exhibit very little structure as shown in Fig. 6.10. These have some features in common with Bessel functions - a representation that has also been used in the literature to represent this velocity space coordinate (65).

The $n = 1$ t mode corresponds to the zonal flows ($n = 1$ y mode) which are very low frequency fluctuations. This structure, along with several other t modes, is shown

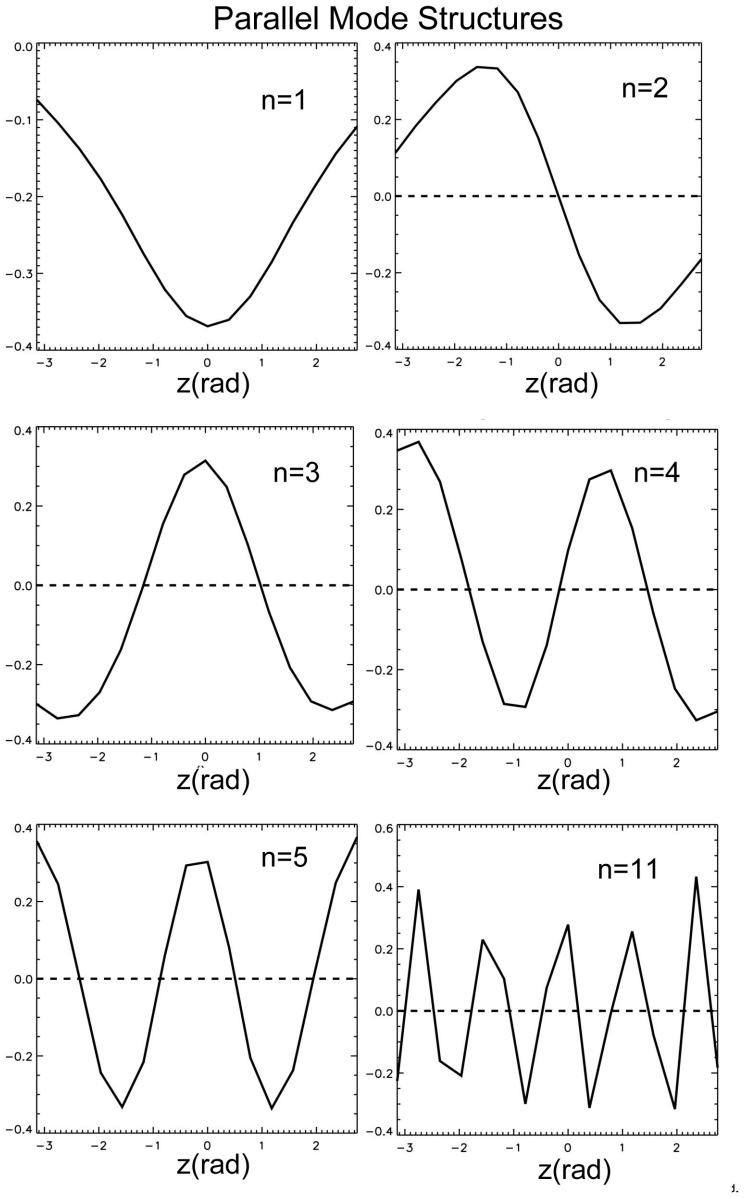

Figure 6.6: Selected mode structures for the parallel (z) coordinate.

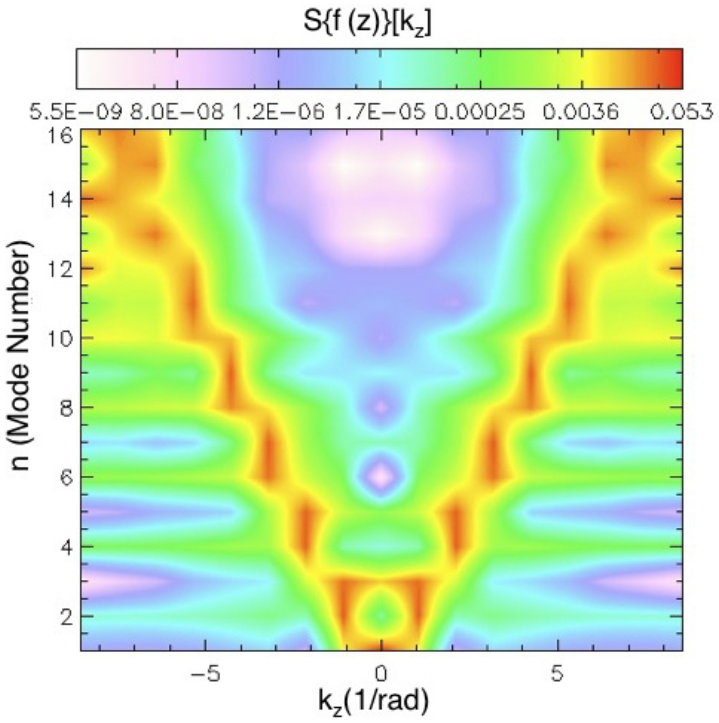

Figure 6.7: Fourier spectra of the z modes.

in Fig. 6.11. The corresponding frequency spectra are shown in Fig. 6.12 where it is seen that the modes exhibit broadband spectra.

Since the coordinate-eigenvalues define an error bound for a truncated HOSVD, the spectra of eigenvalues give an indication of the importance of each of the mode structures. The spectrum of eigenvalues for each of the six coordinates is shown in Fig. 6.13. It is observed that the eigenvalues for the velocity space coordinates fall off very sharply. One can then infer that only a few structures in velocity space are most important in the dynamics, and that the higher n structures can be dropped in a truncation without losing much of the data-set. In contrast, the eigenvalue spectra for the other coordinates drop of very gradually after a sharp initial decrease. This indicates broadband fluctuations in these coordinates.

Note that various coordinates are characterized by widely different types of struc-

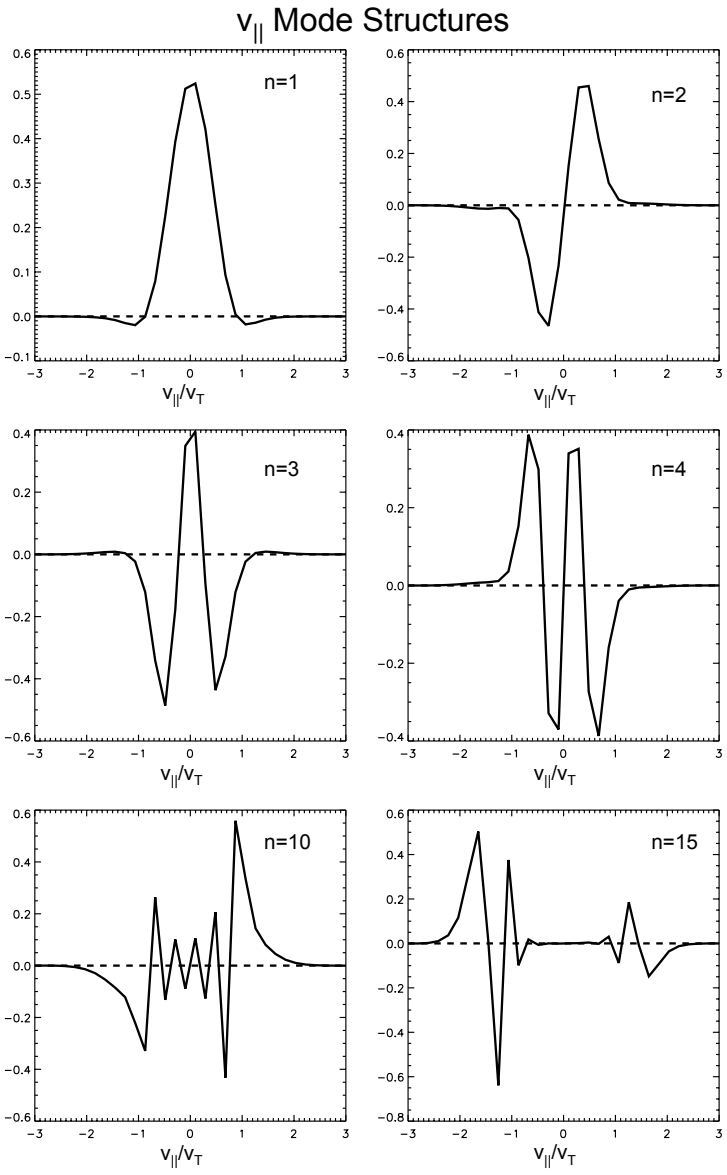

Figure 6.8: Selected mode structures for the $v_{||}$ coordinate.

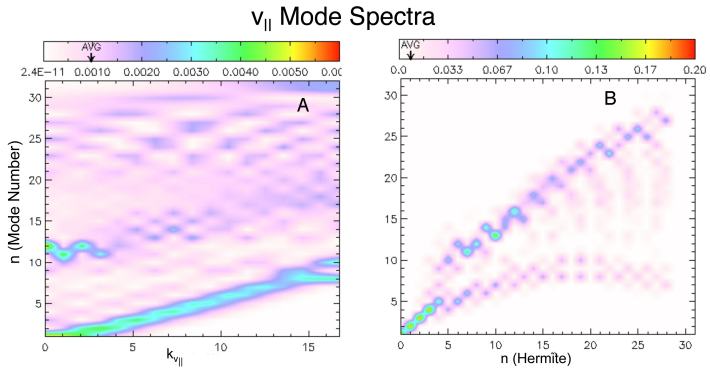

Figure 6.9: Fourier (A) and Hermite (B) spectra of the $v_{||}$ modes.

tures. The perpendicular directions x and y exhibit largely harmonic structures, the parallel z and $v_{||}$ modes are more akin to orthogonal polynomials, and the time structures fluctuate randomly. The HOSVD is able to extract these widely different behaviors in a single analysis. The HOSVD takes very little data to represent the mode structures and a lot of data to explain how they work together. While this is not always advantageous, it is easy and appealing to be able to visualize the structures that make up the entire data set at a glance. This would be useful, for instance, if one were exploring different possible coordinate bases in the process of designing or refining a code. The current analysis would indicate that representing $v_{||}$ with Hermite polynomials could offer significant advantages; since the the HOSVD $v_{||}$ modes are similar to Hermite polynomials and the corresponding $v_{||}$ eigenvalue spectrum drops off steeply, use of a Hermite representation could plausibly facilitate greater computational performance.

Note that all the results presented so far in this section have only used the coordinate modes and eigenvalues. This can be done without extracting any portion of the core tensor. As described in Sec. 6.2, the core tensor assigns a weight to each tensor (outer product between different combinations of coordinate modes) in the decomposition. The elements of the core tensor can be ordered by magnitude. This is plotted

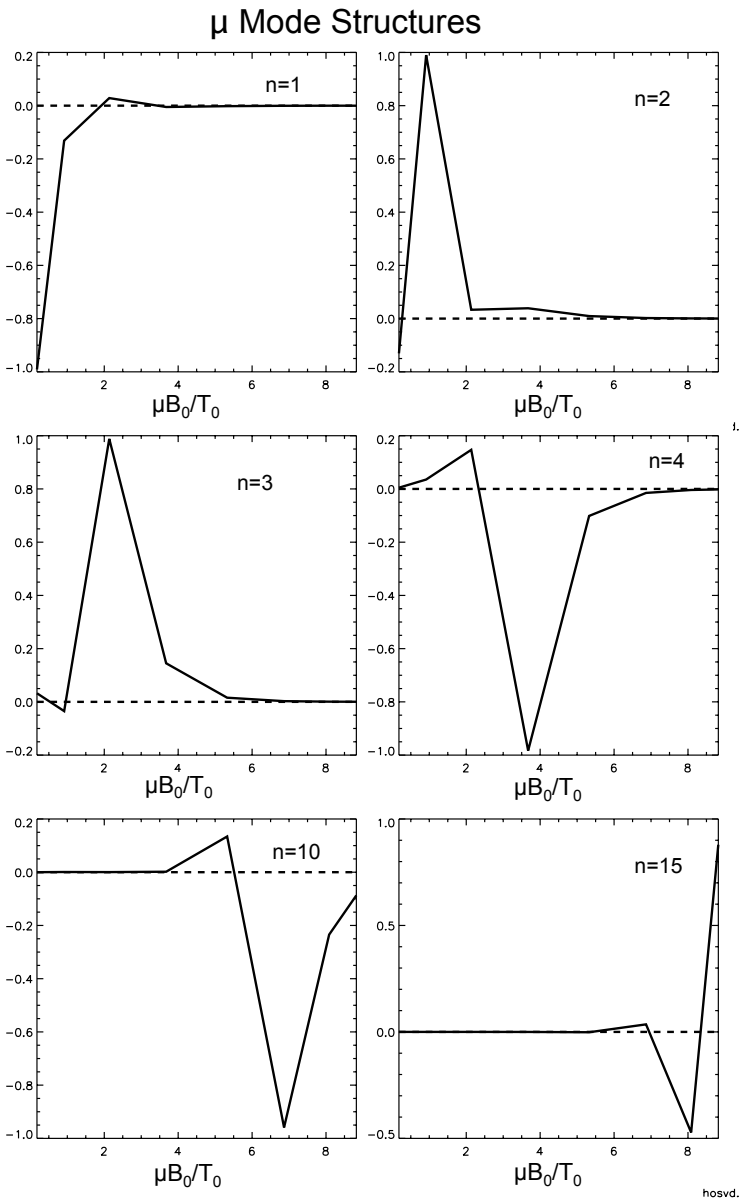

Figure 6.10: Selected mode structures for the μ coordinate.

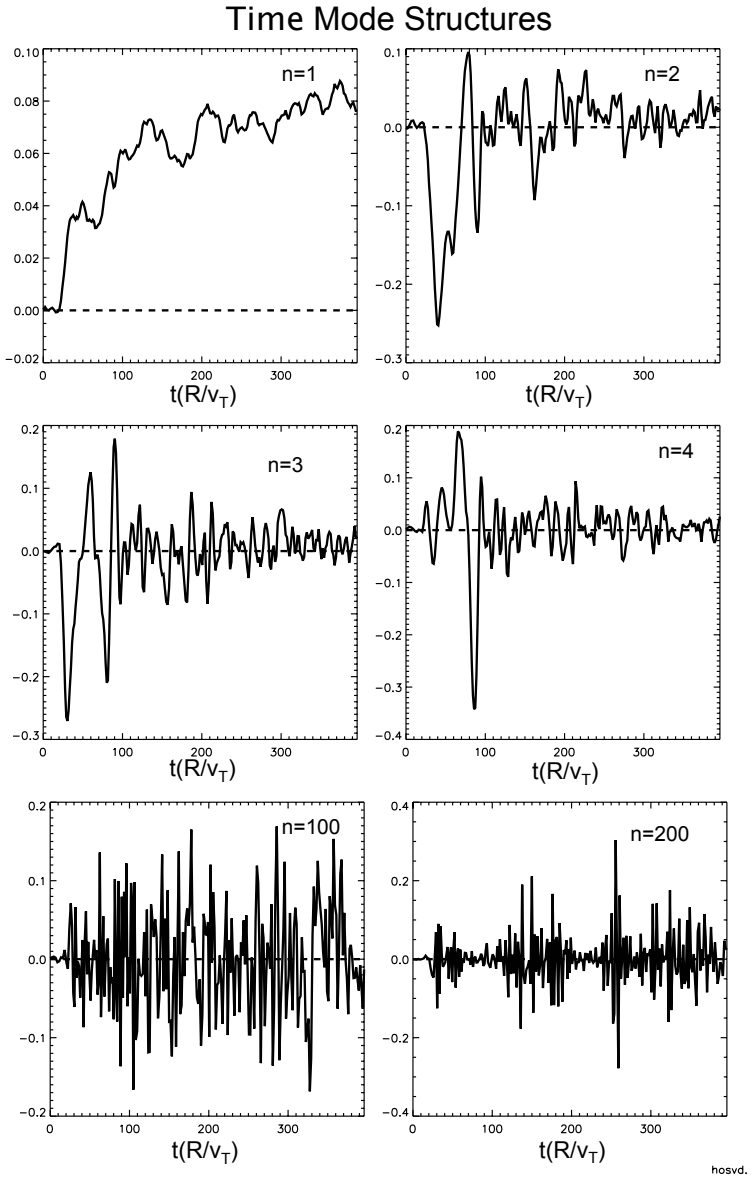

Figure 6.11: Selected mode structures for the time coordinate.

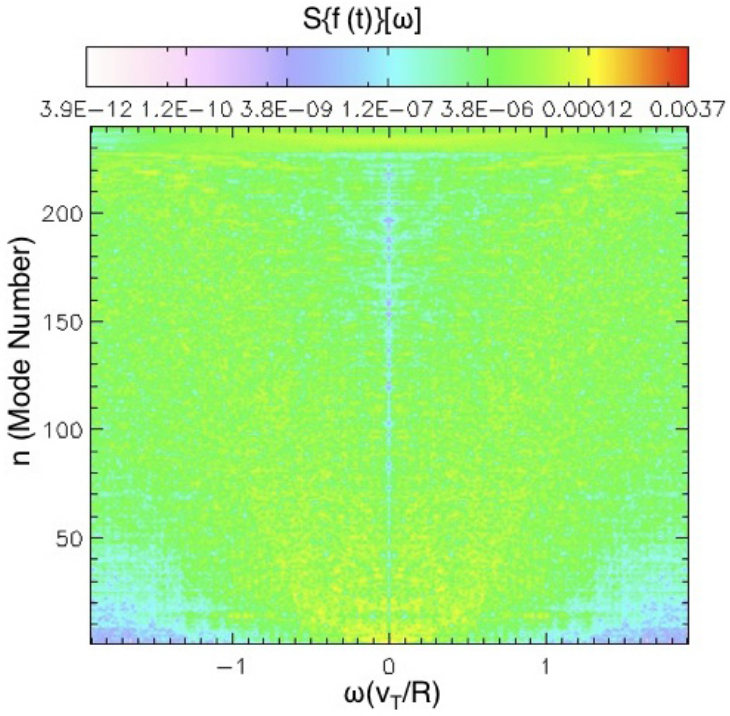

Figure 6.12: Frequency spectra of the time modes.

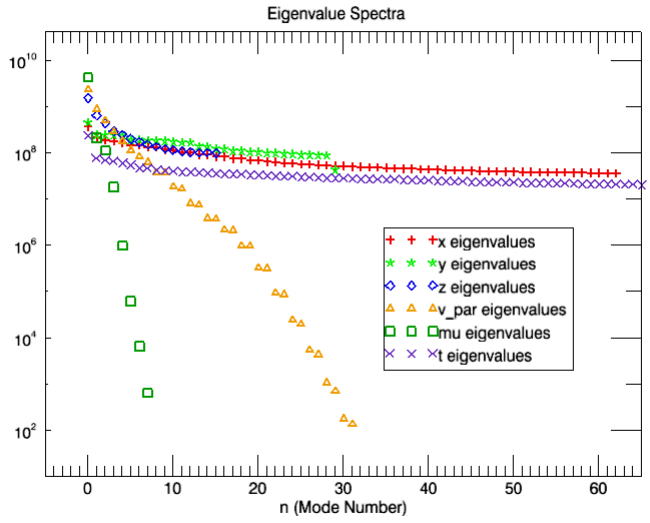

Figure 6.13: Spectra of coordinate eigenvalues.

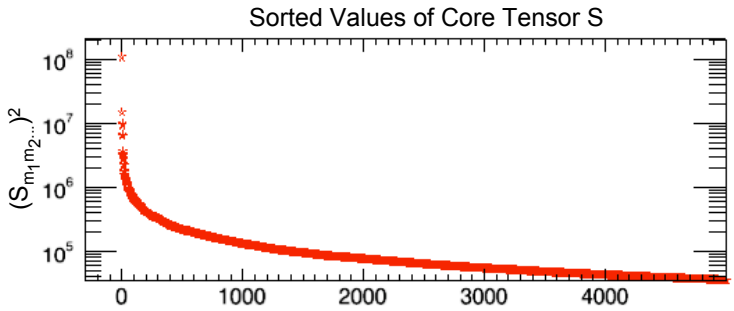

Figure 6.14: Spectrum of the largest 5000 squared elements of the core tensor

in Fig. 6.14 for the 5000 largest elements of the core tensor. The largest element of the core tensor is S_{111211}. This defines a weight for the outer product between the $n = 2$ $v_{||}$ mode and the $n = 1$ modes for all the other coordinates. These mode structures are plotted together in Fig. 6.15 for easy reference. Since the $n = 1$ y mode is part of this outer product, this reproduces some aspect of the zonal flow. The next four largest combinations also include the first y-mode. The largest combination which doesn't include the $n = 1$ y mode is weighted by S_{221113} - i.e., $n = 2$ for x and y modes, $n = 1$ for z, $v_{||}$, and μ modes, and $n = 3$ for the time coordinate. These are plotted together in Fig. 6.16 for easy reference.

6.6 Computation of the Core Tensor - Truncation and Compression

In this section performance results and compression rates are presented for a series of truncated HOSVDs with successively smaller error tolerances. Since a truncated HOSVD is characterized by multiple truncation ranks, there is a high degree of flexibility in selecting these ranks. The scheme used in this analysis takes an error tolerance as an input. After the coordinate-eigenvalues are calculated, a routine cycles through all possible truncation ranks that satisfy this error tolerance (as cal-

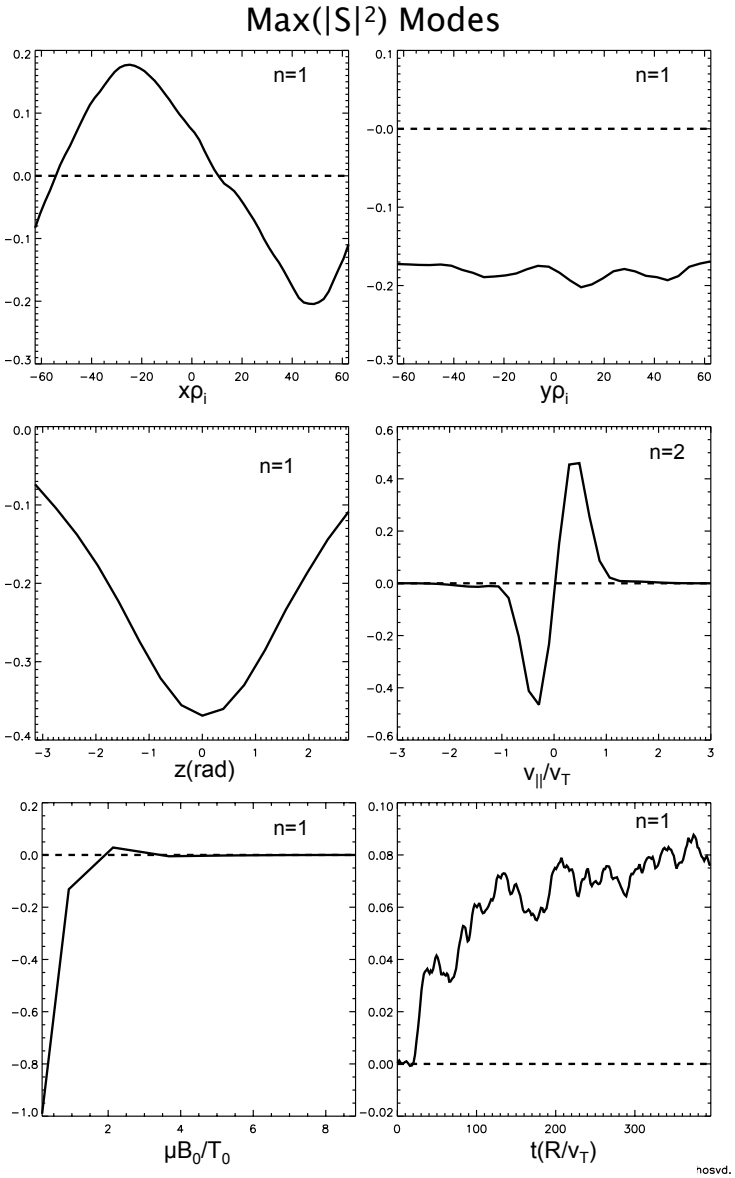

Figure 6.15: Plots of the coordinate mode structures associated with the largest value of the core tensor.

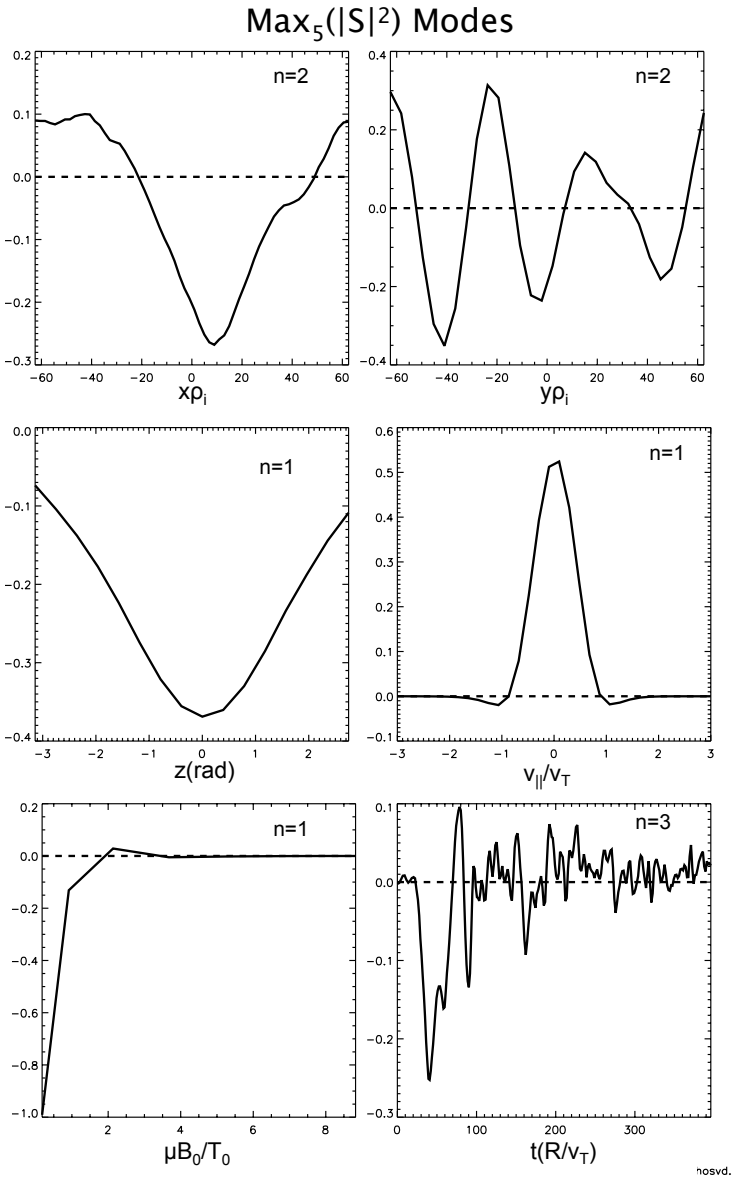

Figure 6.16: Plots of the coordinate mode structures associated with the largest value of the core tensor not associated with zonal modes ($n = 1$ y mode).

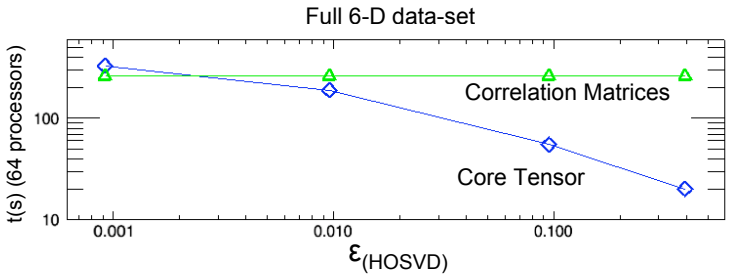

Figure 6.17: Plot of the computation time necessary to solve for the correlation matrices (green triangles) and the truncated core tensor (blue diamonds) plotted against truncation error.

culated using the error bound defined in Eq. 6.13), and selects the truncation ranks that correspond to the smallest possible inverse compression ratio, δ_{HOSVD} (defined in Eq. 6.17). The cpu time necessary to calculate the correlation matrices and the truncated core tensor is plotted against the truncation error in Fig. 6.17. The matrix multiplication, which is the most expensive step in calculating the core tensor, uses the highly optimized PCGEMM routine. As such, it is faster than the calculation of the correlation matrices for the smaller truncation ranks even though it entails more operations. Approximately 10.5 cpu hours (589 seconds on 64 processors) were necessary in order to calculate a truncated HOSVD within the 0.1% error tolerance. This use of computer resources is very manageable and much bigger problems would also be tractable. On the other hand it is expected that the data from many large gyrokinetic simulations (which include effects like kinetic electrons, electromagnetic effects, electron gyro-scale instabilities, etc.) could not be analyzed with a HOSVD with a reasonable allocation of computer resources. In cases like this, analysis and compression of individual time steps in the simulation could be useful and manageable.

The error for this series of truncated HOSVDs is plotted against the inverse com-

pression ratio in Fig. 6.18. The inverse compression ratio is,

$$\delta_{HOSVD}^{(r_{k_x} r_{k_y} r_z r_{v_{||}} r_\mu r_t)} = \frac{r_{k_x} n_{k_x} + r_{k_y} n_{k_y} + r_z n_z + r_{v_{||}} n_{v_{||}} + r_\mu n_\mu + r_t n_t + r_{k_x} r_{k_y} r_z r_{v_{||}} r_\mu r_t}{n_{k_x} n_{k_y} n_z n_{v_{||}} n_\mu n_t}, \tag{6.17}$$

and the (normalized) truncation error is,

$$\epsilon^{(r_{k_x} r_{k_y} r_z r_{v_{||}} r_\mu r_t)} = \frac{\|\mathcal{G} - \mathcal{G}^{r_{k_x} r_{k_y} r_z r_{v_{||}} r_\mu r_t}\|_F}{\|\mathcal{G}\|_F}, \tag{6.18}$$

where $\|\cdot\|_F$ denotes the square of the Frobenius norm. Fig. 6.18 shows that if one defines an error tolerance of, e.g., 10% (1%), then the data-set can be compressed to $\sim 4\%$ ($\sim 15\%$) of its original size. Decompositions like the SVD perform particularly well at extracting complex coherent structures that are not well described by the standard toolkit of special functions. In light of this, it is noteworthy that these compression rates can be achieved even for a data-set like the one considered here - a data set seemingly without dominant coherent structures. The truncation ranks are also noted in Fig. 6.18 for the $k_x, k_y, z, v_{||}, \mu, t$ coordinates, respectively (for reference, the full rank values are $(64, 16, 16, 32, 8, 240)$). Nearly all of the truncation is in the velocity space coordinates. This is consistent with the steep drop-off in the spectra of $v_{||}$ and μ eigenvalues shown in Fig. 6.13. This is another indication that a basis of some sort of orthogonal polynomial could be used to advantage in a code; for example, it may take a few dozen grid points for a finite difference method to resolve the same features that can be captured by a handful orthogonal polynomials. (On the other hand, these results may be applicable only to a limited region of parameter space and provide poor intuition with regard to modeling additional effects like, e.g., the trapped / passing electron orbit boundary for CTEM turbulence).

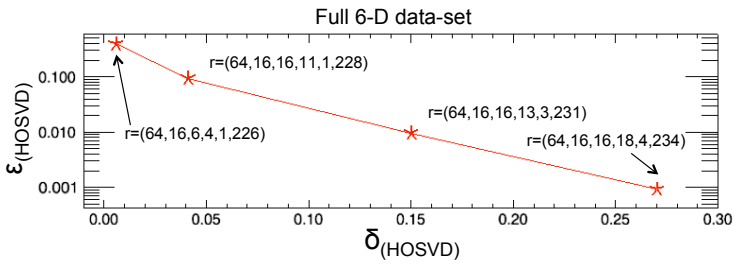

Figure 6.18: Plot of the truncation error versus inverse compression ratio for a series of truncated HOSVDs. The truncation ranks are noted for the $(k_x, k_y, z, v_{||}, \mu, t)$ coordinates respectively (out of a total of (64,16,16,32,8,240)).

6.7 Compression of the Gyrokinetic Distribution Function

One purpose for which HOSVD is particularly valuable is in data compression. The mathematical reasons why this is often expected to be the case will be discussed, and then computational results in this regard will be presented. For the purposes of this discussion, consider a D-dimensional tensor, $\mathcal{A}^{(D)}$, with an equal number of elements, n, in each coordinate, and HOSVD truncation ranks, r (also equal in each coordinate). The number of data elements it takes to store this truncated decomposition is $Drn + r^D$ (rn for each set of modes and r^D for the core tensor), and the size of the original data-set is n^D. Thus the inverse compression ratio for this truncation is,

$$\delta^{(r)}_{HOSVD} = \frac{Drn + r^D}{n^D} \approx \frac{r^D}{n^D}. \tag{6.19}$$

In order to perform a SVD on the same data set, the D-dimensional data tensor must be matricized. Assume that D is an even number and the tensor is matricized in such a way that the dimensions are split evenly between the columns and rows of the matrix: $\mathcal{A}^{(D)} \rightarrow A^{(n^{D/2} \times n^{D/2})}$. Now define a truncation rank, $r_{SVD} = r^D$, for the SVD so that the truncated SVD keeps the same number of terms (D-dimensional tensors) in

the series as the truncated HOSVD. This truncated SVD requires $r_{SVD}(1+2n^{D/2}) = r^D(1+2n^{D/2})$ data elements. The compression ratio for this SVD truncation is

$$\delta_{SVD}^{(r_{SVD}=r^D)} = \frac{r^D(1+2n^{D/2})}{n^D} \approx \frac{2r^D}{n^{D/2}}. \tag{6.20}$$

Note that the majority of the SVD data elements are in the singular vectors and very few data elements are necessary to define how the vectors combine in the decomposition. In contrast, the reverse is true for HOSVD; the core tensor (which defines how the modes combine) requires the vast majority of the storage and the modes themselves require relatively few data elements.

A comparison of Eqs. 6.19 and 6.20 indicates that the HOSVD truncation requires only a small fraction, $\mathcal{O}(n^{-D/2})$ of the memory required to store the SVD truncation, a feature that *improves* as the size n and the dimensionality, D, of the data-set increase. However, there is a large caveat in the fact that when the truncation ranks are equated in this manner ($r_{SVD} = r^D$), the SVD truncation error is guaranteed to not exceed the HOSVD truncation error (see Eq. 6.3). The HOSVD stores a given number of tensors with far fewer data elements than the SVD, but the SVD produces a smaller truncation error than the HOSVD for the same number of tensors. Which decomposition technique wins the compression comparison depends on a balance between these two properties. For the data set considered here, it is found that the storage advantages of HOSVD trump the optimality of SVD so that HOSVD achieves a much smaller truncation error for a given compression ratio.

In order to compare compression results for the two decompositions, one can plot truncation error against inverse compression ratio. Equations 6.17 and 6.18 define the inverse compression ratio and the truncation error for a truncated HOSVD of the full 6-D data-set. Eqs. 6.21 and 6.22 define the corresponding expressions for a

truncated SVD.

$$\delta_{SVD}^{(r)} = \frac{r(1 + n_{k_x} n_{k_y} n_z + n_{v_{||}} n_\mu n_t)}{n_{k_x} n_{k_y} n_z n_{v_{||}} n_\mu n_t}. \tag{6.21}$$

$$\epsilon^{(r)} = \frac{||\mathcal{G} - \mathcal{G}^{(r)}||_F}{||\mathcal{G}||_F}. \tag{6.22}$$

Compression rates are tested for a series of data-sets with increasing dimensionality - a 3-D data set $[g|_{(k_x\rho_i=0.0, k_y\rho_i=0.2, z=0)}(v_{||}, \mu, t)]$ consisting of the gyrokinetic distribution function at the outboard midplane $z = 0$ for $k_x\rho_i = 0.0$, and $k_y\rho_i = 0.2$, a 4-D data set which retains the z coordinate $[g|_{(k_x\rho_i=0.0, k_y\rho_i=0.2)}(z, v_{||}, \mu, t)]$, and a 5-D data set which additionally retains the k_y dependence $[g|_{(k_x\rho_i=0.0), k_y}(z, v_{||}, \mu, t)]$. The expressions for inverse compression ratio and truncation error for these reduced-dimensional data-sets can be recovered from the expressions in Eqs. 6.17, 6.18, 6.21, and 6.22 by dropping the terms corresponding to the reduced dimensions.

In Fig. 6.19, compression rates are plotted for the 3-D data-set for SVD (blue asterisks) and HOSVD (red diamonds). Even for 3 dimensions, HOSVD produces superior compression rates. Compression rates for the 4 and 5-D data sets are plotted in Figs. 6.20 and 6.21. For the four and five dimensional SVDs, two different schemes have been used to distribute the tensor into a matrix. First, all the 'spatial' coordinates are distributed in the rows of the matrix, and only the time coordinate varies with the columns (blue asterisks). This is a common technique which produces separate spatial and time basis vectors (sometimes topos and chronos) as done in Refs. (60),(68),(69), and Chaps. III-V. The second method is to distribute the coordinates more evenly between the columns and the rows (green plus signs).

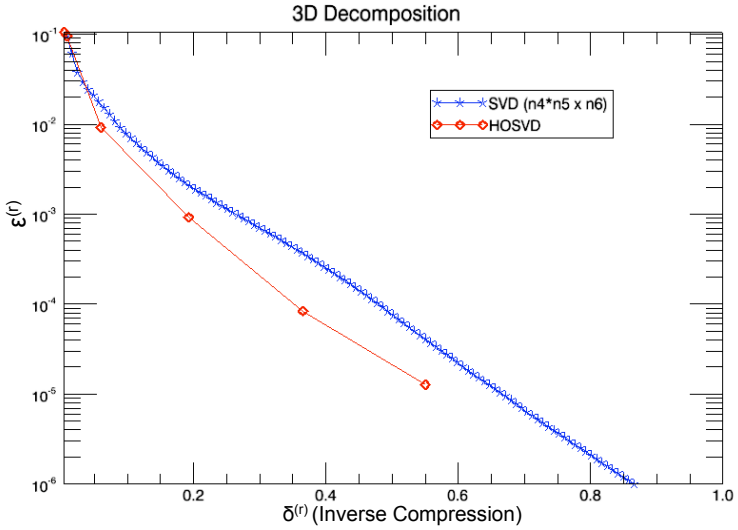

Figure 6.19: Comparison of truncation error versus inverse compression ratio for HOSVD (red diamonds) and SVD (blue asterisks). HOSVD achieves a smaller truncation error for a given inverse compression ratio.

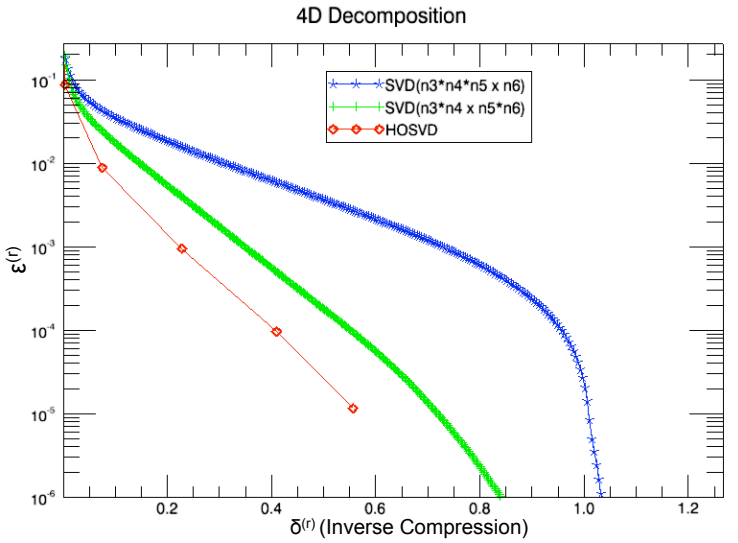

Figure 6.20: Comparison of truncation error versus inverse compression ratio for HOSVD (red diamonds) and two applications of SVD. The blue asterisks denote SVD applied to a matrix where the time coordinate is the only coordinate varying along the columns, and the green plus signs denote SVD applied to a matrix where the coordinates are more evenly distributed. HOSVD achieves a smaller truncation error for a given inverse compression ratio.

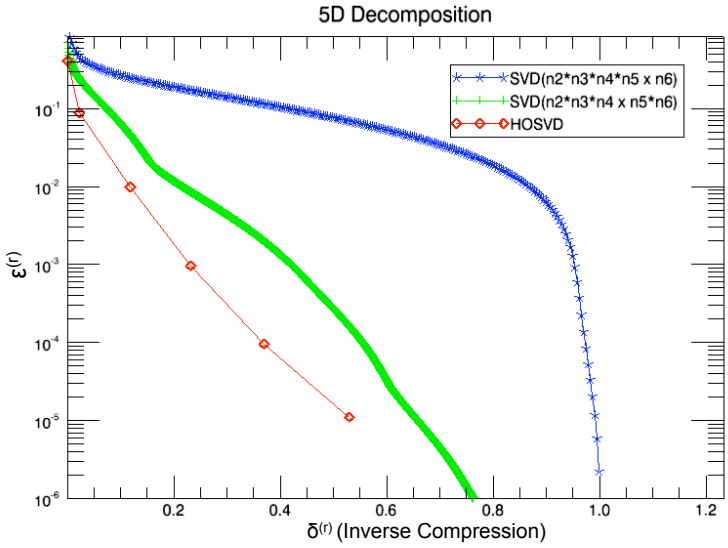

Figure 6.21: Comparison of truncation error versus inverse compression ratio for HOSVD (red diamonds) and two applications of SVD. The blue asterisks denote SVD applied to a matrix where the time coordinate is the only coordinate varying along the columns, and the green plus signs denote SVD applied to a matrix where the coordinates are more evenly distributed. HOSVD achieves a smaller truncation error for a given inverse compression ratio. This distinction is amplified as the dimensionality increases as can be seen by comparing this figure with Figs 6.19 and 6.20.

This makes interpretation of the basis vectors more difficult, but is advantageous for compression as seen in Figs. 6.20 and 6.21. In either case, HOSVD (red diamonds) significantly out-performs SVD. To illustrate this consider a situation where a truncation is held to an error tolerance of 0.01. As illustrated in Fig. 6.21 for the 5-D data set, a truncated HOSVD could compress the data set to $\sim 12\%$ of its original size whereas the truncated SVDs could only compress it to $\sim 21\%$ (or $\sim 87\%$ for the topos-chronos method). Analysis of this series of increasingly high dimensional data-sets also demonstrates that the advantages of HOSVD with regard to compression are augmented as the dimensionality increases.

An alternative comparison of SVD and HOSVD is to plot the spectra of SVD singular values (squared) and their HOSVD analogues - the elements of the core tensor (squared). By the theorem shown in Eq. 6.3, SVD must perform better in this comparison. Recall that the sum of the squares of the SVD singular values (elements of the HOSVD core tensor) is equal to the 'energy' in the entire data-set, and the square of each singular value (element of the core tensor) denotes the amount of 'energy' in each tensor in the series. This comparison is plotted for the 5-D data set in Fig. 6.22 where all three panels show the same data at increasing (from top to bottom) zoom levels. There are a total of 1920 singular values and ~ 15 million elements in the core tensor (5000 of which are shown in this plot). From this plot it is clear that only a small number of terms in the HOSVD are competitive with their SVD counterparts. The first ten or so elements of the core tensor are smaller but comparable to the SVD singular values. For numbers beyond a few dozen, the HOSVD is quite inefficient when measuring by this standard.

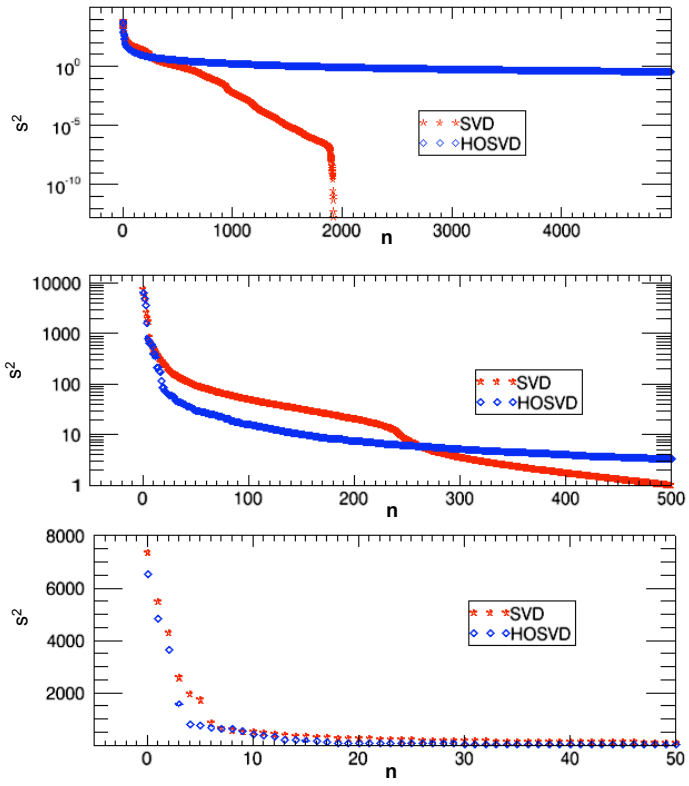

Figure 6.22: Plot of squared singular values from an SVD (blue diamonds) and the 5000 (of ∼15 million) largest squared elements of the core tensor from an HOSVD. The data is the same in all three panels viewed with increasingly zoomed (from top to bottom) plot ranges. The SVD captures more 'energy' for any given number of modes.

6.8 Summary

This chapter has described the application of the tensor decomposition, HOSVD, to analysis of gyrokinetic data. HOSVD has many properties that make it well suited to analyzing high-dimensional data-sets like the full 5-D plus time gyrokinetic distribution function. An efficient, scalable HOSVD routine was created by matricizing the important operators and implementing a parallel routine. The ~ 8 GB data-set representing the full distribution function from a gyrokinetic simulation was analyzed using HOSVD with a very modest allocation of computer resources. HOSVD produces mode structures independently for each coordinate. This offers insight into efficient ways of representing each coordinate and provides a unique view of the underlying data. HOSVD is very efficient at compressing high-dimensional data and is shown to out-perform SVD in this regard.

CHAPTER VII

Inference of Damped Mode Effects Without the Use of Mode Decompositions

7.1 Introduction

Initial efforts were made to identify damped mode excitation in gyrokinetic turbulence before the mode decomposition techniques described in Chap. III were developed. These results were published in Ref. (88). Many of these results have been superseded by the explicit demonstration of damped mode excitation in Chaps. III and IV. Nonetheless, much of this early work provides insight into, e.g., possible ways to infer damped mode activity in an experiment. In this chapter, many of the results from Ref. (88) will be recounted along with additional insight which has been gained from the work described in Chaps. II-V.

In this chapter, comparisons are made between frequencies, growth rates, and cross phases (from an eight field, two dimensional, gyro-Landau fluid model - GLF23 (91)) and frequency spectra and cross-phases from nonlinear gyrokinetic simulations using the GYRO code (53).

7.2 Frequency Spectra

The following subsection describes comparisons between linear mode frequencies and nonlinear frequency spectra. These are described as they were understood at the time - before the use of gyrokinetic GENE eigenmode solver and the corresponding mode decompositions. A retrospective commentary is provided in Sec. 7.2.2.

7.2.1 Comparisons of Mode Frequencies With Nonlinear Spectra

Two distinguishing features of a linear eigenmode are its frequency (eigenvalue) and its phase relations (eigenvector). If multiple modes are excited to significant amplitudes in a turbulence simulation, one would expect their corresponding mode frequencies to appear in the frequency spectrum. Such is the case with the geodesic acoustic mode (89) whose linear mode frequency is readily identified in the nonlinear spectrum. The transport model, GLF23, is used to examine the frequencies and phases of multiple linear eigenmodes. GLF23 is based on an eight field gyro-Landau-fluid model, yielding eight modes. Any fluid representation is a projection of a kinetic equation onto a set of fluid variables, constructed by taking moments of the kinetic equation and making approximations to close the moment hierarchy. Thus, the eight modes accessible to GLF23 should be conceptualized as being representative of the modes accessible to the gyrokinetic equation, albeit a finite set.

For CYCLONE-base-case parameters, GLF23 produces the unstable ITG mode and five stable modes whose frequencies cluster around the ITG mode frequency, and whose damping rates are on the same order of magnitude as the ITG growth rate. Two other very high frequency (10^5 times larger than the ITG frequency), heavily damped modes were dismissed. It is unlikely that these modes are physical.

The linear mode frequencies from GLF23 closely match regions of intensity in

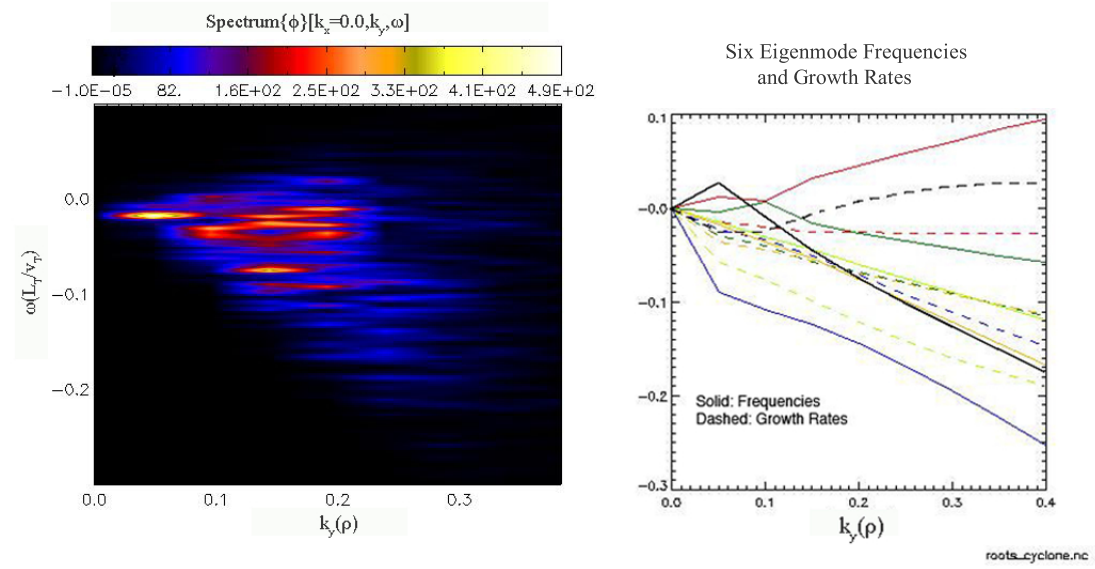

Figure 7.1: Comparison of the nonlinear frequency spectrum from GYRO simulation data (left) with the frequencies of the ITG mode and five other stable modes (right) as calculated from GLF23 as a function of k_y, plotted on the same plot range. The frequencies of the unstable modes closely match regions of intensity in the nonlinear spectrum for a wide range of wavenumbers.

the nonlinear frequency spectrum from a corresponding GYRO simulation. In all regions of k-space, the frequencies of the five damped modes fall in areas of significant intensity in the nonlinear frequency spectrum as evident in Fig. 7.1 (as a function of k_y), and Fig. 7.2 (as a function of k_x). Figure 7.1 shows that both the spread in linear mode frequencies and the width of the nonlinear spectrum are roughly proportional to k_y. In addition, the damped mode frequencies seem to be *representative* of the nonlinear spectrum, defining a range of excitation.

Although there is a dearth of theory in the literature regarding frequency spectra, it is commonly believed that the linear growth rate provides an estimate of the expected width of a spectrum (92). The basic argument is as follows. On average, nonlinear energy transfer must balance the linear energy input due to the instability

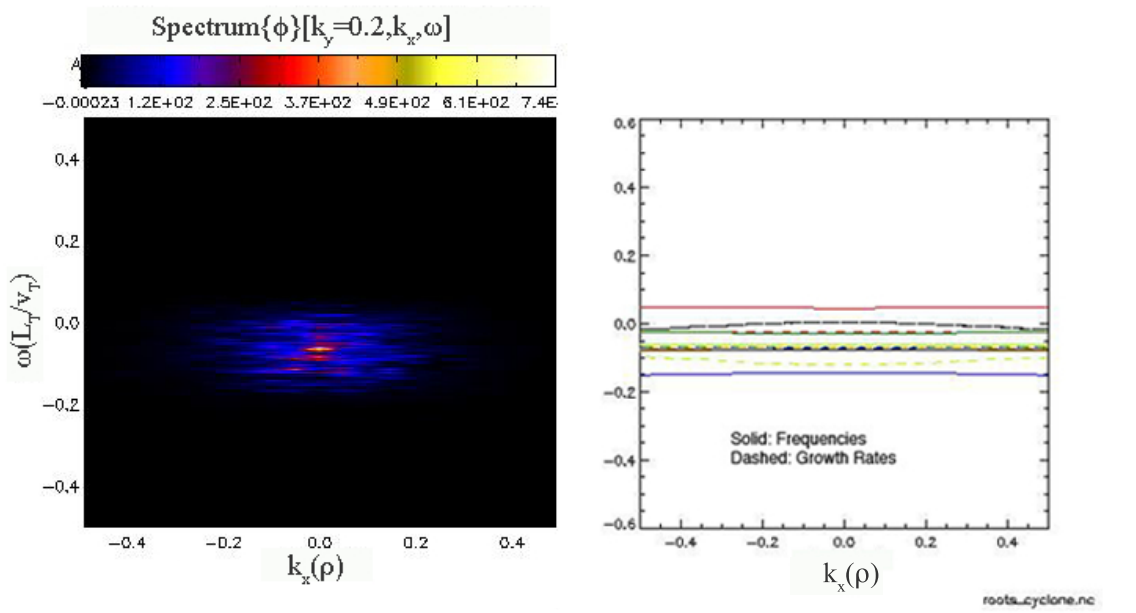

Figure 7.2: Comparison of the nonlinear frequency spectrum from GYRO simulation data (left) with the frequencies of the ITG mode and five other stable modes (right) as calculated from GLF23 as a function of k_x, plotted on the same plot range. The frequencies of the unstable modes closely match regions of intensity in the nonlinear spectrum for a wide range of wavenumbers.

in order to saturate turbulence. This requirement sets an upper limit on the extent to which nonlinear interactions can modify temporal dynamics and thus broaden a frequency spectrum.

For all wavenumbers examined, the width of the frequency spectrum is much larger than the linear growth rate. This is difficult to explain without invoking the presence of other accessible normal modes with characteristic frequencies represented in the nonlinear spectrum. A scan in temperature gradient scale length, L_T, was examined in order to determine the dependence of spectrum width on the linear growth rate. Figure 7.3 shows the spectra for the wavenumber $k_y\rho_i = 0.2$, $k_x\rho_i = 0$ for a series of L_T values. The central vertical line represents the ITG mode frequency and the solid line on the frequency axis shows the linear growth rate. The spectra for all values of L_T have comparable widths in spite of an increase by a factor of 3 in the growth rate. A corresponding scan of GLF23 runs shows that the width of the spread in damped mode frequencies varies only weakly with L_T and remains close to the widths of the nonlinear spectra. The width of frequency spectra can also be affected by Doppler shifting due to zonal flows. However, the L_T scan also eliminates Doppler shifting as the primary cause of the width of the spectra since the zonal flow velocity increases strongly with R/L_T as well. Figure 7.4 shows a plot of the width of the nonlinear frequency spectra in comparison with the spread in damped eigenmode frequencies, linear growth rate, and zonal flow velocity for the wavenumber $k_x\rho_i = 0$ and $k_y\rho_i = 0.2$. The nonlinear spectrum scales well with the spread in damped eigenmode frequencies but does not scale with either the linear growth rate or the zonal flow velocity.

It should be noted that GLF23 parameter scans show that the spread in linear mode frequencies is only weakly dependent on gradient scale lengths and safety factor, but strongly dependent on magnetic shear, $\hat{s}$. The frequency spread is much narrower

for low values of $\hat{s}$. However, this behavior is not observed in the nonlinear spectrum of GYRO simulations which still show wide spectra similar to higher $\hat{s}$ spectra. If the low $\hat{s}$ nonlinear spectrum is to be interpreted in terms of available linear eigenmodes, one must assume that there are important eigenmodes at low $\hat{s}$ that are not captured by GLF23's eight field fluid closure or that GLF23 does not capture the correct shear dependence of the damped eigenmode frequencies.

7.2.2 Retrospective Commentary

As described in Chap. III, a very large number of modes are excited in the nonlinear turbulence. The GLF23 eigenmodes have frequencies that are in the same frequency range as the weakly damped modes shown to be excited in Sec. 3.3, but their damping rates are significantly larger. Nonetheless it is plausible that they capture some of the same effects. The direct comparison between linear eigenmode frequencies and the nonlinear spectra is, in retrospect, rather simplistic. With a mode decomposition, one can calculate nonlinear frequency spectra for each mode by calculating the frequency spectrum of $h^{(n)}(t)$ (recall Eq. 3.1). It is found that the frequency spectrum of each mode (including the unstable mode) exhibits a broadband spectrum which is very similar to the total frequency spectrum. This indicates that nonlinear interactions largely trump the linear mode frequencies in defining the spectrum. The failure of the width of the nonlinear spectrum to scale with several expected influences (linear growth rate, shearing rate, etc., as described in the previous subsection) remains compelling. In addition, it is found that net spectrum roughly matches the range of frequencies represented by the weakly damped gyrokinetic eigenmodes (this can be seen, in part, in Fig. 3.2). It is plausible that each excited eigenmode contributes a time scale to the nonlinear interactions in such a way that the nonlinear spectrum represents the underlying spectrum of linear mode frequencies. However,

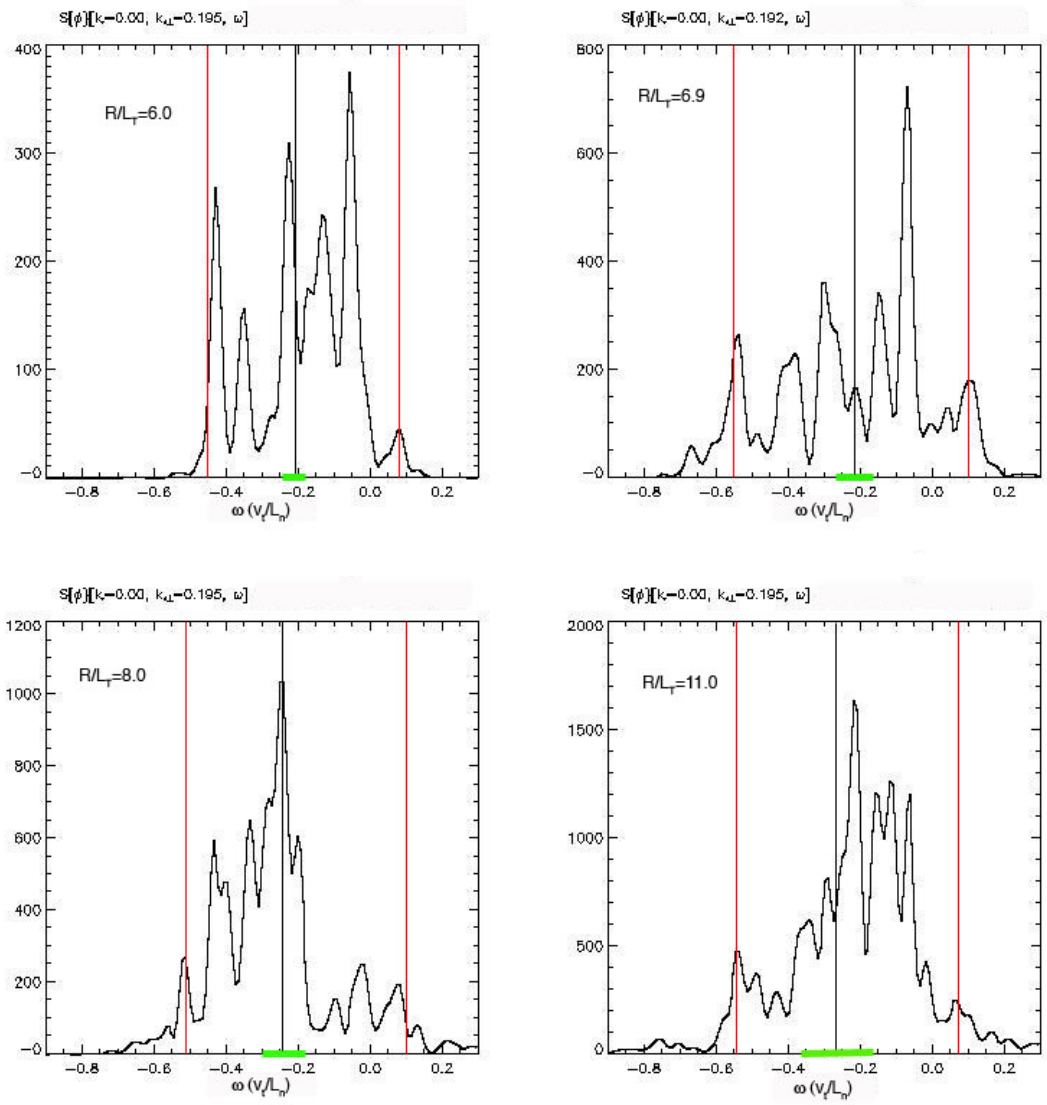

Figure 7.3: Frequency spectra for an L_T scan. The central vertical lines represent the ITG frequency, the outlying vertical lines show the width of the spectrum taken for Fig. 7.4, and the horizontal bar on the axis represents the linear growth rate. In all instances the frequency spectra are much wider than the linear growth rate. In addition, the widths of the spectra remain similar throughout the scan in spite of an increase in the growth rate by a factor of three. The spread in damped mode frequencies varies little with L_T and closely matches the width of the nonlinear spectra as seen in Fig. 7.4.

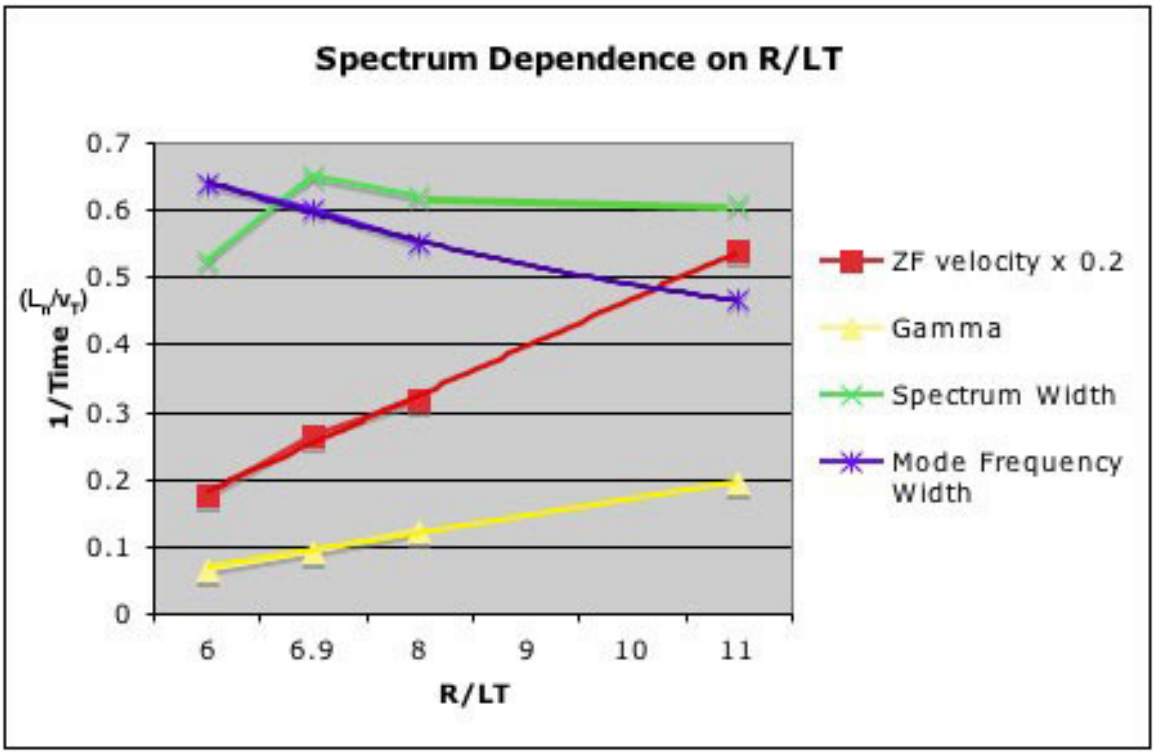

Figure 7.4: Plot of the width of the nonlinear frequency spectrum (as shown by the vertical lines in Fig. 7.3) at $k_x\rho_i = 0, k_y\rho_i = .2$ in comparison with other quantities that might determine the width of the spectrum. The linear growth rate and the zonal flow velocity increase significantly over the L_T scan. However, the widths of the nonlinear spectra vary little and are matched closely by the spread in eigenmode frequencies.

this has not been explicitly demonstrated.

7.3 Transport Fluxes

The following subsection describes comparisons between nonlinear fluxes and quasilinear estimates. This is described as it was understood at the time, and a retrospective commentary is provided in Sec. 7.3.2.

7.3.1 Comparisons of Quasilinear and Nonlinear Fluxes

Excitation of damped eigenmodes in fluid models generally causes a reduction in transport fluxes. Their effect on energy balance and transport can roughly be conceptualized as the opposite of an instability, i.e., they dissipate energy from the fluctuations allowing gradients to steepen. In order to illustrate the effect of damped eigenmodes on heat flux, we write the electrostatic potential and pressure fluctuations as a superposition of six modes corresponding to the six modes defined by GLF23,

$$\phi = \beta_1 + \beta_2 + \beta_3 + \beta_4 + \beta_5 + \beta_6, \tag{7.1}$$

$$p = R_1\beta_1 + R_2\beta_2 + R_3\beta_3 + R_4\beta_4 + R_5\beta_5 + R_6\beta_6, \tag{7.2}$$

$$Q(k) = k_y Im(\phi(k)^* p(k)). \tag{7.3}$$

The R_i are complex coefficients defining the correct $\phi^* p$ cross phases for each eigenmode. The heat flux, Eq. 7.3, is proportional to the $\phi^* p$ cross correlation. The heat

flux can also be expressed in the eigenmode basis as,

$$Q(k) = k_y \mathrm{Im}(\sum_i R_i \beta_i^2 + \sum_{i,j \neq i} R_i \beta_i \beta_j^*). \tag{7.4}$$

The β_i^2 are positive definite so the direction of the flux contribution from these terms depends only on the coefficients $\mathrm{Im}(R_i)$. The contribution of cross terms is more difficult to characterize. This is the topic of current study with the reduced three-field ITG model, where it appears that (with some interesting exceptions) these terms largely cancel out so that the flux is dominated by the β_i^2 terms. Damped mode phase data are available from GLF23 and indicate that three of the five damped modes would give an inward contribution to heat flux. The unstable mode gives an outward component of flux, as do the two most weakly damped modes, albeit at a significantly reduced level in comparison to the unstable mode. As a result, damped mode excitation causes a net reduction in heat flux in comparison with the transport that would result solely from the instability.

In order to estimate the magnitude of the effect of damped eigenmodes on transport, comparisons are made between the quasilinear flux and the true flux. Quasilinear theory estimates fluxes assuming that the dynamics are governed solely by the unstable mode. A quasilinear flux is constructed by multiplying the ϕ^2 intensity from a nonlinear simulation by the linear response function from a linear simulation as shown in Eq. 7.5. For an initial value code, a linear simulation can only identify the fastest growing mode so all quantities (phases, frequencies, etc.) derived from the data are associated with the instability. As a result, this procedure amounts to replacing p in the heat flux expression with the estimate $p = R_1 \phi$ which is accurate only if the fluctuations lie almost exclusively on the unstable manifold. This amounts

to keeping only the $R_1\beta_1^2$ term in Eq. 7.4,

$$Q_{ql}(k) = k_y \mathrm{Im}(R_1(k)\phi^2(k)). \tag{7.5}$$

In order to construct a quasilinear flux, the response function R_1 is taken from a linear GS2 (54) run and is used in conjunction with data from a nonlinear GYRO simulation. GS2 is capable of initializing a linear simulation for a range of radial wavenumbers, whereas GYRO is limited to $k_x\rho_i = 0$ for linear simulations. The response function is plotted in Fig. 7.5. Using data from these two codes should not be a problem, as GS2 and GYRO have been extensively benchmarked for CYCLONE-base case parameters. Comparisons between GS2 and GYRO were made for $k_x\rho_i = 0$ wavenumbers and the quasilinear fluxes agree to within 2%.

The quasilinear flux is a good estimate of the true flux in the linear phase before nonlinear energy transfer excites damped eigenmodes. This corresponds to $t<80L_T/v_T$ in Fig. 7.6, which shows the two fluxes as functions of time starting from infinitesimal initial conditions. In the saturated state, the quasilinear flux consistently overestimates the true flux as would be expected when damped eigenmodes are excited. This is seen in Fig. 7.6 after $t \approx 80L_T/v_T$, and in a longer time history of the two fluxes in Fig. 7.7. The ratio of total true flux to quasilinear flux is, on average, 0.64. At $k_x\rho_i = 0$, the ratio is 0.79 and the quasilinear estimate grows increasingly poor as k_x increases, as seen in Fig. 7.8.

These comparisons indicate that damped eigenmodes have an effect of approximately 36% on transport fluxes.

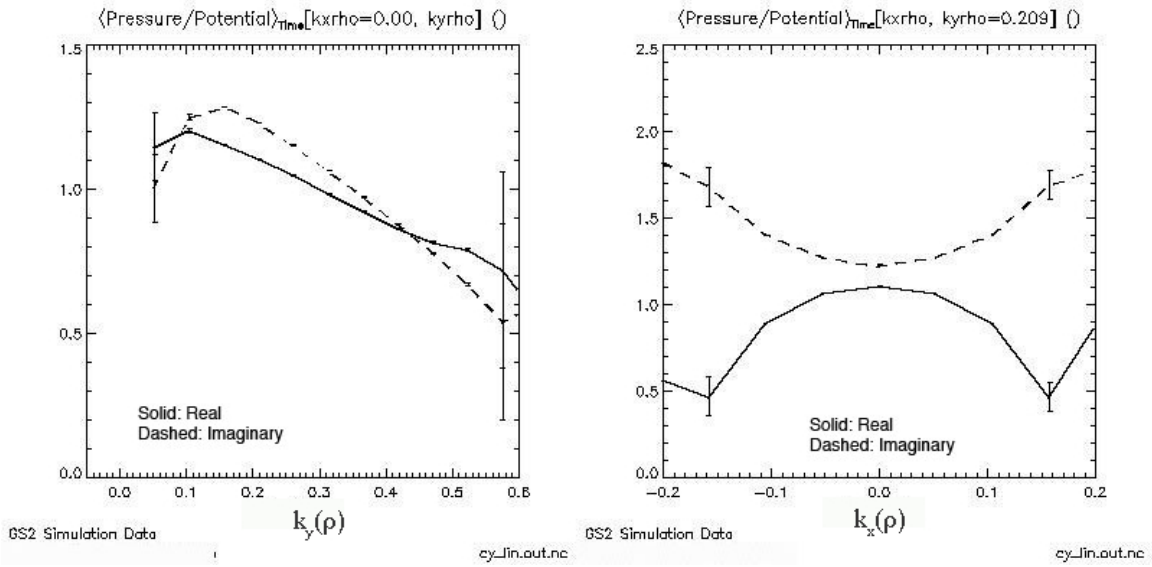

Figure 7.5: The linear response function P/ϕ from linear GS2 data for $k_x\rho_i = 0$ as a function of k_y(left), and $k_y\rho_i = 0.2$ as a function of k_x right.

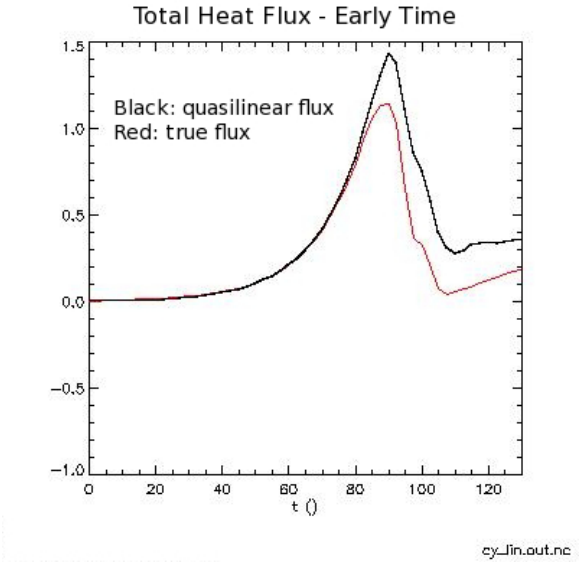

Figure 7.6: A comparison of the quasilinear and true fluxes during the linear growth phase and the transition from the linear to nonlinear regime. At early times, the two fluxes are identical but diverge when nonlinear energy transfer excites damped eigenmodes.

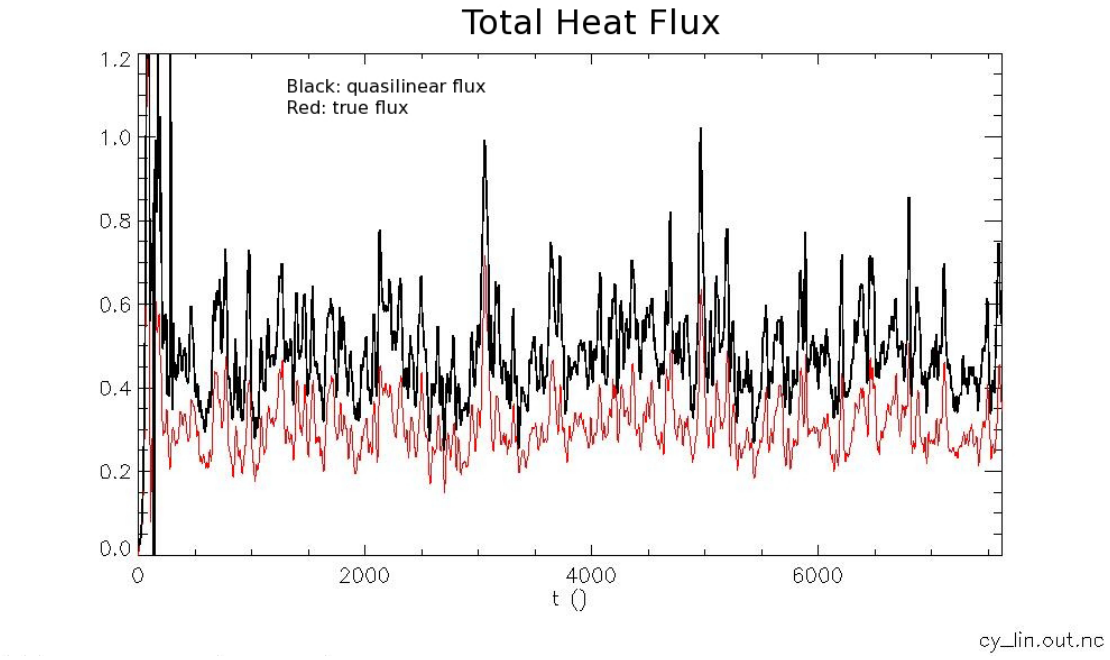

Figure 7.7: A long time history of the quasilinear and true heat fluxes. On average, the true flux is 64% of the quasilinear flux.

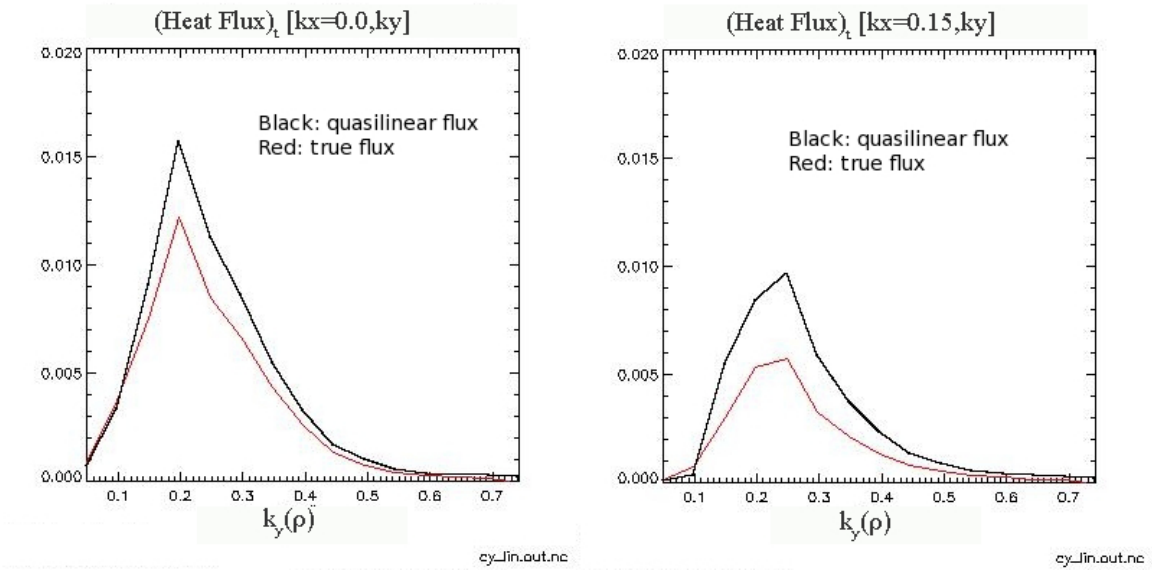

Figure 7.8: A comparison of the quasilinear and true fluxes at $k_x\rho_i = 0$ as a function of k_y (left), and $k_x\rho_i = 0.15$ as a function of k_y (right). The quasilinear approximation worsens as k_x increases.

7.3.2 Retrospective Commentary

In light of the results in Sec. 4.2 (where it is noted that the unstable mode defines $\sim 95\%$ of the transport) it may, at first glance, be surprising that there is a significant reduction from quasilinear transport estimates. In actuality, these results are not inconsistent, as will be explained in this subsection.

Consider a simplified mode decomposition with two modes for the electrostatic potential and the pressure,

$$\begin{aligned} \phi &= \phi_1 + \phi_2 \\ P &= P_1 + P_2, \end{aligned} \tag{7.6}$$

where,

$$\begin{aligned} P_1 &= R_1 \phi_1 \\ P_2 &= R_2 \phi_2 \end{aligned} \tag{7.7}$$

The second mode in this decomposition can be thought of as a simplified representation of the aggregate effect of all subdominant modes. This simplified mode decomposition will be used to compare three different fluxes (Eqs 7.8-7.10). For simplicity, assume the cross terms are zero as would be the case in a POD decomposition. The total flux is

$$Q_{tot} \propto R_1 \langle \phi_1^* \phi_1 \rangle + R_2 \langle \phi_2^* \phi_2 \rangle. \tag{7.8}$$

The quasilinear flux described in the previous subsection is

$$Q_{QL} \propto R_1 \langle \phi^*_{tot} \phi_{tot} \rangle = R_1 (\langle \phi^*_1 \phi_1 \rangle + \langle \phi^*_2 \phi_2 \rangle). \tag{7.9}$$

Also of interest is the flux described in Sec. 4.2 which is the flux associated exclusively with the the unstable mode,

$$Q_1 \propto R_1 \langle \phi^*_1 \phi_1 \rangle. \tag{7.10}$$

For clarity, the following is a summary of claims regarding the fluxes in Eqs. 7.8-7.10:

1) In the previous subsection it is stated that Q_{QL} is approximately 36% larger than Q_{tot}.

2) In Sec. 4.2 it is stated that Q_1 is approximately $< 5\%$ smaller than Q_{tot}.

Thus one quasilinear estimate is larger than the total flux and the other is smaller. The expressions in Eq. 7.8-7.10 reveal how this is consistent. Q_1 is smaller that Q_{tot} because R_2 is slightly positive (see Fig. 4.4 B where the value for $n = 2$ is positive but smaller than that of $n = 1$, and the rest of the values are randomly distributed about 0). In addition, Q_{QL} is larger than Q_{tot} because R_1 is much larger than R_2 (this can also be seen in Fig. 4.4 B where the $n = 1$ value is much larger than the rest). Thus the two results are consistent. In addition, the calculation of Q_{QL} in the previous subsection and its comparison with the total flux is a valid test regarding the excitation of damped modes: in the case that $\phi_2 = 0$ the two would be exactly the same. It is also of note that even in the event of slightly positive transport associated with damped modes (as is the case for the results presented in Chap. IV), damped mode excitation still produces a reduction from quasilinear flux estimates: the subdominant modes produce a slight outward transport, but they do so at a lesser rate than the unstable mode.

7.4 Phase PDFs

The following subsection describes comparisons between nonlinear fluxes and quasilinear estimates. This is described as it was understood at the time, and a retrospective commentary is provided in Sec. 7.3.2.

7.4.1 Comparisons of Linear and Nonlinear Cross-Phases

The eigenvector of a linear eigenmode defines cross-phase relations between fields. Nonlinear cross phases in saturated turbulence are the result of the interaction between all excited eigenmodes. Heat flux is expressed in terms of the cross phase between electrostatic potential and pressure fluctuations, and so is dependent on the eigenmodes that make up the fluctuations, as discussed in the previous section. We examine pdfs of phase angles $\tan^{-1}[\mathrm{Im}(p^*\phi)/\mathrm{Re}(p^*\phi)]$ to better understand the behavior of nonlinear cross phases and their relation to damped eigenmode excitation.

A phase-angle pdf is constructed by tracking (for different wavenumbers) the number of instances in time when the phase angle falls in different angular ranges. In addition, the pdf can be intensity weighted, amplifying the probability by a factor proportional to the instantaneous intensity, ϕ^2. This serves to highlight regions (in time and k-space) that are important for transport, and makes phase pdfs smoother. However, it is unclear what information is eliminated during this process. For instance if damped eigenmode excitation is associated with periods of low intensity, then intensity weighting acts to filter out the damped eigenmode contribution to phase angle dynamics. We consider both weighted and unweighted phase angle pdfs in this paper. Intensity weighted pdfs are examined in Reference (41) where nonlinear phase pdfs are compared to the linear phase angles of the unstable mode for CTEM turbulence. There is a close correspondence between linear and nonlinear phase angles, which

leads the authors of Ref. (41) to conclude that the dynamics are governed by the unstable mode. In this work, a correspondence is also observed between phase pdfs and linear mode phase angles. However, the peak of the pdf about the linear phase angle is broadened. While the width is smaller than the spread $\Delta\omega$ of the frequency spectrum, we will show that it is consistent with the excitation of other modes.

A long time simulation (2800 time steps corresponding to $t(v_T/L_T) = 500$ to 7500) was used to create phase angle pdfs. The intensity weighted phase pdf at $k_x = 0$ as a function of k_y is shown in Fig. 7.9 A. It is observed that the phase pdf is peaked near the phase angle of the most unstable mode for most wavenumbers. The exception is $k_y\rho_i = 0.05$ where there is a secondary peak that aligns with the linear phase angle and a larger peak which is offset from the linear angle, as seen in Fig. 7.9 B. The larger peak may correspond to another mode or it may reflect the net effect of multiple interacting modes. Fig. 7.10 shows two unweighted phase pdfs that are representative of most phase pdfs. The phase pdfs have widths that range from roughly 0.5 radians to 1.5 radians and also exhibit non-Gaussian 'tails' and 'bumps'. While there is little in the literature regarding phase pdfs, it is plausible that many of these features are signatures of multiple mode excitation. Linear theory defines a single phase angle for each eigenmode, not a peaked distribution of phase angles.

For nonlinear data, one would expect some nonlinear broadening but it is unclear how large this effect would be. A phase pdf with a finite width can be easily explained by the interaction of multiple modes. Consider the interaction between a dominant mode ϕ_1 and another mode ϕ_2 with smaller amplitude, different phase angle, and frequency as modeled by:

$$\phi = \phi_1 e^{-i\omega_1 t} + \phi_2 e^{-i\omega_2 t}, \tag{7.11}$$

$$p = \phi_1 e^{-i\alpha_1} e^{-i\omega_1 t} + \phi_2 e^{-i\alpha_2} e^{-i\omega_2 t}. \tag{7.12}$$

The dominant and subdominant mode phase angles / frequencies are represented by α_1 and α_2 / ω_1 and ω_2 respectively. Taking ϕ_2/ϕ_1 as a small parameter, the phase angle, $\tan^{-1}[\mathrm{Im}(p^*\phi)/\mathrm{Re}(p^*\phi)]$ can be expanded to first order in ϕ_2/ϕ_1:

$$\alpha_{nl} = \alpha_1 + \frac{\phi_2}{\phi_1} \frac{tan(\alpha_1)}{1 + tan^2(\alpha_1)} A(\alpha_1, \alpha_2, (\omega_1 - \omega_2)t), \tag{7.13}$$

$$\begin{aligned} A(\alpha_1, \alpha_2, (\omega_1 - \omega_2)t) = & \frac{sin(\alpha_1 + (\omega_1 - \omega_2)t) + sin(\alpha_2 + (\omega_2 - \omega_1)t)}{sin(\alpha_1)} \\ & - \frac{cos(\alpha_1 + (\omega_1 - \omega_2)t) + cos(\alpha_2 + (\omega_2 - \omega_1)t)}{cos(\alpha_1)}. \end{aligned} \tag{7.14}$$

The nonlinear phase angle has a constant term (α_1) and a smaller amplitude term (proportional to ϕ_2/ϕ_1) oscillating at the beat frequency. This would manifest itself in a phase pdf as a peak at the dominant phase angle with a width proportional to the ratio of the mode amplitudes. This analysis applied to more than two modes would produce a similar result, i.e., a pdf peaked at the dominant phase angle with a width dependent on the relative mode amplitudes.

In order to develop more intuition regarding the structure of phase angle pdfs, a simple modeling exercise was undertaken. Heuristic signals for the electrostatic potential and pressure were created to model the interaction of multiple modes in creating a nonlinear phase angle. The electrostatic potential is modeled by taking the electrostatic potential signal from a long time simulation for a single wavenumber ($k_x\rho_i = 0, k_y\rho_i = 0.15$) near the peak of the spectrum in a nonlinear GYRO simulation. This signal is divided into six sections representing six linear eigenmodes,

$$\phi = \beta_1 + \eta(\beta_2 + \beta_3 + \beta_4 + \beta_5 + \beta_6), \tag{7.15}$$

$$p = R_1\beta_1 + \eta(R_2\beta_2 + R_3\beta_3 + R_4\beta_4 + R_5\beta_5 + R_6\beta_6). \tag{7.16}$$

As in Eq. 7.1, β_1 represents the unstable eigenmode and the remaining β_i represent the damped eigenmodes. Each β_i is modeled by a time segment of the long time simulation data. The damped eigenmodes are reduced in amplitude by the factor η. The pressure signal is created by multiplying the same mode signals (β_i) by complex constants (R_i), which give them the correct phase angles (as calculated by GLF23) for the different modes [Eq. 7.16]. A net phase angle is determined from these heuristic pressure and potential signals and a phase pdf is calculated. It is observed that the phase pdf is peaked near the unstable mode phase angle for a wide range of η. As η is increased, the phase pdf broadens and other features (secondary peaks, 'bumps', and 'tails') become more prominent. For each value of η, an energy ratio can be calculated ($\eta^2(\sum_{i=2,6}\gamma_i)/\gamma_1$). This energy ratio is the ratio of the rate of energy dissipation (due to the damped modes) to the energy input rate (from the instability). The model phase pdfs most closely match the true nonlinear pdf when the energy ratio is between 0.20 and 0.44, i.e., the damped modes are dissipating roughly 30% of the energy input by the instability. This is consistent with the magnitude of the effect of damped eigenmodes on transport fluxes as estimated in the previous section.

7.4.2 Retrospective Commentary

This analysis of nonlinear cross-phases remains valid and very pertinent in light of the established excitation of a hierarchy of damped modes as described in Chap. III. The estimates of dissipation due to damped modes have been superseded by the explicit calculations presented in Sec. 4.2.

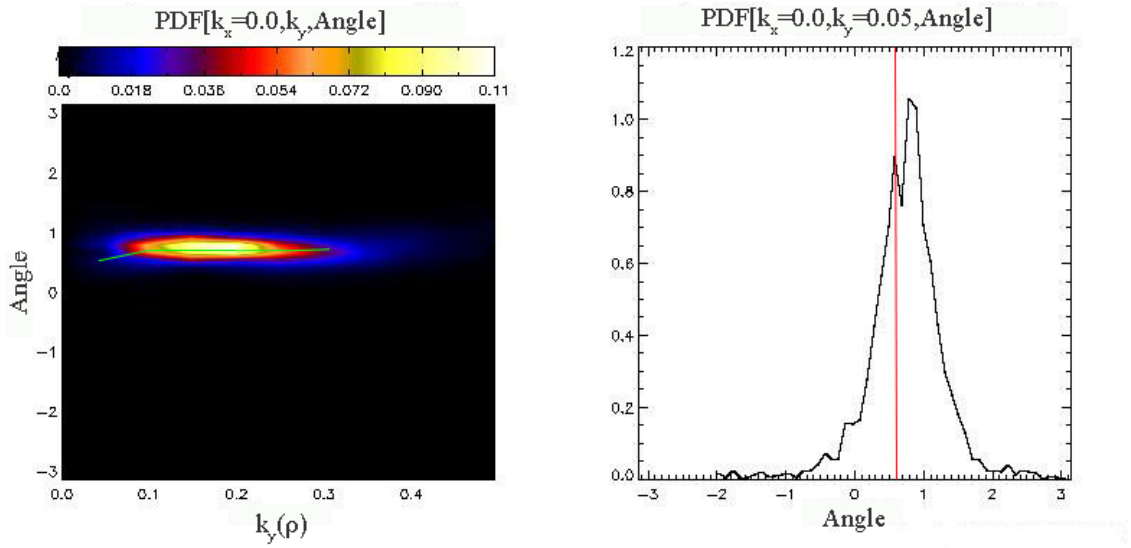

Figure 7.9: Left: Intensity weighted phase pdf at $k_x\rho_i = 0$ as a function of k_y. The line represents the linear phase angle. Right: Unweighted phase pdf for the wavenumber $k_x\rho_i = 0, k_y\rho_i = .05$. The vertical line represents the most unstable mode phase angle, which corresponds to a secondary peak in the phase pdf.

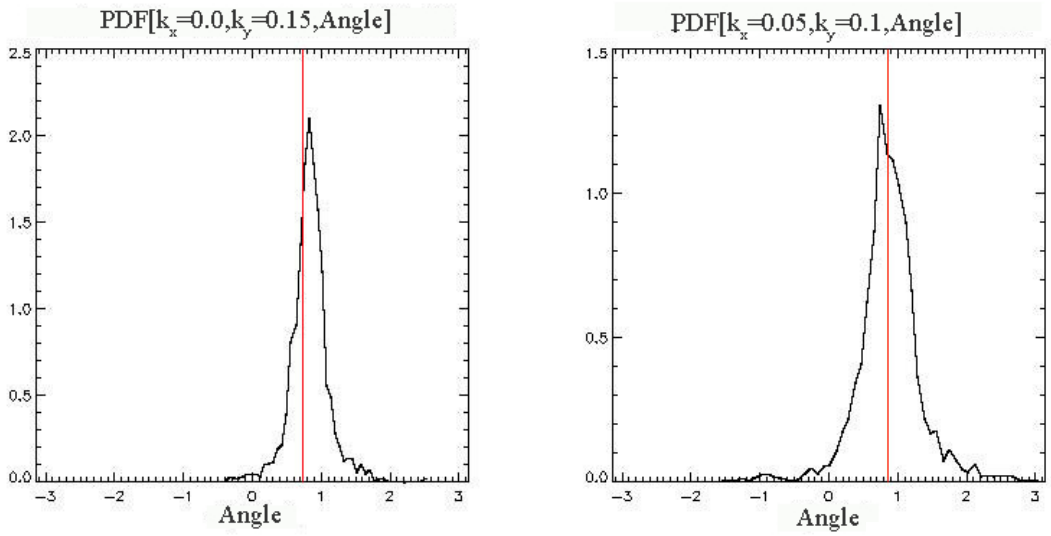

Figure 7.10: Unweighted phase angle pdfs for $k_x\rho_i = 0.05$, $k_y\rho_i = 0.1$ (left),and $k_x\rho_i = 0, k_y\rho_i = 0.15$ (right). The vertical lines represent the most unstable mode phase angle. These phase pdfs are representative of many wavenumbers that exhibit widths ranging from 0.5 to 1.5 radians and non-Gaussian 'tails' and 'bumps'.

7.5 Damping of Zonal Modes

In Ref. (88) the distinction is made between zonal modes (any fluctuation at $k_y\rho_i = 0$) and the Hinton-Rosenbluth zonal flow (90). It is noted that, while a zonal flow is very weakly damped and unlikely to be a major dissipator of energy, other damped modes at $k_y\rho_i = 0$ may, indeed, be more strongly damped and define a potent energy sink. With the development of the energy diagnostics described in Sec. 2.4, it was revealed that significant dissipation does occur at $k_y\rho_i = 0$ but it is not larger than other regions of the spectrum (see Fig. 4.2). A strongly fluctuating cross phase (and correspondingly broad phase pdf) is also reported for zonal modes in Ref. (88). This is an interesting observation which has not been pursued and could be the topic of further study.

7.6 Summary

In summary, this chapter has reviewed preliminary results examining gyrokinetic data without the use of a gyrokinetic eigenvalue solver or mode decomposition techniques. Comparisons of quasilinear and nonlinear fluxes remain instructive. It was shown that the quasilinear flux shown in Eq. 7.5 overestimates the true flux. This is a valid indicator of damped mode excitation. This result is discussed in light of results from Sec. 4.2 in Sec. 7.3.2. Results in this chapter also demonstrate how the excitation of subdominant modes modify cross-phases by broadening the width of a phase pdf.

CHAPTER VIII

Summary, Conclusions, and Future Work

8.1 Conclusions and Summary

In conclusion, it has been shown that certain novel and important features of plasma microturbulence require an understanding of not just the instabilities that drive the turbulence, but also subdominant stable modes that are driven to finite amplitude in the nonlinear state. This has been shown for gyrokinetic simulations of ITG turbulence.

The most general motivation for this research has been to contribute to the broad effort of increasing understanding of plasma microturbulence in fusion devices, with he ultimate aim being to develop the capability to predict its behavior and identify novel methods to suppress its deleterious effects on plasma confinement. More specifically, the goal has been twofold:

1) To build upon the recent identification in fluid models of the critical role of damped eigenmodes in saturating microturbulence and modifying transport levels. This is done by examining the effects of damped modes in comprehensive gyrokinetic models.

2) To characterize the complex, high-dimensional dynamics inherent to kinetically

described turbulence. This is accomplished through mode decompositions of nonlinear gyrokinetic data.

This section provides a brief summary of the major results.

Chapter II describes gyrokinetic energy diagnostics that have been implemented in the GENE code. In Chap. III, the concept of a mode decomposition is introduced. The relation of a gyrokinetic mode decomposition to the analogous decomposition in a fluid model is discussed. A method for constructing a linear eigenmode decomposition of gyrokinetic data is defined wherein left eigenvectors are used to project out the contribution of the eigenmodes to the nonlinear dynamics. Methods for overcoming the issue of non-orthogonality are discussed, including the process of orthogonalizing the eigenvectors with the Gram-Schmidt method. A decomposition onto the basis of orthogonalized eigenvectors reveals that damped modes are excited in such a way that their amplitudes decrease with both increasing damping rate and deviation of the mode frequency from that of the unstable mode. The use of POD to construct mode decompositions is then described along with a discussion of the very powerful properties of a POD - optimality and orthogonality of both right and left eigenvectors. A detailed presentation of results from a POD of nonlinear gyrokinetic data is presented. The first POD mode is very similar to the driving instability and a hierarchy of subdominant modes is excited. These modes are characterized by a variety of structure in phase space. This structure achieves finer scales as mode number increases. The time histories of the modes are defined by increasingly fast time scales as the mode number increases.

In Chap. IV POD mode decompositions are applied to the question of saturation mechanisms for ITG turbulence. It is found that energy dissipation peaks at large perpendicular scales - the same scales where the instability operates. This is a striking contrast with hydrodynamic turbulence (where energy drive and dissipation occur at

distinct scales), and most theories for saturation of plasma microturbulence which have, at least implicitly, assumed dissipation at small perpendicular scales. A novel form of equipartition is found to organize the level of damped eigenmode excitation at high mode numbers.

In Chap. V, the role of subdominant modes in electromagnetic turbulence is examined. It is found that several subdominant linear eigenmodes with tearing parity are part of the linear spectrum. In the nonlinear turbulence, modes with tearing parity are excited to significant levels. It is found that single modes with tearing parity ($n = 1$ or 2 in the POD decomposition) produce a significant amount of magnetic diffusivity. In addition the residual modes ($n > 2$) produce, in aggregate, a greater degree of magnetic diffusivity. The mode structures that correspond most closely to the unstable modes are associated with a relatively low contribution to the magnetic stochasticity although a low level of diffusivity is produced due to the deviation from exact non-tearing parity at finite values of k_x.

In Chap. VI, HOSVD, a high-dimensional variant of the matrix decomposition SVD (which underlies the POD methods) is discussed. Various mathematical properties of the HOSVD are described and compared with the SVD. A description of the numerical optimization and implementation of a scalable HOSVD algorithm is described. Then HOSVD is applied to the full 6-D (five dimensions plus time) distribution function from a nonlinear simulation. This offers a unique global characterization of the data set which reveals many of the important aspects of the underlying turbulence. One very practical application of the HOSVD is in compressing the large amounts of data produced by gyrokinetic simulations. It is found that the HOSVD does this very effectively in comparison with the SVD.

In Chap. VII, preliminary results inferring damped mode excitation from gyrokinetic data without the use of mode decompositions is reviewed. Many of the results

have been replaced by the results in Chaps. II through V, but others remain instructive. It was shown that a type of quasilinear estimate overstates the true flux. This is a valid method for inferring damped mode activity and is discussed in light of the results in Sec. 4.2. Calculations of cross-phase pdfs are also presented and interpreted in light of subdominant mode excitation.

8.2 Future Work

Many avenues of future work have been identified during the course of this research. A few examples are discussed here:

1). The results presented here have been largely limited to examination of ITG turbulence and could be applied to other important types of turbulence (e.g., CTEM and ETG). For example, it is of interest to discover whether there is a parameter regime in which the gyrokinetic description matches more closely the results from fluid models with regard to the significant reduction of transport from quasilinear expectations seen in the latter (i.e., a strong inward flux due to damped modes).

2). The equipartition of amplitude attenuation rate outlined in Sec. 4.4 hints at underlying principles that determine the excitation of damped modes and resulting saturation of the turbulence. This is currently being explored both analytically and numerically with the expectation of attaining valuable new insights into the organization of kinetically described plasma microturbulence.

3). Mechanisms for damped mode excitation have not been thoroughly examined in the context of gyrokinetics. For example, it has yet to be established whether the fine scale phase space $(z, v_{||}, \mu)$ structure which develops at large scales is due to Landau damping and linear phase mixing, or alternatively if there is an underlying nonlinear mechanism. It is likely the latter, although this has not been rigorously

explored.

4). A question (which is likely related to the previous point) is regarding the role and relative importance of zonal flows with relation to damped mode excitation. It is clear that zonal flows are important in moderating the turbulence; is this effect separate from damped mode activity or is it intimately connected? It is expected that some common assumptions of the effects of zonal flows may be reinterpreted in the context of damped mode excitation.

5). Mode decompositions like POD have been used in the hydrodynamics community to construct reduced models of turbulent systems (59). Many of the techniques and insights developed in the course of this research may facilitate construction of such models for the description of plasma microturbulence. For example, the ability to apply HOSVD and SVD to very large data-sets could allow for the extraction of a (relatively) small number of modes which describe the transport.

APPENDICES

APPENDIX A

Gyrokinetic Equation and Definitions of Expressions

The notation in this appendix follows very closely that of Ref. (38). The quantities below are normalized as follows:

$$
\begin{array}{ccc}
k_x \rightarrow \frac{k_x}{\rho_{ref}} & k_x \rightarrow \frac{k_x}{\rho_{ref}} & v_{||} \rightarrow c_{ref} v_{Tj} v_{||} \\
\mu \rightarrow \frac{T_{ref}}{B_{ref}} T_{0j} \mu & B_0 \rightarrow B_{ref} B_0 & t \rightarrow \frac{L_{ref}}{c_{ref}} t \\
m_j \rightarrow m_{ref} m_j & T_{0j} \rightarrow T_{ref} T_{0j} & n_{0j} \rightarrow n_{ref} n_{0j} \\
q_j \rightarrow e q_j & c_{ref} = \sqrt{T_{ref}/m_{ref}} & \rho_{ref} = c_{ref}/\Omega_{ref} \\
\Omega_j = \frac{q_j B_0}{m_j} & \Omega_j \rightarrow \Omega_{ref} \Omega_j & \Omega_{ref} = \frac{e B_{ref}}{m_{ref} c} \\
v_{Tj} = \sqrt{2 T_{0j}} m_j, & &
\end{array}
\tag{A.1}
$$

where the subscript ref denotes a reference quantity, e.g., ρ_{ref} is a reference micro-scale length (usually the ion gyro-radius), L_{ref} is a macro-scale length (like the major radius R), and c_{ref} is a reference velocity (like the thermal velocity).

The gyrokinetic equation can be expressed

$$\frac{\partial g_j}{\partial t} = \mathcal{L}[g_j] + \mathcal{N}[g_j], \tag{A.2}$$

where g_j is related to the full perturbed distribution f_j function through

$$f_j = g_j - \frac{2q_j}{m_j v_{Tj}} v_{||} \bar{A}_{||} F_{0j}, \tag{A.3}$$

and j denotes particle species.

The linear operator is

$$\begin{aligned}\mathcal{L}[g_j] = &-v_* F_{0j} i k_y \chi_j + \frac{\beta T_{0j}}{L_p q_j B_0^2} v_{||}^2 i k_y \Gamma_j - v_{Tj} v_{||} \Gamma_{jz} \\ &-v_d (K_y i k_y + K_x i k_x) \Gamma_j + \frac{v_{Tj} \mu}{2} \frac{\partial B_0}{\partial z} \frac{\partial f_j}{\partial v_{||}} + C_j(f_j).\end{aligned} \tag{A.4}$$

The parallel advection term contains the expression,

$$\begin{aligned}\Gamma_{jz} &= \frac{\partial g_j}{\partial z} + \frac{q F_{0j}}{T_{0j}} \frac{\partial \chi_j}{\partial z} + v_{Tj} v_{||} \frac{q F_{0j}}{T_{0j}} \mu \partial_z B_0 \bar{A}_{||} \\ &= \frac{\partial \Gamma_j}{\partial z} - \mu \partial_z B_0 \frac{q F_{0j}}{T_{0j}} \bar{\phi},\end{aligned} \tag{A.5}$$

and the remaining terms in Eq. A.4 are defined as follows:

$$
\begin{aligned}
F_{0j} = F_0 &= \pi^{-3/2} e^{-(v_{||}^2 + \mu B_0)} \\
\chi_j &= \bar{\phi}_j - v_{Tj} v_{||} \bar{A}_{||_j} \\
\Gamma_j &= g_j + \frac{q_j F_{0j}}{T_{0j}} \chi_j \\
v_* &= \frac{1}{L_n} + \frac{1}{L_{Tj}} (v_{||}^2 + \mu B_0 - \frac{3}{2}) \\
v_d &= \frac{T_{0j}}{q_j B_0} (2 v_{||}^2 + \mu B_0) \\
K_x &= -\sin(z) \\
K_y &= -\cos(z) - \hat{s} z \sin(z) \\
B_0(z) &= \frac{1}{1 + \epsilon_t \cos(z)}
\end{aligned}
\tag{A.6}
$$

The expressions for the equilibrium magnetic field, B_0 (for which ϵ_t is the inverse aspect ratio), and the curvature terms, K_x and K_y, are the expressions for $\hat{s} - \alpha$ equilibrium (47) with $\alpha = 0$. L_p, L_{Tj}, and L_n are the equilibrium scale lengths for the pressure, temperature, and density respectively (normalized to L_{ref}), v_{Tj} is the thermal velocity for particle species j, and $C_j(f_j)$ is a collision operator.

The overbar denotes a gyroaverage which (in a Fourier representation) is accomplished by multiplying by a zeroth-order Bessel function, J_0. For example the gyroaverage of the electrostatic potential is,

$$
\begin{aligned}
\bar{\phi} &= J_0(\lambda_j) \phi \\
\lambda_j &= \left(\frac{2 B_0 \mu}{m_j} \right)^{1/2} \frac{k_\perp}{\Omega_j} \\
k_\perp^2 &= (k_x + \hat{s} z k_y)^2 + k_y^2 .
\end{aligned}
\tag{A.7}
$$

Expressions for the electromagnetic fields are necessary in order to close the system. The gyrokinetic Poisson equation is

$$\phi = \frac{\sum_j n_{0j}\pi q_j B_0 \int J_0(\lambda_j) g_j dv_{||} d\mu}{k_\perp^2 \lambda_D^2 + \sum_j \frac{q_j^2}{T_{0j}} n_{0j}(1-\Gamma_0(b_j))}, \tag{A.8}$$

where $\lambda_D = \sqrt{\frac{B_{ref}^2}{4\pi c^2 n_{ref} m_{ref}}}$ is the Debye length, $\Gamma_0(x) = e^{-x}\hat{I}_0(x)$ ($\hat{I}_0$ is the zeroth order modified Bessel function) and $b_j = \frac{v_{Tj}^2 k_\perp^2}{2\Omega_j^2}$.

The perturbed magnetic field is obtained from the parallel magnetic vector potential $A_{||}$ via the gyrokinetic Ampere's law,

$$A_{||} = \frac{\sum_j \frac{\beta}{2} q_j n_{j0} v_{Tj} \pi B_0 \int v_{||} J_0(\lambda_j) g_j dv_{||} d\mu}{k_\perp^2 + \sum_j \frac{\beta q_j^2}{m_j} n_{0j} \pi B_0 \int v_{||}^2 J_0^2(\lambda_j) F_{0j} dv_{||} d\mu}, \tag{A.9}$$

where $\beta = \frac{8\pi n_{ref} T_{ref}}{B_{ref}^2}$.

The nonlinear operator is

$$\mathcal{N}[g_j] = \sum_{\vec{k'}_\perp} (k'_x k_y - k_x k'_y) \chi_j(\vec{k'}_\perp) g_j(\vec{k}_\perp - \vec{k'}_\perp). \tag{A.10}$$

APPENDIX B

Flux Tube Parallel Boundary Condition

The domain in the parallel direction is labelled by the poloidal angle, z, and restricted to one poloidal turn ($z = [-\pi, \pi]$). In order to extend the domain along the field line, multiple poloidal turns must be connected with a boundary condition in the parallel direction. This is complicated when the magnetic field has finite magnetic shear, $\hat{s} = \frac{x_0}{q_0}\frac{\partial q}{\partial x}|_{x_0}$. By convention, the domain is chosen to be a box at $z = 0$. The magnetic shear causes it to distort into a parallelogram as it progresses along the field line. This distortion occurs with opposite orientation in the $+z$ and $-z$ directions so that a shift is necessary in order to match domains at the $\pm\pi$ boundary. This shift is equal to the integral of the magnetic shear along the field line (simply $2\pi\hat{s}$ for $(s - \alpha)$ (47) geometry) multiplied by the radial distance $(x - x_0)$, so that the boundary condition in direct space is,

$$F(x, y, z = \pi) = F(x, y + 2\pi\hat{s}(x - x_0), z = -\pi), \tag{B.1}$$

where x_0 is the center of the box.

For a Fourier representation this boundary condition implies

$$\sum_{k_x}\sum_{k_y} f_{k_x,k_y}(z=\pi)e^{-ik_x x}e^{-ik_y y} = \sum_{k_x}\sum_{k_y} f_{k_x,k_y}(z=-\pi)e^{-ik_x x}e^{-ik_y(y+2\pi\hat{s}(x-x_0))}$$
$$= \sum_{k'_x}\sum_{k_y} f_{k'_x,k_y}(z=-\pi)e^{i2\pi\hat{s}x_0k_y}e^{-ik'_x x}e^{-ik_y y}, \tag{B.2}$$

where the sum has been shifted from a k_x sum to a sum over $k'_x = k_x + 2\pi\hat{s}k_y$. Thus the boundary condition in Fourier space is $f_{k_x,k_y}(z=\pi) = f_{k_x+2\pi\hat{s}k_y,k_y}(z=-\pi)e^{i2\pi\hat{s}x_0k_y}$. This is simplified by noting that the new summation variable k'_x must also be a multiple of $k_{x_{min}} = \frac{2\pi}{L_x}$, where L_x is the radial box length. This enforces the condition

$$mk_{x_{min}} + 2\pi\hat{s}nk_{y_{min}} = Mk_{x_{min}}$$
$$\Rightarrow 2\pi\hat{s}\frac{k_{y_{min}}}{k_{x_{min}}} = N, \tag{B.3}$$

where $k_x = mk_{x_{min}}$, $k_y = nk_{y_{min}}$ and N and M are integers. This is a condition on the box sizes (L_x, L_y) and the magnetic shear, $\hat{s}$, that must be met while defining parameters. Condition B.3 also reduces the phase factor to the simple expression

$$e^{i2\pi\hat{s}x_0k_y} = e^{inN\pi} = (-1)^{nN}. \tag{B.4}$$

The final boundary condition is

$$f_{k_x,k_y}(z=\pi) = f_{k_x+2\pi\hat{s}k_y,k_y}(z=-\pi)(-1)^{nN}. \tag{B.5}$$

This boundary condition, in practice, extends the domain along the field line by connecting additional $z=[-\pi,\pi]$ domains at higher k_x in a k_y dependent fashion.

APPENDIX C

Derivation of Gyrokinetic Energy Equation

The gyrokinetic energy evolution equation, including electromagnetic terms and an arbitrary number of particle species, will be derived in this appendix. An energy operator is defined,

$$W[F,G] \equiv \left\langle \frac{\pi B_0 n_0 T_{0j}}{F_{0j}} \Gamma_j [F]^* G \right\rangle, \tag{C.1}$$

where

$$\left\langle \cdot \right\rangle \equiv \sum_{k_x,k_y} \sum_j \int dz dv_{||} d\mu J(z)(\cdot), \tag{C.2}$$

F and G are functions of the form of the perturbed distribution function g_j, $J(z)$ is a Jacobian (equal to $1/B_0$ for $\hat{s}-\alpha$) and $\Gamma_j = g_j + \frac{q_j F_{0j}}{T_{0j}} \left(\bar{\phi_j} - v_{Tj} v_{||} \bar{A_{||}}_j \right)$ as defined in Eq. A.6.

Apply this operator to the gyrokinetic equation as follows,

$$W \left[g_j, \frac{\partial g_j}{\partial t} = \mathcal{L}[g_j] + \mathcal{N}[g_j] \right] + c.c., \tag{C.3}$$

and consider the results term by term.

The operation on the time derivative contains terms proportional to

$$\langle \phi^* \pi n_{0j} q_j B_0 J_0(\lambda_j) g_j \rangle \,, \tag{C.4}$$

$$\left\langle A_{||}^* \pi n_{0j} q_j B_0 v_{Tj} v_{||} J_0(\lambda_j) g_j \right\rangle , \tag{C.5}$$

and,

$$\left\langle g_j^* g_j \right\rangle , \tag{C.6}$$

where the time derivatives now operate on the entire quantity (using the product rule). Note that the coefficients that multiply g_j in expression C.4 are the same factors in the species summation and velocity space integral in the gyrokinetic Poisson equation (Eq. A.8), and the coefficients that multiply g_j in expression C.5 correspond to those in the gyrokinetic Ampere's law (Eq. A.9). Thus, these two terms (C.4 and C.5) become quadratic in the fields ϕ and $A_{||}$ so that the total quantity associated with these terms is

$$D(k_\perp)|\phi|^2 + \left[\frac{2k_\perp^2}{\beta} - \pi B_0 \sum_j \frac{n_{0j} q_j^2 v_{Tj}^2}{T_{0j}} \int dv_{||} d\mu v_{||}^2 J_0(\lambda_j)^2 F_{0j} \right] |A_{||}|^2, \tag{C.7}$$

where $D(k_\perp) = k_\perp^2 \lambda_D^2 + \sum_j \frac{q_j^2 n_{0j}}{T_{0j}} (1 - \Gamma_0(b_j))$.

Expression C.6 can be expressed in terms of the full distribution function, f_j and

the magnetic vector potential via the relation $g_j = f_j + \frac{2q_j v_{||}}{m v_{Tj}} \bar{A}_{||_j} F_{0j}$ so that

$$|g_j|^2 = |f_j|^2 + \left(\frac{2q_j F_{0j} v_{||}}{m v_{Tj}}\right)^2 |J_0(\lambda_j) A_{||}|^2 + \frac{2q_j F_{0j} v_{||}}{m v_{Tj}} \left(f_j^* J_0(\lambda_j) A_{||} + (J_0(\lambda_j) A_{||})^* f_j\right). \tag{C.8}$$

The gyrokinetic Ampere's law can be expressed in terms of f_j (rather than g_j as in Eq A.9) as

$$A_{||} = \frac{\beta}{2k_\perp} \pi B_0 \sum_j n_{0j} q_j v_{Tj} \int v_{||} J_0(\lambda_j) f_j dv_{||} d\mu. \tag{C.9}$$

After applying this version of Ampere's law to the last term on the RHS of Eq. C.8, the resulting expression for Eq. C.8 is

$$\sum_j \int dv_{||} d\mu \pi B_0 n_{0j} T_{0j} \frac{|f_j|^2}{F_{0j}} + \left[\sum_j \pi B_0 \frac{n_{0j} q_j^2 v_{Tj}^2}{T_{0j}} \int dv_{||} d\mu v_{||}^2 J_0(\lambda)^2 F_{0j} + \frac{2k_\perp}{\beta}\right] |A_{||}|^2. \tag{C.10}$$

Now the $\sum_j \pi B_0 \frac{n_{0j} q_j^2 v_{Tj}^2}{T_{0j}} \int dv_{||} d\mu v_{||}^2 J_0(\lambda)^2 F_{0j} |A_{||}|^2$ terms cancel in expressions C.7 and C.10 so that the final energy quantity is

$$E = \sum_{k_x, k_y} \sum_j \pi B_0 n_{0j} T_{0j} \int dz dv_{||} d\mu J(z) \frac{|f_j|^2}{F_{0j}} + \sum_k D(k_\perp) |\phi|^2 + 2 \sum_k \frac{k_\perp^2}{\beta} |A_{||}|^2. \tag{C.11}$$

Now consider the terms in Eq C.3 associated with the linear operator. The linear

operator is reproduced here for easy reference:

$$\mathcal{L}[g_j] = -v_* F_{0j} i k_y \chi_j + \frac{\beta T_{0j}}{L_p q_j B_0^2} v_{||}^2 i k_y \Gamma_j - v_{Tj} v_{||} \Gamma_{jz}$$
$$-v_d (K_y i k_y + K_x i k_x) \Gamma_j + \frac{v_{Tj} \mu}{2} \frac{\partial B_0}{\partial z} \frac{\partial f_j}{\partial v_{||}} + C_j(f_j). \tag{C.12}$$

The electromagnetic and curvature terms vanish under a summation over k_x, k_y:

$$\frac{\beta T_{0j}}{L_p q_j B_0^2} v_{||}^2 \left(\sum_{k_x, k_y} i k_y \Gamma_j^* \Gamma_j \right) = 0 \tag{C.13}$$

$$v_d K_y \left(\sum_{k_x, k_y} i k_y \Gamma_j^* \Gamma_j \right) = 0 \tag{C.14}$$

$$v_d K_x \left(\sum_{k_x, k_y} i k_x \Gamma_j^* \Gamma_j \right) = 0 \tag{C.15}$$

These terms vanish because $\Gamma_j^* \Gamma_j$ is even in k_x and k_y (due to the reality constraint for Fourier transforms, $\hat{f}_k^* = \hat{f}_{-k}$), and it is multiplied by an odd factor (k_x or k_y).

Now consider the parallel derivative terms. While calculating these terms an alternative form for Γ_j will be used,

$$\Gamma_j = f_j + \frac{q_j F_{0j}}{T_{0j}} \bar{\phi}. \tag{C.16}$$

Using this notation, the $v_{||}$ derivative becomes,

$$\frac{v_{Tj} \mu}{2} \partial_z B_0 \frac{\partial f_j}{\partial v_{||}} = \frac{v_{Tj} \mu}{2} \partial_z B_0 \frac{\partial \Gamma_j}{\partial v_{||}} + v_{Tj} v_{||} \mu \partial_z B_0 \frac{q F_{0j}}{T_{0j}} \bar{\phi}. \tag{C.17}$$

Also, the parallel advection term can be rewritten (as in Eq. A.5),

$$-v_{Tj}v_{||}\Gamma_{jz} = -v_{Tj}v_{||}\frac{\partial \Gamma_j}{\partial z} - v_{Tj}v_{||}\mu\partial_z B_0 \frac{qF_{0j}}{T_{0j}}\bar{\phi}, \tag{C.18}$$

so that the sum of the two parallel derivative is,

$$\begin{aligned} -v_{Tj}v_{||}\Gamma_{jz} + \frac{v_{Tj}\mu}{2}\partial_z B_0 \frac{\partial f_j}{\partial v_{||}} = \\ -v_{Tj}v_{||}\frac{\partial \Gamma_j}{\partial z} - v_{Tj}v_{||}\mu\partial_z B_0 \frac{qF_{0j}}{T_{0j}}\bar{\phi} + \frac{v_{Tj}\mu}{2}\partial_z B_0 \frac{\partial \Gamma_j}{\partial v_{||}} + v_{Tj}v_{||}\mu\partial_z B_0 \frac{qF_{0j}}{T_{0j}}\bar{\phi} = \\ -v_{Tj}v_{||}\frac{\partial \Gamma_j}{\partial z} + \frac{v_{Tj}\mu}{2}\partial_z B_0 \frac{\partial \Gamma_j}{\partial v_{||}}. \end{aligned} \tag{C.19}$$

Now the terms in the energy equation involving the parallel derivatives are (note that the B_0 cancels with the Jacobian $J = 1/B_0$ in the z integral in these expressions and is absorbed into the $\langle\cdot\rangle$ operator),

$$\left\langle -\pi n_{0j}T_{0j}v_{Tj}v_{||}\frac{\Gamma_j^*}{F_{0j}}\frac{\partial \Gamma_j}{\partial z} + \pi n_{0j}T_{0j}\frac{v_{Tj}\mu}{2}\partial_z B_0 \frac{\Gamma_j^*}{F_{0j}}\frac{\partial \Gamma_j}{\partial v_{||}} \right\rangle + c.c. \tag{C.20}$$

The z integral of the first term can be integrated by parts as follows,

$$\begin{aligned} -v_{Tj}v_{||}\int dz \frac{\Gamma_j}{F_{0j}}\frac{\partial \Gamma_j}{\partial z} + c.c. = -v_{Tj}v_{||}\int dz \frac{\partial}{\partial z}\frac{|\Gamma_j|^2}{F_{0j}} + v_{Tj}v_{||}\int dz \mu\partial_z B_0 \frac{|\Gamma_j|^2}{F_{0j}} \\ = v_{Tj}v_{||}\int dz \mu\partial_z B_0 \frac{|\Gamma_j|^2}{F_{0j}} \end{aligned} \tag{C.21}$$

where the derivative of the inverse Maxwellian $\partial_z F_{0j}^{-1} = \mu\partial_z B_0 F_{0j}^{-1}$ has been used along with the property $\frac{|f_j|^2}{F_{0j}}|_{z=boundary} = 0$ (note that this zero boundary condition applies after all possible k_x connections have been exhausted).

Likewise, the $v_{||}$ integral of the second term in Eq. C.20 can be integrated by parts

to obtain,

$$\frac{v_{Tj}\mu}{2}\partial_z B_0 \int dv_{||} \frac{\Gamma_j}{F_{0j}} \frac{\partial \Gamma_j}{\partial v_{||}} + c.c. = \frac{v_{Tj}\mu}{2}\partial_z B_0 \int dv_{||} \frac{\partial}{\partial v_{||}} \frac{|\Gamma_j|^2}{F_{0j}} - \frac{v_{Tj}\mu}{2}\partial_z B_0 \int dv_{||} 2v_{||} \frac{|\Gamma_j|^2}{F_{0j}}$$
$$= -\frac{v_{Tj}\mu}{2}\partial_z B_0 \int dv_{||} 2v_{||} \frac{|\Gamma_j|^2}{F_{0j}} \tag{C.22}$$

where the derivative of the inverse Maxwellian $\partial_{v_{||}} F_{0j}^{-1} = 2v_{||}F_{0j}^{-1}$ has been used along with the property $\frac{|f_j|^2}{F_{0j}}|_{v_{||}=boundary} = 0$. Now the remaining term can in Eq. C.21 can be integrated over $v_{||}$ and the remaining term in Eq. C.22 can be integrated over z after which they cancel exactly. This eliminates the contribution of the parallel derivatives to the energy equation.

The drive term enters the energy equation as follows,

$$-\left\langle \pi n_{0j} T_{0j} v_* (g_j + \frac{q_j F_{0j}}{T_{0j}} \chi_j)^* i k_y \chi_j \right\rangle . \tag{C.23}$$

The $k_y \chi_j^* \chi_j$ term vanishes under the k_x, k_y summation leaving the energy drive,

$$-\left\langle \pi n_{0j} T_{0j} v_* g_j^* i k_y \chi_j \right\rangle . \tag{C.24}$$

The final term in the linear operator is the collision term which provides the energy sink,

$$\left\langle \pi n_{0j} T_{0j} v_* \Gamma_j^* C_j(f_j) \right\rangle . \tag{C.25}$$

Now consider the nonlinear operator,

$$\mathcal{N}[g_j] = \sum_{\vec{k'_\perp}} (k'_x k_y - k_x k'_y)\chi_j(\vec{k'_\perp}) g_j(\vec{k_\perp} - \vec{k'_\perp}). \tag{C.26}$$

When multiplied by Γ_j^* we have,

$$\Gamma_j^* \mathcal{N}[g] =$$

$$\sum_{\vec{k'_\perp}} (k'_x k_y - k_x k'_y) g_j(-\vec{k_\perp}) \chi_j(\vec{k'_\perp}) g_j(\vec{k_\perp} - \vec{k'_\perp}) \tag{C.27}$$

$$+ \frac{q_j F_{0j}}{T_{0j}} \sum_{\vec{k'_\perp}} (k'_x k_y - k_x k'_y) \chi_j(-\vec{k_\perp}) \chi_j(\vec{k'_\perp}) g_j(\vec{k_\perp} - \vec{k'_\perp}), \tag{C.28}$$

where the reality constraint, $\hat{f}_k^* = \hat{f}_{-k}$, has been used. To account for Eq. C.27, apply the following coordinate transformation (which leaves the sum unchanged):

$$\begin{aligned} \vec{k} &\rightarrow \vec{k'} - \vec{k} \\ \vec{k'} &\rightarrow \vec{k'} \\ \vec{k} - \vec{k'} &\rightarrow -\vec{k}. \end{aligned} \tag{C.29}$$

This reverses the sign on the coupling coefficient,

$$(k'_x k_y - k_x k'_y) \rightarrow -(k'_x k_y - k_x k'_y) \tag{C.30}$$

while leaving the remaining terms unchanged:

$$g_j(-\vec{k_\perp}) \chi_j(\vec{k'_\perp}) g_j(\vec{k_\perp} - \vec{k'_\perp}) \rightarrow g_j(\vec{k_\perp} - \vec{k'_\perp}) \chi_j(\vec{k'_\perp}) g_j(-\vec{k_\perp}) \tag{C.31}$$

This implies that the expression in Eq. C.27 is equal to the negative of itself - in other

words it is zero. Likewise, in order to address the expression in Eq. C.28, consider the following coordinate transformation (which leaves the sum unchanged):

$$\begin{aligned} \vec{k} &\rightarrow -\vec{k'} \\ \vec{k'} &\rightarrow -\vec{k} \\ \vec{k} - \vec{k'} &\rightarrow \vec{k} - \vec{k'}. \end{aligned} \tag{C.32}$$

This also reverses the sign on the coupling coefficient while leaving the remaining terms unchanged, demonstrating that the expression in Eq. C.28 also vanishes. This proves that the nonlinearity conserves the energy quantity.

In summary the gyrokinetic energy quantity is,

$$\begin{aligned} E = \sum_{k_x,k_y} \sum_j \pi B_0 n_{0j} T_{0j} \int dz dv_{||} d\mu J(z) \frac{|f_j|^2}{F_{0j}} + \\ \sum_k D(k_\perp) |\phi|^2 + 2 \sum_k \frac{k_\perp^2}{\beta} |A_{||}|^2 \end{aligned} \tag{C.33}$$

which evolves according to,

$$\frac{\partial E}{\partial t} = Q + C, \tag{C.34}$$

where Q is the drive term proportional to the heat flux,

$$Q = -\left\langle \pi n_{0j} T_{0j} v_* g_j^* i k_y \chi_j \right\rangle + c.c., \tag{C.35}$$

and C is the collisional energy sink,

$$C = \left\langle \pi n_{0j} T_{0j} v_* \Gamma_j^* C_j(f_j) \right\rangle . + c.c. \tag{C.36}$$

APPENDIX D

Orthogonality of Left and Right Eigenvectors

As discussed in Sec. 3.2, the eigenvectors of the linear gyrokinetic operator are non-orthogonal. As such, projection operators (other than the eigenvectors themselves) are necessary in order to isolate the time histories of each eigenmode in an eigenmode decomposition. Consider the matrix whose columns are the eigenvectors, $\vec{f}_n$,

$$F = \begin{bmatrix} \vec{f}_1 & \vec{f}_2 & \cdots \end{bmatrix}. \tag{D.1}$$

The desired projection operators are the rows of the inverse of F,

$$\begin{bmatrix} \vec{f^{(1)}} \\ \vec{f^{(2)}} \\ \cdots \end{bmatrix} \begin{bmatrix} \vec{f}_1 & \vec{f}_2 & \cdots \end{bmatrix} = F^{-1}F = I, \tag{D.2}$$

or, alternatively the columns of the transpose of the inverse of F,

$$F^{-T} = \begin{bmatrix} \vec{f^{(1)}} & \vec{f^{(2)}} & \cdots \end{bmatrix}. \tag{D.3}$$

Now consider the eigenvalue problem of interest,

$$LF = FD, \tag{D.4}$$

Where L is the matrix representing the linear gyrokinetic operator, and D is the diagonal matrix of eigenvalues. Taking the inverse and transpose of Eq. D.4 produces,

$$L^{-T}F^{-T} = F^{-T}D^{-1}. \tag{D.5}$$

It was shown in Eq. D.3 that the columns of F^{-T} are the projection operators, and in Eq. D.5 that the columns of F^{-T} are the eigenvectors of L^{-T}. In addition, the eigenvectors of the inverse of a matrix are the same as the eigenvectors of the matrix. This implies that the columns of F^{-T} also satisfy the left eigenvalue problem:

$$L^{T}F^{-T} = F^{-T}D, \tag{D.6}$$

i.e., the projection operators are the left eigenvectors of the linear gyrokinetic operator.

Bibliography

[1] J. Li, J. Zhang, and X. Duan, Nucl. Fusion **50**, 014005 (2010).

[2] J. D. Lawson, Proceedings of the Physical Society B **70**, 6 (1957).

[3] K. Ikeda, Nucl. Fusion **50**, 014002 (2010).

[4] D. Meade, Nucl. Fusion **50**, 014004 (2010).

[5] M.N. Rosenbluth, and C.L. Longmire, Ann. Phys. **1**, 120 (1957).

[6] I.B. Bernstein, E.A. Frieman, M.D. Kruskal, and R.M. Kulsrud, Proc. R. Soc. A **244**, 17 (1958).

[7] J. Jaquinot, Nucl. Fusion **50**, 014001 (2010).

[8] F.L. Hinton, and R D. Hazeltine, Rev. Mod. Phys. **48**, 239 (1976).

[9] W. Horton, Rev. Mod. Phys. **71**, 735 (1999).

[10] G.D. Conway, Plasma Phys. Control. Fusion **50**, 124026 (2008).

[11] P.W. Terry, and W. Horton, , Phys. Fluids **26**, 106 (1983).

[12] A. Hasegawa and K. Mima, Phys. Rev. Lett. **39**, 205 (1977).

[13] A. Hasegawa and M. Wakatani, Phys. Rev. Lett. **50**, 682 (1983).

[14] B. Coppi and G. Rewoldt, Phys. Rev. Lett. **33**, 1329 (1974).

[15] H. Biglari, P.H. Diamond, P.W. Terry, Phys. Fluids **31**, 9 (1988).

[16] G. Hammett, M.A. Beer, W. Dorland, S.C. Cowley, S.A. Smith, Plasma Phys. and Control. Fusion **35**, 973 (1993).

[17] M. A. Beer, Ph.D. Thesis, Princeton University, (1995).

[18] A.M. Dimits, A. M., G. Bateman, M. A. Beer, B. I. Cohen, W. Dorland, G. W. Hammett, C. Kim, J. E. Kinsey, M. Kotschenreuther, A. H. Kritz, *et al.*, Phys. Plasmas **7**, 969 (2000).

[19] E.J. Doyle, W.A. Houlberg, Y. Kamada, V. Mukhovatov, T.H. Osborne, A. Polevoi, G. Bateman, J.W. Connor, J.G. Cordey, T. Fujita, X. Garbet, T.S. Hahm, L.D. Horton, A.E. Hubbard, F. Imbeaux, F. Jenko, J.E. Kinsey, Y. Kishimoto, J. Li, T.C. Luce, Y. Martin, M. Ossipenko, V. Parail, A. Peeters, T.L. Rhodes, J.E. Rice, C.M. Roach, V. Rozhansky, F. Ryter, G. Saibene, R. Sartori, A.C.C. Sips, J.A. Snipes, M. Sugihara, E.J. Synakowski, H. Takenaga, T. Takizuka, K. Thomsen, M.R.Wade, H.R.Wilson, Nucl. Fusion **47**, S18-S127 (2007).

[20] D. Told, F. Jenko, P. Xanthopoulos, L. D. Horton, E. Wolfrum, Phys. Plasmas **15**, 102306 (2008).

[21] A. Casati, T. Gerbaud, P. Hennequin, C. Bourdelle, J. Candy, F. Clairet, X. Garbet, V. Grandgirard, Ö.D. Gürcan, S. Heuraux, G. T. Hoang, C. Honore, F. Imbeaux, R. Sabot, Y. Sarazin, L. Vermare, and R. E.Waltz, Phys. Rev. Lett. **102**, 165005 (2009).

[22] C. Holland, A. E. White, G. R. McKee, M. W. Shafer, J. Candy, R. E. Waltz, L. Schmitz, and G. R. Tynan, Phys. Plasmas **16**, 052301 (2009).

[23] L. Lin, M. Porkolab, E. M. Edlund, J. C. Rost, C. L. Fiore, M. Greenwald, Y. Lin, D. R. Mikkelsen, N. Tsujii, and S. J. Wukitch, Phys. Plasmas **16** 012502 (2009).

[24] M. Barnes, I.G. Abel, W. Dorland, T. Görler, G. W. Hammett, and F. Jenko, Phys. Plasmas **17**, 056109 (2010).

[25] A. E. White, W.A. Peebles, T. L. Rhodes, C. H. Holland, G. Wang, L. Schmitz, T. A. Carter, J. C. Hillesheim, E. J. Doyle, L. Zeng, G. R. McKee, G. M. Staebler, R. E. Waltz, J. C. DeBoo, C. C. Petty, and K. H. Burrell, Phys. Plasmas **17**, 056103 (2010).

[26] D.A. Baver, P.W. Terry, and R. Gatto, Phys. Plasmas **9**, 3318 (2002).

[27] K. Makwana, P.W. Terry, J.-H. Kim, and D.R. Hatch, submitted to Phys. Plasmas (2010).

[28] P.W. Terry, D.A. Baver, and S. Gupta, Phys. Plasmas **13**, 022307 (2006).

[29] P.W. Terry, D.A. Baver, and D.R. Hatch, Phys. Plasmas **16**, 122305 (2009).

[30] P.W. Terry, Phys. Rev. Lett. **93**, 235004 (2004).

[31] F. Jenko, W. Dorland, M. Kotschenreuther, and B. N. Rogers , Phys. Plasmas, **7**, 1904 (2000).

[32] F. Merz and F. Jenko, Nuclear Fusion **50**, 054005 (2010).

[33] A. A. Vlasov, Soviet Physics Uspekhi **10**, 721 (1968).

[34] E.A. Frieman, L. Chen, Phys. Fluids **25**, 502 (1982).

[35] W.W. Lee, Phys. Fluids **26**, 556 (1983).

[36] A.J. Brizard, and T.S. Hahm, Rev. Mod. Phys. **79**, 421 (2007).

[37] M.A. Beer, S.C. Cowley, and G.W. Hammett, Phys. Plasmas **2**, 2687 (1995).

[38] F. Merz, Ph.D. Thesis, IPP Garching (Dec. 2008).

[39] F. Jenko, B. Dorland, M. Kotschenreuther, and B. Rogers, Phys. Plasmas **7**, 1904 (2000).

[40] W. Nevins et al., Phys. Plasmas **14**, 084501 (2007).

[41] T. Dannert and F. Jenko, Phys. Plasmas **12**, 072309 (2005).

[42] J. Lang, S. Parker, and Y. Chen, Phys. Plasmas **14**, 082315 (2007).

[43] D. R. Ernst, J. Lang, W. M. Nevins, M. Hoffman, Y. Chen, W. Dorland, and S. Parker, Phys. Plasmas **16**, 055906 (2009).

[44] M.J. Pueschel, M. Kammerer, F. Jenko, Phys. Plasmas **15**, 102310 (2008).

[45] S.E. Parker, Y. Chen, W. Wan, B. I. Cohen, and W. M. Nevins, Phys. Plasmas **11**, 2594 (2004).

[46] T. Görler, and F. Jenko, Phys. Plasmas **15**, 102508 (2008).

[47] J. Connor, R. Hastie, and J. Taylor, Phys. Rev. Lett. **40**, 396 (1978).

[48] S. Cowley, R. Kulsrud, and R. Sudan, Physics of Fluids B **3**, 2767 (1991).

[49] T.-H. Watanabe, H. Sugama, Nucl. Fusion **46** , 24 (2006).

[50] J. Candy and R.E. Waltz, Phys. Plasmas **13**, 032310 (2006).

[51] L. Landau, J. Phys. USSR **10**, 25 (1946).

[52] A. Arakawa, Journal of Comp. Phys. **135**, 103-114 (1997).

[53] J. Candy and R.E. Waltz, J. Comput. Phys., **186**, 545 (2003).

[54] W. Dorland, F. Jenko, M. Kotschenreuther, and B.N. Rogers, Phys. Rev. Lett. **85** , 5579 (2000).

[55] P. Xanthopoulos, F. Merz, T. Görler, and F. Jenko, Physical Review Letters **99**, 035002 (2007).

[56] M. Kammerer, F. Merz, and F. Jenko, Phys. Plasmas **15**, 052102 (2008).

[57] J.-H. Kim, and P.W. Terry, Phys. Plasmas **17**, 112306 (2010).

[58] K.F. Riley, M.P. Hobson, S.J. Bence, Mathematical Methods of Physics and Engineering, (Cambridge University Press, 2002) Ed. 2.

[59] G. Berkooz, P. Holmes, and J.L. Lumley, Annu. Rev. Fluid Mech. **25**, 539-575 (1993).

[60] S. Futatani, S. Benkadda, and D. del-Castillo-Negrete, Spatiotemporal multiscaling dynamics of impurity transport in turbulent plasmas". Phys. of Plasmas **16**, 1 (2009).

[61] D. del-Castillo-Negrete, D.A. Spong, and S.P. Hirshman, Phys. Plasmas **15**, 092308 (2008).

[62] G.H. Golub, C.F. Van Loan, Matrix Computations, (The Johns Hopkins University Press, Baltimore and London, 1989) Ed. 2, p. 71.

[63] A.N. Kolmogorov, Dokl. Akad. Nauk SSSR **30**, 299 (1941).

[64] T. Tatsuno, W. Dorland, A.A. Schekochihin, G.G. Plunk, M. Barnes, S.C. Cowley, and G.G. Howes, Phys. Rev. Lett. **103**, 015003 (2009).

[65] G. G. Plunk, S. C. Cowley, A. A. Schekochihin and T. Tatsuno, Two-dimensional gyrokinetic turbulence. Journal of Fluid Mechanics, Available on CJO 19 Oct 2010 doi:10.1017/S002211201000371X

[66] A A Schekochihin, S C Cowley, W Dorland, G W Hammett, GGHowes, G G Plunk, E Quataert, and T Tatsuno, Plasma Phys. Control. Fusion **50**, 124024 (2008).

[67] P.H. Diamond, S.-I. Itoh, K. Itoh and T.S. Hahm, Plasma Phys. Controlled Fusion **47**, R35 (2005).

[68] D.R. Hatch, P.W. Terry, F. Jenko, F. Merz, and W.M. Nevins, submitted to Phys. Rev. Lett.

[69] D.R. Hatch, P.W. Terry, F. Jenko, F. Merz, M.J. Pueschel, W.M. Nevins, and E. Wang, submitted to Phys. Plasmas.

[70] D. Biskamp, A. Zeiler, Phys. Rev. Lett., **74**, 706 (1995).

[71] B.D. Scott, Phys. Rev. Lett., **65**, 3289 (1990).

[72] P.W. Terry, D.R. Hatch, and J.H. Kim, Statistical Theory for Energy Distribution in Gyrokinetic Turbulence, Bull. Amer. Phys. Soc. **55**, No. 15, 304 (2010).

[73] J. Candy, Phys. Plasmas **12**, 072307 (2005).

[74] M.J. Pueschel, and F. Jenko, Phys. Plasmas **17**, 062307 (2010).

[75] W.M. Nevins, E. Wang, and J. Candy, "Magnetic stochasticity in gyrokinetic simulations of plasma microturbulence", LLNL-JRNL-423692 (Feb. 2010), submitted to PRL.

[76] V. Hernandez, J. Roman, and V. Vidal, ACM Transactions on Mathematical Software **31**, 351 (2005).

[77] L.S. Blackford, J. Choi, A. Cleary, E. D'azevedo, J. Demmel, I. Dhillon, J. Dongarra, S. Hammarling, G. Henry, A. Petitet, K. Stanley, D. Walker, and R.C. Whaley, ScaLAPACK Users' Guide, (Society for Industrial and Applied Mathematics, Phlidelphia, PA, 1997), ISBN= $0 - 89871 - 397 - 8$ (paperback).

[78] M.J. Pueschel, Ph.D. Thesis, IPP Garching (Dec. 2009).

[79] A.B. Rechester and M.N. Rosenbluth, Phys. Rev. Lett. **40**, 38 (1978).

[80] T.-H. Watanabe, and H. Sugama, Phys. Plasmas, **11**, 1476 (2004).

[81] L.R. Tucker, Psychometrika, **31**, 279311 (1966).

[82] T.G. Kolda, B.W. Bader, SIAM Review, **51**, 3, 455-500 (2009).

[83] T.G. Kolda, "Multilinear operators for higher-order decompositions", Sandia Reports, SAND2006-2081, (2006).

[84] L. De Lathauwer, B. De Moor, and J. Vandewalle, SIAM J. Matrix Anal. Appl. **21**, 4, 1253-1278 (2000).

[85] L.S. Lorente , J.M. Vega, A. Velazquez, Aerospace Science and Technology **14** 168-177 (2010).

[86] G.H. Golub, C.F. Van Loan, Matrix Computations, (The Johns Hopkins University Press, Baltimore and London, 1989) Ed. 2.

[87] E. Anderson, Z. Bai, C. Bischof, S. Blackford, J. Demmel, J. Dongarra, J. Du Croz, A. Greenbaum, S. Hammarling, A. McKenney, D. Sorensen, LAPACK User's Guide, (Society for Industrial and Applied Mathematics, Philadelphia, PA, 1999) Ed. 3.

[88] D.R. Hatch, P.W. Terry, W.M. Nevins, W. Dorland, Phys. Plasmas **16**, 022311 (2009).

[89] N. Winsor, J.L. Johnson, and J.M. Dawson, Phys. Fluids **11**, 2448 (1968).

[90] M.N. Rosenbluth and F. Hinton, Phys. Rev. Lett. **80**. 724 (1998).

[91] R.E. Waltz, G.M. Staebler, W. Dorland, G.W. Hammett, M. Kotschenreuther, Physics of Plasmas **4**, 2482 (1997).

[92] N. Mattor, P.W. Terry, Phys. Fluids B **4**, 5 May 1992.

[93] G.S. Lee and P.H. Diamond, Phys. Fluids **29**, 3291 (1986).

[94] J.E. Kinsey, G.M. Staebler, R.E. Waltz, Physics of Plasmas **12**, 052503 (2005).

[95] C. Holland, P.H. Diamond, S. Champeaux, E. Kim, O. Gurcan, M.N. Rosenbluth, G.R. Tynan, N. Crocker, W. Nevins, and J. Candy, Nucl. Fusion **43** , 761 (2003).

[96] A. Fujisawa, A. Shimizu, H. Nakano, S. Ohsima, K. Itoh, H. Iguchi, K. Matsuoka, S. Okamura, S.-I. Itoh, and P.H. Diamond, Plasma Phys. and Control. Fusion **48**, A 365 (2006).

[97] K. Itoh, S.-I. Itoh, P.H. Diamond, T.S. Hahm, A. Fujisawa, G.R. Tynan, M. Yagi and Y. Nagashima, Physics of Plasmas **13**, 055502 (2006).

[98] Z. Lin, T.S. Hahm, W.W. Lee, W.M. Tang, and P.H. Diamond, Phys. Rev. Lett. **83**, 3645 (1999).